MODELLING AND DESIGN GUIDELINES OF INTEGRATED HIGH-TEMPERATURE PHOTOELECTRO-CHEMICAL DEVICES

ÉCOLE POLYTECHNIQUE FÉDÉRALE DE LAUSANNE

Laboratory of Renewable Energy Science and Engineering

Alejandra Aguilar Mayordomo

ÉCOLE POLYTECHNIQUE
FÉDÉRALE DE LAUSANNE

SPRING SEMESTER 2020

SEMESTER PROJECT

Supervisors: Ronald Ramiro Gutierrez Perez, Professor Sophia Haussener.

INDEX

ABSTRACT

In the present study, hydrogen and syngas fuels are delivered from water electrolysis and co-electrolysis of water and carbon dioxide, respectively, though the use of an integrated high-temperature photoelectrochemical device, composed of a high temperature solar cell (HTSC) coupled with a solid oxide electrolyser (SOE). Clean, renewable and available solar energy is used as the power source of this device. A numerical multiphysics model is developed, including a one-dimensional model designed to represent the high temperature photoabsorber assembly, and a two-dimensional model embodying the solid oxide electrolyser. The performance of this integrated device is assessed according to certain parameters, including the molar flow of fuel produced at the outlet of the device and the solar-to-fuel efficiency.

The productivity of the device is analysed for both fuel production simulations under a variety of different scenarios, where parameters affecting the structure's design, the material properties and the operating and boundary conditions are varied. The resulting energetic and production performances under each case scenario are measured and appraised, in order to get a broader insight in the effect of these variables in the performance of the fuel-producing device and provide general device design guidelines.

The acquired results show the difference in importance of some specifications over others in the performance of the device. The parametric study for the hydrogen production reveals the number of photoabsorbers as the parameter which most significantly affects the performance of the device. In order to maximise the performance of the HTSC-SOE integrated device, addressing this parameter, a simulation is carried out which allowed to determine the optimum combination of parameters that the device should possess in order to obtain the maximum solar-to-fuel efficiency possible and deliver the highest amount of hydrogen molar flow rate. On the other hand, the parametric study of the syngas fuel production though the co-electrolysis of H_2O and CO displays that the H_2/CO ratio is the most decisive variable which influences the amount of hydrogen and carbon dioxide generated. The reduction of the source of H_2 formation, by diminishing the inlet molar fraction of water at the cathode chamber, is proved to affect the H_2/CO ratio of the device to a bigger extent than increasing the temperature of the electrolyser components. In either of the two simulations, high efficiencies can be accomplished by reducing the required electric power of the electrolyser, which is achieved by increasing its operating temperature.

Key words: integrated device, photoelectrochemical device, solar fuel, HTSC, solid oxide electrolyte, selective barrier, numerical simulation, parametric study, hydrogen, syngas.

LIST OF SYMBOLS AND ABREVIATIONS

LATIN SYMBOLS	DEFINITION
$a_{\mathrm{V},i}$	Specific area, property of the porous anode and cathode electrodes (i =anode, cathode).
A	Area (equation 1b, 10f) or Richardson constant (equations 3a, 3b).
B	Radiative recombination coefficient.
C	Solar constant.
CBO	Conduction band offset.
C_i	Auger recombination coefficient.
D_i	Diffusion coefficient (i =electrons, holes).
D_{ik}	Multi-component Fick diffusivity.
E	Electric field.
$E_{\mathrm{act},i}$	Activation energy for the exchange current density (i = O_2, H_2, CO).
E_{Fn}	Fermi level of the barrier.
E_{Fp}	Fermi level of the absorber.
E_i	Equilibrium potential for the half reaction at the anode and cathode (i = O_2, H_2).
E_i°	Standard cell potential (i = O_2, H_2, CO).
$E_{\mathrm{g},i}$	Band gap energy (i =barrier, absorber).
E_{C}	Conduction band.
E_{F}	Fermi level.
E_{G0}	Bandgap extrapolated to absolute zero.
E_{V}	Valence band.
F	Faraday’s constant.
G	Generation rate
h	Convection coefficient.
$h_{\mathrm{c,f}}$	Convection coefficient at the cathode.
$H_{\mathrm{S,1}}$	The volumetric heat source and the boundary heat sources in the HTSC (Q_{tot} + Q_{b}).
$H_{\mathrm{S,3}}$	The reflected heat source from the HTSC to the bottom of the glass cover.
$i_{0,i}$	Local current densities at the anode and cathode (i = O_2, H_2, CO).
i_i	Exchange current densities at the anode and cathode (i = O_2, H_2, CO).
i_{l}	Ionic current.
i_{sc}	Short circuit current density.
I	Current.
I_{o}	Dark current.
I_{sc}	Short circuit current.
I_{sun}	Solar irradiation.
J	Total photocurrent.
J_{em}	current density emitted from the absorber to the barrier.
J_i	Carrier current density at the interface between barrier and absorber (i =electrons, holes).
J_{rev}	reversed photocurrent from the metal electrode.
k_{B}	Boltzmann’s constant.
k_{eff}	Effective thermal conductivity of the porous media.
k_i	Pre-exponential coefficient of the anode and cathode electrodes (i = O_2, H_2, CO).
k_{p}	Conductivity of the bulk (anode or cathode).
L	Minority charge carrier diffusion length.
m_i	Effective mass (i = electrons, holes).
M_i	Molar mass of species i.
n	Number of moles of electrons transferred.
$n_{\mathrm{eq},i}$	Concentration of charge carriers at equilibrium (i=electrons, holes).
n_i	Mole flow rate of species i= O_2, H_2, or carrier concentration of i =electrons, holes.
n_{i}	Intrinsic carrier concentration.

N_A	Dopant concentration in p-type material (absorber).
N_D	Dopant concentration in n-type material (barrier).
p	Pressure.
p_A	Absolute pressure.
$p_{i,\mathrm{ref}}$	Reference partial pressure of species i = O_2, H_2, H_2O, CO, CO_2.
p_i	Partial pressure of species i = O_2, H_2, H_2O, CO, CO_2.
P_fuel	Power contained in the fuel produced in the electrolyser.
P_nabs	Part of the solar energy transmitted though the photoabsorber.
P_{sc}	Power generated in the solar cell.
q	Electronic charge constant.
Q	Electric charge.
Q_a	Heat released at the anode electrode.
Q_b	Boundary heat sources at both the barrier and absorber ($Q_{rec,b}$+Q_p+Q_{lost}).
Q_br	Mass source term: addition of mass to the flow due to electrochemical reactions.
Q_c	Heat released/absorbed at the cathode electrode.
$Q_{\mathrm{cond},i}$	Heat loss by conduction at the inlet of the anode/cathode chambers.
$Q_\mathrm{c,g}$	Heat lost by convection from the glass cover into the atmosphere.
Q_e	Heat released at the solid electrolyte due to joule heating.
Q_EC	Heat energy due to the electrochemical reactions.
Q_j	Heat loss due to Joule heating in the photoabsorber.
Q_JH	Joule heating due to the charge transport in the solid conductors.
Q_lost	The difference between the all heat sources and the incoming solar radiation, it is used to close the balance.
Q_P	Heat loss due to the Peltier effect.
$Q_\mathrm{r,g}$	Heat lost by radiation from the glass cover into the atmosphere (Q_{rad}).
Q_rec	Heat loss due to internal recombination mechanisms in the photoabsorber assembly.
$Q_\mathrm{rec,b}$	Heat loss due to surface recombination in the metal contacts.
P_ref	Heat reflected from the glass cover into the atmosphere.
Q_ref	Heat energy reflected at the front of the photoabsorber.
Q_s	Added or removed heat in the system.
$Q_{\mathrm{s},i}$	Sensible heat for heating the reactants and products inside the chambers.
Q_sr	Radiative heat source.
Q_sun	Total solar power incident in the device.
Q_t	Heat loss due to thermalization in the photoabsorber.
Q_tot	Volumetric heat source inside the photoabsober device: barrier and absorber (Q_{th}+Q_J+Q_{rec}-Q_{sr}).
R	Recombination rate (*equations 3c, 5a*) or the ideal gas constant (electrolyser equations).
R_WGSR	Rate of water gas shift reaction.
S_1	Surface recombination velocity at interface between barrier and metal electrode.
S_2	Surface recombination velocity at interface between barrier and absorber.
S_3	Surface recombination velocity at interface between absorber and metal electrode.
T	Temperature.
$T_{i,\mathrm{ch}}$	Temperature of the chamber (i =cathode, anode).
T_in	Temperature at the inlet of the anode and cathode chamber.
T_sc	Local temperature of the solar cell.
VBO	Valence band offset.
V_A	Relative work function of the electrode.
V_C	Relative work function of the absorber.
V_e	Operating voltage of the electrolyser.
V_fb	Flat band potential (V_{fb}=V_C-V_A).
V_oc	Open circuit voltage.
V_sc	Photovoltage of the solar cell.
V_bi	Built-in voltage.
W_s	Added or removed power in the system.

x_i	Mass fraction of species i at the inlet of the cathode/anode chamber (i =H_2O, O_2, N_2, H_2).
x_k	Mole fraction of species k.

GREEK SYMBOLS	DEFINITION
λ	Wavelength.
σ	Stephan Boltzmann constant.
μ_i	Charge carrier mobility (i =electrons, holes).
ρ	Density.
κ	Electrode permeability.
$\emptyset$	Electrostatic potential.
$\emptyset_l$	Ionic potential.
θ_p	Volume fraction of the anode and cathode.
$\phi_{I,i}$	Potential of the electrolyte (i =anode, cathode).
η_i	Activation overpotentials at the anode and cathode (i = O_2, H_2, CO).
η_{ohm}	Ohmic resistance in the electrolyte and electrodes.
η_{STF}	Solar to fuel efficiency.
α_i	Asymmetry factor (i = cathode, anode).
ε	Emissivity.
ε_{p}	Electrode porosity.
ω_k	Mass fraction of species k.
σ_i	Ionic conductivities of the anode and cathode electrodes (i = anode, cathode).
σ_i°	Pre-exponential factor of the anode and cathode (i = anode, cathode).
σ_{elec}	Ionic conductivity of the solid electrolyte.
$\sigma_{\mathrm{elec}}^{\circ}$	Pre-exponential factor (depends on the material of the solid electrolyte).
$\tau_{\mathrm{aug},i}$	Auger recombination lifetime (i =electrons, holes).
τ_i	Minority charge carrier lifetime (i =electrons, holes).
$\tau_{\mathrm{rad},i}$	Radiative recombination lifetime (i =electrons, holes).
$\tau_{\mathrm{srh},i}$	Shockley-Read-Hall recombination lifetime (i =electrons, holes).
ΔE_{C1}	Conduction band offset between absorber and barrier.
ΔE_{V1}	Valence band offset between absorber and barrier.
ΔG_i°	Gibbs free energy at 298K.

LIST OF FIGURES

LIST OF TABLES

1. INTRODUCTION

1.1 BACKGROUND AND PROBLEM DESCRIPTION

Due to the increasing awareness of global warming and climate change, the demand of clean energy and fuels has powered the research in renewable energies. Designing and building sustainable systems are, consequently, some of the most critical issues the present society addresses. Developing sustainable fuels which are able to replace the current energy carrier fuels is a key step in fulfilling this objective. Humanity currently relies on fossil fuels to power the day a day life. This has been proven to be, not only unsustainable, but noxious to the planet. This is due to the fact that the gases released during the burning of fossil fuels include the so-called greenhouse gases. As it may be known to the reader, greenhouse gases are the main contribution to global warming, defined as the progressive increase in the average temperature of the Earth's atmosphere due to an increased amount of heat energy being trapped in the atmosphere, and not radiating out into space. The effect of this phenomena is progressively becoming more and more evident, driving climate change. Human activity has been pointed out as the ultimate cause of this phenomena, as experts attribute the increase in atmospheric warming to the increased amount of carbon-containing gases produced by human activity. As a consequence of the increased use of fossil fuels, the warming trend is being accelerated. Hence the need to cut down emissions by reducing our dependence on fossil fuels.

Clean energy means less exposure to harmful emissions and less consumption of natural resources. Nowadays renewable energy solutions are progressively becoming cheaper [1], [2], more reliable and more efficient, building the path to an affordable, resilient and clean energy future. The advantages brought by renewable and sustainable ways of producing energy are numerous. Not only the planet's wellness is improved, but a country's economy can be also positively affected, as, though homegrown resources, clean energy increases the country's energy independence [3]. Producing clean energy involves using sustainable sources to directly produce electric power (such as wind or tidal power plants) or to alternatively produce clean fuels (hydrogen being one of the most potential ones). In recent times, a number of countries around the world have implemented policies, which favour the use of hydrogen in a diverse number of sectors, in order for the carbon emissions of these sectors to be reduced [4]. Hydrogen gas is versatile and has a wide variety of uses, which can be grouped in two major categories: H_2 gas as a feedstock and H_2 gas as an energy vector. Some of these applications include energy storage, stationary power and mobility. The latter being one of the most fundamental application of this gas, with the ultimate goal of fully decarbonising the transportation system. Not only this, but the versatility of this fuel and its numerous applications are some of the reasons why hydrogen can become an important contributor in the decarbonization of existing economies [5].

The diversity of the potential supply sources used in the extraction of hydrogen form its source constitutes a fundamental reason why this gas is considered such a promising energy carrier. The variety of methods and resources through which it can be obtained is wide, some including fossil fuels such as coal and natural gas, nuclear energy, non-food crops, all of these releasing CO_2 during the process. Now-a-days, most of the world's hydrogen production is produced through a process called Steam Methane Reforming, which is considered a CO_2 intensive process, and thus needs to be efficiently replaced. Alternatively, the energy needed for the extraction process of this fuel can also be supplied by renewable sources, such as wind, geothermal, hydroelectric and solar, used to split water [6].

The production of renewable, clean fuels is also achieved with synthesis gas as a resource. This is a raw material for the production of chemicals via a number of different fuel synthesis processes. These include procedures such as: methanation, which involves the gasification of producer gas to methane; Fischer-Tropsch synthesis, in which the syngas undergoes a chain growth reaction (polymerisation) to heavy-weight liquid hydrocarbons; DME (dimethyl ether) synthesis, where CO and H_2 are reacted to form methanol, which is dehydrated into dimethyl ether and water; and methanol synthesis, which, as the name indicates, represents the production of methanol from CO and H_2. All of these processes use synthetic gas to produce second generation biofuels, which can be used, for example, as diesel or gasoline replacement in mobility. The process we focus on in Fischer-Tropsch synthesis, where H_2 and CO are used as the building blocks, which react to produce -CH_2- building blocks. These concatenate with each other, producing liquid fuels when six or seven carbon atoms are present in the molecule. Upstream water gas shift reaction is used to manage the H_2/CO ratio adjustment. Our motivation is to produce the syngas input for these processes in a renewable way, in order to make the final fuel clean. High-temperature co-electrolysis of carbon dioxide and steam offers the possibility to produce synthetic gas. Carbon monoxide can also be obtained from the produced H_2 and CO_2 via reverse-water shift reaction (*equation 6c*). During this process, not only is electrical energy converted into chemical energy, but a route to reduce CO_2 emissions is also provided [7], [8].

In the first part of this study we model the production of H_2 gas though H_2O splitting electrolysis. Meanwhile, in the second part we propose adding CO_2 at the inlet of the device in order to fuel the co-electrolysis reaction, generating H_2 and CO gases, also known as syngas. Operating such methods at high temperatures brings a list of advantages to their performances. Increased operating temperatures mainly provide a pathway to reduce the operating voltage required at the electrolyser and increase the rate of the product production. Other advantages include avoiding back reactions, improving the reaction kinetics, improving the electrolyser's ionic conductivity and the electrode's catalytic activity and allowing for the use of non-expensive catalysts.

The method though which the electrolyser device is powered is a point of interest. In order to make the fuel produced clean, water electrolysis and co-electrolysis of water and carbon dioxide could be powered using solar energy, which could be used in parallel to heat the reactants and increase the electrolyser's working temperature. Solar energy is an interesting energy source in the designing of approaches to generate clean fuels, chemicals and electricity. In the current study, this source of power is intended to be used to produce electric power by the use of solar cells, which work integrated with the electrolyser. Due to its integrated design, the heat sources present in the device affect both the solar cell and the electrolyser in the same manner, meaning that, if we want the electrolyser to work at high temperatures, due to the anticipated advantages, the solar cell would also be forced to do so. This originates a problem, as conventional solar cells work at an average of 50-60°C [16], ceasing to operate at high temperatures, and so would be unable to provide the needed voltages to drive the electrolysis reactions when operating at those conditions. Photogenerated-charge carrier recombination increases due to the reduction of the band bending at high temperatures, resulting in a decrease of the photovoltage produced. Since the maximum voltage produced by the cell decreases as the temperature is increased, this will lead to a drop in performance of the system and, at some point, to the failure of the solar cell. The problem then arises, as the need to find alternative ways to separate photocarriers at high temperatures must be developed and implemented.

A number of researchers have been working in the field, trying to develop different hybrid systems combining photovoltaic solar cells and electrolysers, in order to achieve PV-driven high temperature electrolysis. Litch et al. [9], [10] conducted a theoretical analysis of a model consisting of a photovoltaic component and an electrolyser component, where these two systems in the device where physically separated. In their research, the solar cells did not receive excessive heating, as a light splitter was used to separate the incident solar spectrum, having part of the solar spectrum used to drive the solar cell, and the remaining used for heating the electrolyser components. This meant that the solar cells did not operate at high temperatures, so the device did not require the use of different semiconducting junctions for charge carrier separation. The study carried out by Schwede et al. [11] in 2010 proposed the first PETE (photon-enhanced thermionic emission) converter, a high temperature solar energy collecting method. The developed device consisted of a hot semiconductor cathode and a cold anode, separated by a vacuum gap. High efficiencies were expected; however, the fabrication of such device posed a number of challenges due to the vacuum structure and at the same time, the efficiency and lifetime of the cathode degraded at elevated temperatures. In 2013, the authors Yang and Ye and Yang et al. [12] used the same principle. A modified version of the PETE method presented by Schwede et al. [11] was studied, where they proposed an isothermal, planar high temperature solar cell model, where instead of using a traditional p-n junction for carrier separation, selective contacts were used. The function of these was to selectively separate and extract electrons or holes. The model structure of the HTSC consisted of a narrow band gap absorber with a wide band gap barrier layer and a metal electrode at each side, and the balance between the carrier generation and recombination was used to analyse the performance.

1.2 RESEARCH OBJECTIVE

An integrated, high efficiency device is aimed to be developed, for which a solar cell which is capable of working at high temperatures is required. The desired photoelectrochemical (PEC) device requires the use of semiconducting junction for charge carrier separation at high temperatures. A solid electrolyte for ion conduction is also needed, due to the incapability of electrolytes to be kept in a liquid state at 1atm pressure and temperatures above 100°C. Moreover, the electrolyser's electrodes must be both electron and oxide ion conducting

In the present study we model hydrogen and syngas generation using an integrated photoelectro-chemical device. This involves the use of a photovoltaic device and an electrolyser, which, in our case, is a solid oxide electrolyser. The feasibility of such device is studied through the development of a non-isothermal computational model. The working principle of the designed device is the following: high energy photons are absorbed by the solar cell, generating charge carriers by the photoelectric effect. These are then separated using a selective barrier. The same principle proposed by Yang et al. and Yang and Ye [3], [4] is applied in our model. The photocurrent and photovoltage generated in the HTSC device then power a solid oxide electrolyser, where the electrolysis of water into oxygen and hydrogen, or the co-electrolysis of H_2O and CO_2 into H_2 and CO takes place. The developed model is used to assess the potential of this type of HTSC-SOE device, and provide general design guidelines though a parameter study.

The current study goes one step further in the research made by Ronald Gutierrez [13] (PhD student at EPFL). The main difference between the previous and the present study is that the original model did not involve a completely integrated device, as there was not a direct contact between the HTSC and the components of the electrolyser (*figure 1a*). The HTSC was located in close proximity to the electrolyser components (below few millimetres). In the current device we propose a fully integrated device, where the HTSC is in direct contact with the solid electrolyser, concretely located next to the SOE (*figure 1b*). Another valuable difference to be pointed out is the fact that a quartz glass cover and support are added in the current model, adding extra losses which need to be taken into account. As well as convective and radiative losses to the atmosphere, heat loss due to reflection at the glass surface is also considered. The photoabsorber assembly is a thin film (1 µm the absorber layer and 0.1 µm the barrier layer, 1.1µm in total), which needs to be supported by a material layer (4cm long and 210µm thick quartz base) in order for the desired design to be accomplished. Meanwhile, solar irradiation needs to reach the HTSC in order for it to work, so a transparent material is needed to allow the illumination of the photoabsorber. This material is required to, additionally, act as a wall keeping the cathode fluids in the chamber. A thin (4cm long and 1mm thick), transparent quartz cover is used for this purpose. The parameters varied in the design of the original model when carrying out the parametric analysis were the following: the anode chamber height, the number of photoabsorbers, the cathode thickness, the flow velocity, the flow direction, the type of photoabsorber, solid electrolyte and cathode electrode. Different solar concentrations were also applied during the original study. It was concluded the parameters which had the biggest impact in the energetic and production performance of the device were the properties of the photoabsorber, the ion conductivity of the solid electrolyte, the catalytic activity of the porous cathode and the number of photoabsorber assemblies. During the hydrogen production simulation, the results obtained showed a maximum STF efficiency of 9.78% at 50 suns working with three photoabsorbers operating in series, instead of four, and could produce a maximum of 46 mmolm^{-2}s^{-1} moles of hydrogen gas at higher solar concentrations, when operating with an ideal photoabsorber, GaAsi2 (in this case scenario the material properties of the photoabsorber were modified in order for the open circuit voltage, V_{oc}, to be improved: increased Hockley-Read-Hall lifetime, reduced radiative recombination coefficient, reduced surface recombination velocity at the back of the HTSC). Moreover, the syngas production simulation proved to reach, at 50 suns, a 10.2% STF efficiency, when operating with three photoabsorber assemblies. The maximum H_2 production flow rate, during the syngas generation simulation, was obtained when operating with an ideal photoabsorber (GaAsi2) at 50 suns, attaining a value of 41.2mmolm^{-2}s^{-1}, and that achieved for CO was 13.87mmolm^{-2}s^{-1}, when the specifications involved an inlet molar fraction of water of 0.1.

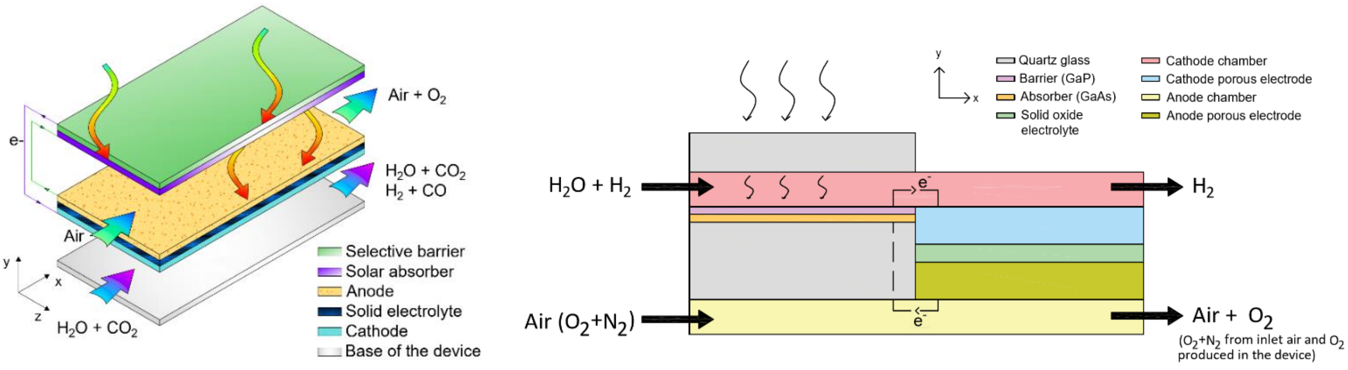

a)

b)

Figure 1a) *Original HTSC-SOE model* [13], ***b)*** *current HTSC-SOE model.*

The motivation which lead us to go one step further in this research was to develop a device which is able to compete with other integrated photoelectrochemical devices. Currently, there are some devices which work at room temperature where the electrodes are photoabsorbers and catalysts at the same time. Our aim is to investigate whether the same can be achieved at high temperatures. In the original study, the operating temperatures of the solar cell and the electrolyser components didn’t differ a lot, so that led to the hypothesis that a more integrated device could be possible to be designed. This was assessed by designing a device where the HTSC and the SOE were placed directly in contact. We then investigated whether this would improve or not the energetic and production performance of the device.

2. THEORETICAL BACKGROUND

2.1 HIGH-TEMPERATURE SOLAR CELLS

In traditional photovoltaic cells, temperature has two main effects. Increasing temperature causes a slight increase in the short circuit current and a more notorious decrease of the open circuit voltage.

Increasing temperature causes the amplitude of atomic vibrations to increase, which in turn leads to larger interatomic spacing. This decreases the potential "seen" by electrons in the material, and so, reduces the band gap energy size [14]. As a consequence, increasing temperature decreases the band gap energy. A link exists between this effect and the slight increase in the current density. The decrease in the band gap energy leads to a bigger fraction of the incoming solar radiation's photons having enough energy to promote electrons from the valence band into the conduction band, thus generating electron-hole pairs which contribute to the current. The open circuit voltage, V_{oc} (equation *1a*) is dependent on the dark current, I_o (equation $1b$), which, in turn, is temperature dependant, as most of the variables used to compute it. The parameter which has the biggest impact in the dark current is the intrinsic carrier concentration, n_i. On its side the intrinsic carrier concentration (equation *1c*) depends on the bandgap (with lower bandgaps giving higher intrinsic carrier concentrations), and on the carrier's energy (with higher temperatures giving higher intrinsic carrier concentrations). In conclusion, the dark current increases with the temperature (meaning more intrinsic carriers, which will increase recombination). This is the dominant effect, which is why in general terms, the solar cell's performance decreases with increasing temperature.

$$V_{\mathrm{oc}} = \frac{kT}{q}\ln\left(\frac{I_{\mathrm{sc}}}{I_0}\right) \qquad (1a)$$

$$I_{\mathrm{o}} = qA\frac{Dn_i^2}{LN_{\mathrm{D}}} \qquad (1b)$$

$$n_i^2 = 4\left(\frac{2\pi kT}{h^2}\right)^3 (m_{\mathrm{e}}m_{\mathrm{h}})^{\frac{3}{2}} exp\left(-\frac{E_{\mathrm{G0}}}{kT}\right) \qquad (1c)$$

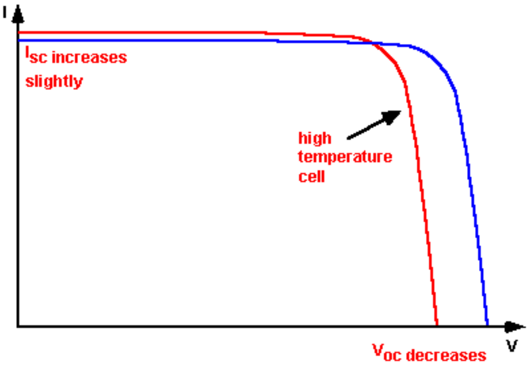

***Figure 2**- Effect of temperature on the IV characteristics of solar cell [15].*

In traditional PV cells, the charge carriers generated by the photovoltaic effect are separated by the built-in electric field of the p-n junction. The built-in voltage depends inversely on the square of the intrinsic carrier density, which increases with operating temperature. This consequently means that, at high temperature, the built-in electric field decreases. PV solar cells are unable to work without the driving force for carrier separation. The rated power of these traditional photovoltaic cell panels is given por STF (at 25°C), however, the operating temperatures vary, and may reach values of 50°C-60°C [16]. As the temperature starts to be increased, diffusion of charge carriers starts to destroy the p-n junction, and recombination will have a negative impact on the performance. Alternatives then have to be searched and implemented, in order to separate the photogenerated charge carriers when aiming to work at high temperatures.

At low temperatures, band bending appears between the semiconductors. The band bending on either side of the junction is governed by the Poisson equation [17]. This bending facilitates the movement of holes and electrons in order for them to be collected, and keeps these photogenerated carriers separated, avoiding recombination (*figure 3a*). As temperature increases, band bending decreases, having the bands slowly become aligned (*figure 3b*). In this situation, electrons do not longer have the driving force to push them towards the metal contact that was previously provided by the band bending, they consequently fall back to their original position. This means photogenerated carriers are no longer kept separated and the photocarriers are free to recombine. Recombination increases, reducing the available photocarriers, reducing, as a consequence, the photovoltage and current density produced.

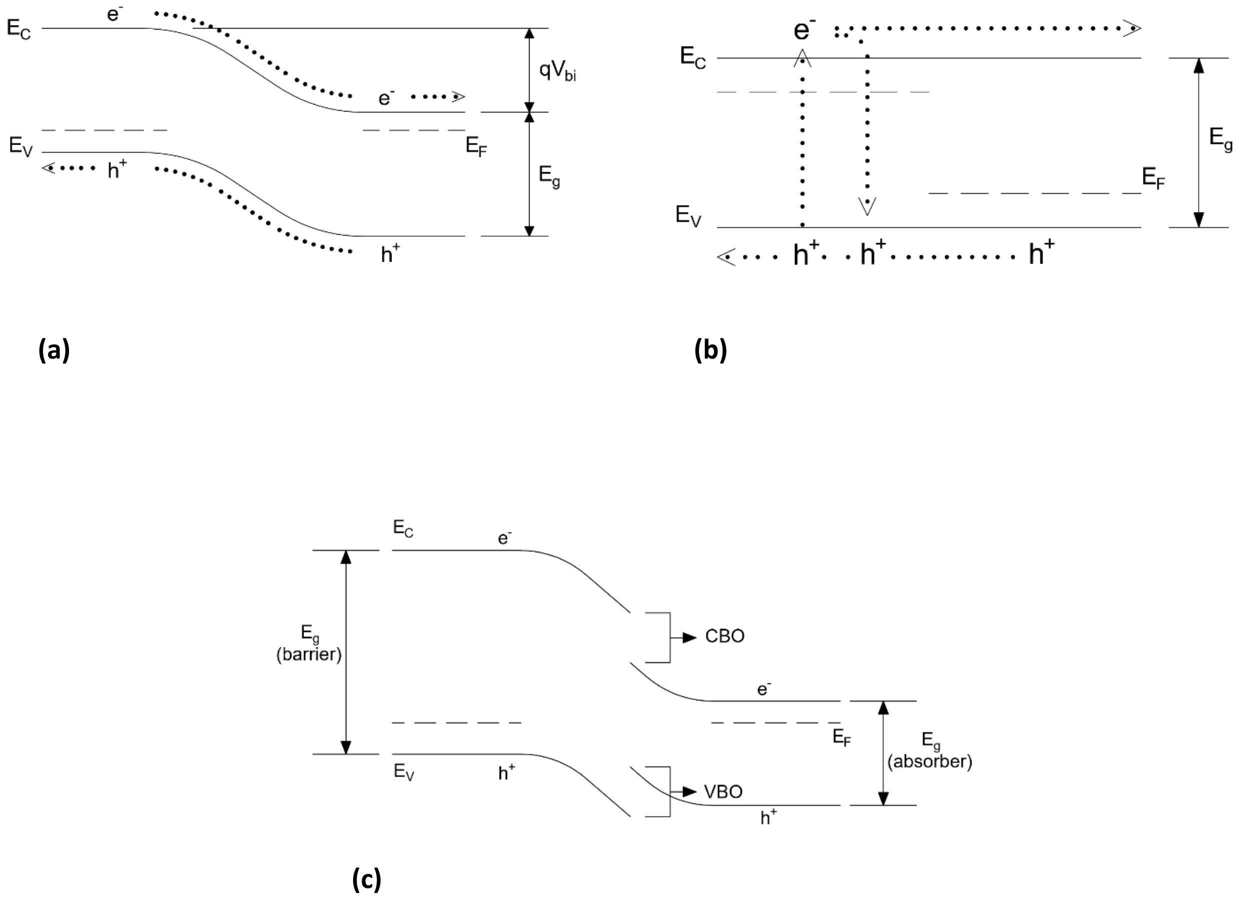

***Figure 3**- Band diagram for the junction of 2 semiconductors **a)** of the same material at low temperatures, **b)** of 2 semiconductors of the same material at high temperatures, **c)** of different materials at low temperatures (heterojunction).*

In this study we aim to work with two different semiconductors at high temperatures, with the purpose of positively affecting the electrolyser's performance. In order to manage this, we make use of a high temperature photovoltaic cells, which involves a photon-enhanced thermionic emission junction (PETE). As already commented, we use the same principle as Yang et al. and Yang and Ye [12], [18], which is the modification of a PETE device where instead of a traditional p-n junction, selective barriers are used.

2.2 HIGH-TEMPERATURE ELECTROLYSIS REACTION

Both high temperature water electrolysis and high temperature water and carbon dioxide co-electrolysis have not only proven to show much higher efficiencies than the same process operated at low temperature, but are also more economically efficient. The reason for this is that at high temperatures, some of the energy needed in the electrolyser is supplied as heat rather than electricity. Similarly, the voltage required to drive the electrolysis reaction reduces, as at higher temperatures, electrochemical equilibrium potentials are reduced. This leads to a decrease in the costs, as lower voltages are needed to power the reactions. The reaction kinetics is also improved, accelerating the rate of hydrogen generation. Moreover, a loss in electrode reactions is achieved, as significantly increasing the temperature lowers the charge transfer overpotentials [7], [19].

Back-reactions in the device are avoided as products are easily released from the electrodes. At low working temperatures, around 25°C (temperatures lower than 100°C), water used in the water electrolysis reaction exists as liquid phase, meaning that detachment of the hydrogen bubbles produced takes a certain time. As a consequence, the risk of backwards reaction exists. Meanwhile, at higher temperatures, the water is present in gaseous phase so H_2 detachments from the cathode surface occur at a higher speed. This also means the product is produced faster. At the same time, we avoid reaching very high temperatures, as that would lead to material thermal degradation problems [19], [20].

Solid oxide electrolysis cells represent a potential technology to store surplus renewable energy in the form of valuable chemicals and fuels.

3. MODEL DESIGN

3.1 DEVICE DESCRIPTION

Technology regarding electrolysers connected to solar cells operating at room temperature already exist. However, such devices are only able to favourably use part of the solar spectrum (the photons with energies higher than the bandgap of the semiconductor). In the current proposed model, all of the incoming solar spectrum is used, as high-energy photons in the solar spectrum (with energies higher than the band gap) are used for driving the electrochemical reaction in the device, while low-energy photons (with energies lower than the band gap energy) are used for heating the species and electrolyser components. The fraction of the solar spectrum absorbed by the photoabsorber causes the photoelectric effect in the solar cell, generating charge carriers, electron-hole pairs in the semiconductor bulk. This leads in turn to the production of a certain photovoltage, which powers the reaction in the electrolyser. The reactants are introduced into the electrolyser, where electrolysis takes place, powered by the electron flow produced in the solar cell, with the final objective of producing hydrogen. The fraction of incoming solar irradiation that is not absorbed by the photoabsorber assembly is used to heat the electrolyser components.

3.1.1 INTEGRATED DEVICE

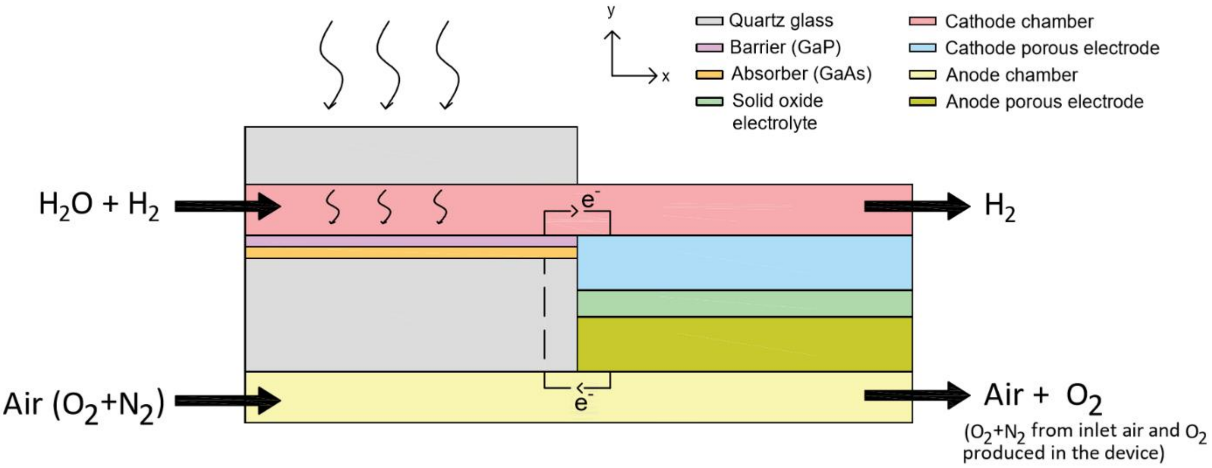

Figure 4- Schematic representation of the integrated device for the hydrogen production simulation.

In this figure the geometrical structure of the integrated device is represented. Quartz glass is placed above the cathode chamber to allow the illumination of the solar cell without covering the rest of the cathode chamber. The device is modelled in this way in order to reduce heat losses by convection and radiation from the glass towards the atmosphere, as this would reduce the performance of the device. Incoming solar energy hits the glass cover, which in turn transmits part of this energy towards the solar cell barrier and reflects part of it to the external atmosphere. Another layer of glass is placed below the solar cell, acting as a support. It is glass used as the supporting material and not any other, due to the fact that if we had a non-transparent material supporting the HTSC, the light that is not absorbed by the photoabsorber assembly will hit directly the supporting material, heating the support and not the device.

Electrons flow from the barrier towards the cathode electrode, in order to power the water splitting reaction. Electrons are then produced in the anode electrode, which are transported back to the semiconductor absorber. This means that current flows from the absorber to the anode, from the anode to the cathode (ionic current), and from the cathode back into the barrier. This is possible by the use of electrical connections between the solar cell and the electrolyser. These connections are not modelled in our device, as they would make the solving of the structure much more complex and time consuming.

In the hydrogen production simulation, water and hydrogen are introduced though the cathode chamber inlet (a portion of hydrogen is needed to be introduced to maintain numerical stability), and air (a mixture of oxygen and nitrogen) enters the device through the anode chamber inlet. Hydrogen fuel is produced in the cathode, exiting the device thought the cathode chamber outlet, and the oxygen produced exits though the anode chamber outlet. Similarly, the same species can be found at the inlet and outlet of the anode chamber in the synthetic gas production simulation. During this second simulation, water, hydrogen, carbon dioxide and carbon monoxide are introduced in the device through the cathode chamber inlet (CO and H_2 are added to maintain numerical stability). The same species would be found at the cathode outlet, but at different proportions.

3.1.2 ELECTROLYSER

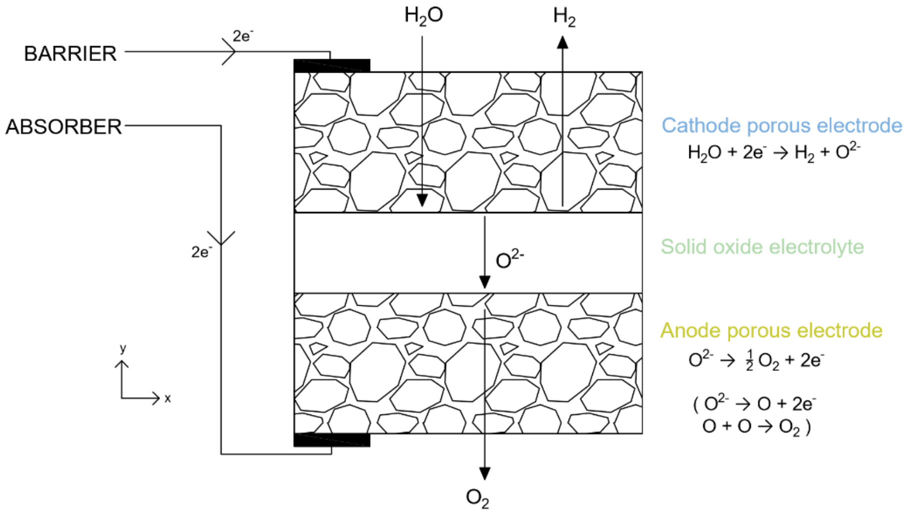

Figure 5- *Schematic representation of the electrolyser for the hydrogen production simulation.*

As previously mentioned, the electrolyser provides high efficiencies at higher temperatures. Solar irradiation does not directly heat the electrolyser components, as no incoming light reaches the SOE, due to the glass cover only being above the photo-absorber assembly. The thermal insulation layer considered as being covering the electrolyser part is assumed as opaque, blocking light to be transmitted. The electrolyser components are heated by conduction from the photoabsorber assembly and indirectly from the bottom of the device.

During the hydrogen production simulation, the water splitting reaction takes place in the high temperature electrolyser. As a flow of electrons is provided from the solar cell towards the cathode electrode, and a mass flow of water is introduced into the cathode chamber, H_2O splits into H_2 and negative oxygen ions in the porous cathode. The hydrogen exits through the cathode outlet, whilst the oxygen ions produced diffuse through the solid electrolyte towards the anode. In this way, the system pumps oxygen ions thorough the solid oxide electrolyte. Oxygen is formed in the anode, which diffuses through the porous electrode and exits though the anode outlet. Finally, the released electrons flow back towards the semiconductor. During the syngas production simulation, *equations 6a*, *6b* and *6c* represent the reactions occurring at the cathode, whilst equation *6d* represents the reaction taking place at the porous anode electrode.

3.1.3 BOUNDARY CONDITIONS

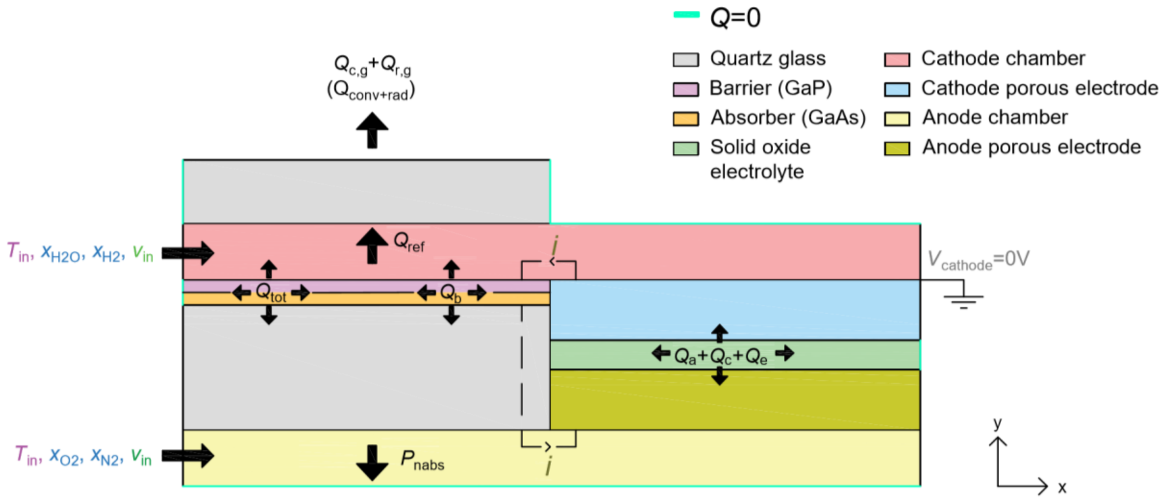

Figure 6*- Representation of the model's boundary conditions for the hydrogen production simulation.*

The parameters that we set in the model for the hydrogen production simulation are shown in *figure 6*. These include the current density, heat sources, voltage at the cathode, inlet velocity, inlet temperature and inlet molar fractions. The difference with respect to the syngas production simulation would be the inlet molar fractions, as we would find, additionally to the ones already shown in the diagram, $x_{\mathrm{CO_2}}$and x_{CO} at the inlet of the cathode chamber. The heat sources shown represent: the heat released and/or absorbed at the electrodes (Q_a, Q_c); the heat released in the solid electrolyte due to joule heating (Q_{e}); the heat lost by convection and radiation into the atmosphere ($Q_{\mathrm{c,g}}$ and $Q_{\mathrm{r,g}}$ respectively); the heat energy reflected at the front of the photoabsorber (Q_{ref}); the part of the solar energy transmitted through the photoabsorber (P_{nabs}); the volumetric heat source inside the photoabsotber device ($Q_{\mathrm{tot}} = Q_{\mathrm{t}} + Q_{\mathrm{j}} + Q_{\mathrm{rec}} - Q_{\mathrm{sr}}$); and the boundary heat sources at the barrier and absorber ($Q_{\mathrm{b}} = Q_{\mathrm{rec,b}} + Q_{\mathrm{P}} + Q_{\mathrm{lost}}$).

To start with, the air introduced in the anode chamber was composed of 0.21 O_2 and 0.79 N_2 molar fractions. An important factor to be considered is the insulation of the device. Heat is lost though convection and radiation throughout the glass, the cathode and anode chamber inlets are opened, as well as its outlets and the cathode and anode porous electrodes (as these electrodes are porous, species are able to flow through them and escape the device). The rest of the model boundaries is considered as insulated, with Q=0.

3.1.4 HIGH-TEMPERATURE SOLAR CELL

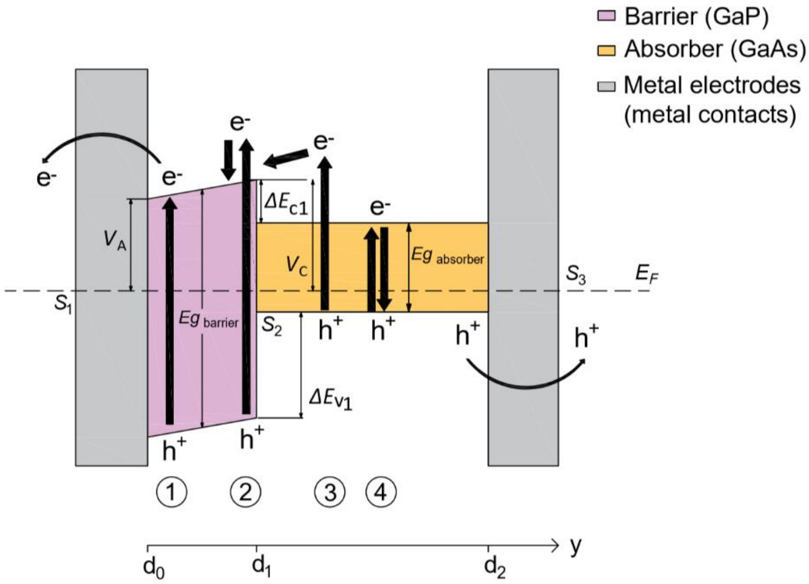

Figure 7- *Band schematics of the HTSC.*

The use of a selective barrier in the high temperature solar cell is used to maintain photogenerated charge carriers separated from one another and to preferentially extract electrons. A wide band gap semiconductor (barrier) is located above a narrow band gap semiconductor (absorber). This geometry allows for a bigger fraction of the incident photons to be absorbed in the absorber, thus producing more photogenerated charge carriers than the barrier. The barrier's high band gap energy means barely any incident photons are absorbed. The role of this layer is primarily carrier extraction, which is consequently a vital part of the selective contact.

The HTSC consists of an absorber, a barrier and 2 electrode contacts placed at each side. The conduction band offset (ΔE_{c1}) between the absorber and the barrier is small, allowing electrons in the absorber's conduction band to be emitted into the barrier. In opposition, the valence band offset (ΔE_{v1}) is much greater, blocking the emission of holes in the absorber's valence band to the barrier. Therefore, this geometrical structure provides low resistance to electrons and high resistance to holes. Electrons are then extracted with the electrode in contact to the barrier, whilst holes are extracted with the electrode below the absorber. The carriers traverse over the barrier by thermionic emission.

As previously mentioned, a similar schematic representation to the one proposed by Yang et al. [12], [18] is applied, however in this case, only one selective contact is used to extract electrons. Charge carrier recombination can also occur on the surface of the metal contact and at the barrier-absorber interface. This model is only accurate when the barrier thickness is smaller than the mean free path of the electrons in the absorber, this is so as electrons can be extracted from the barrier if they are able to travel from the conduction band to the metal contact in a time period smaller than their lifetime.

In *figure 7* we can distinguish 4 different case scenarios. Situation 1 shows the consequence of a high energy photon with $E_{photon} > E_{band\ gap\ barrier}$, which promotes an electron to the barrier's conduction band. A photon with $E_{photon} >>> E_{band\ gap\ barrier}$ is represented in scenario 2. An electron is excited to a higher energy than the barrier's conduction band. The excess energy is lost as heat as the electron returns to the conduction band. In order for an electron to be excited into the barrier's conduction band, it needs to overcome a conduction band offset ΔE_{c1}. In situation 3 a photon with energy $E_{photon} > E_{band\ gap\ absorber}$ reaches the absorber. The electron is provided with energy $E_{band\ gap\ absorber} + \Delta E_{c1}$, so it is able to reach the barrier's conduction band. Scenario 4 shows the absorption in the absorber of a photon with energy $E_{photon} > E_{band\ gap\ absorber}$, however $E_{photon} < E_{band\ gap\ absorber} + \Delta E_{c1}$, so the excited electron reaches the absorber's conduction band, but not the barrier's conduction band. This electron will end up recombining.

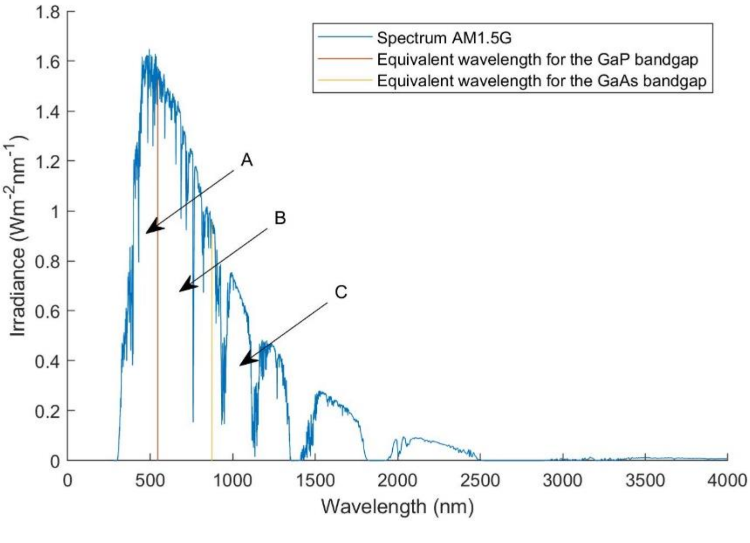

Figure 8- *AM1.5G spectrum.*

Considering $E_{band\ gap\ GaP} = 2.27eV$, $E_{band\ gap\ GaAs} = 1.42eV$ and $E = \frac{hc}{\lambda}$.

A: Represents the fraction of the incident photons absorbed by the GaP material (the barrier). As they have a smaller wavelength than the one for the GaP bandgap ($\lambda_{photon} < \lambda_{band\ gap\ GaP}$), it means they have a higher value of energy than the GaP's band gap energy ($E_{photon} > E_{band\ gap\ GaP}$).

B: Represents the photons that don't have enough energy to be absorbed by the barrier, but have $\lambda_{photon} < \lambda_{band\text{-}gap\ GaAs}$, so $E_{photon} > E_{band\ gap\ GaAs}$, so they are absorbed by the absorber GaAs.

C: Represents the photons with $\lambda_{photon} > \lambda_{band\ gap\ GaAs}$, $E_{photon} < E_{band\ gap\ GaAs}$. These are then not absorbed by the solar cell and its energy is used to heat the electrolyser.

3.2 ALGORITHM

The designed model is separated into two sub-models. These include an 1D model (y-direction) representing the high temperature photoabsorber assembly and solved in Matlab, and a 2D model (x-y direction) representing the solid oxide electrolyser and solved in COMSOL. Both programs are used together in order to solve the operating point of the HTSC-SOE model in each different scenario. By operating point, we mean the values of current density and voltage at which both the photoabsorber and the electrolyser are able to operate together successfully.

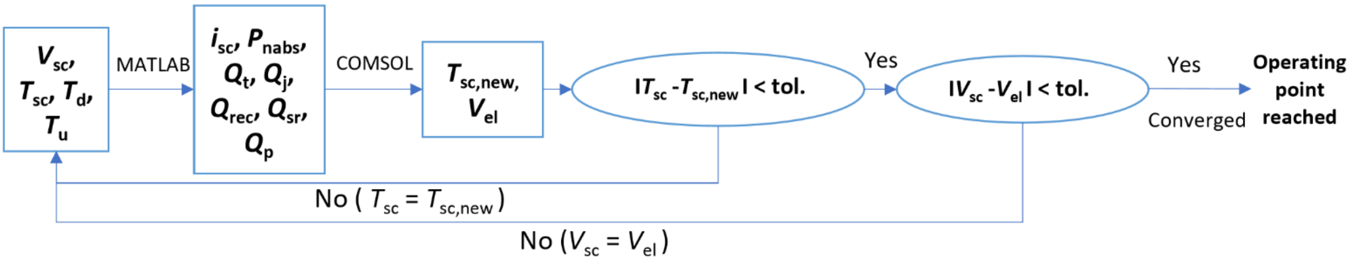

***Figure 9**- Algorithm of the calculation process.*

Figure 9 shows the flow diagram of the basic algorithm used to compute the operating point of the coupled device. This only shows the basic elemental steps which are carried out to complete each iteration and find out whether the device's operating point has been reached or if another iteration must be carried out.

In the computational process, there are 2 loops that are repeated a number of iterations until convergence of the solution is reached, thus the operating point reached. The device is modelled by a one-dimensional model for the HTSC in Matlab (which considers only one axis, in other words, works along the axis connecting the barrier and the absorber), and a two-dimensional model of the solid oxide electrolyser, in COMSOL.

As a concise method, the process of calculation starts by guessing initial temperatures of the HTSC (T_{sc}), the mean temperature of the anode chamber (T_d) and the mean temperature of the cathode chamber (T_u) for a given solar concentration (C) and applied voltage in the solar cell (V_{sc}). This first step is required as the equations used to solve the HTSC model are temperature-dependent. Using these initial values, the set of equations introduced in Matlab for the HTSC model, calculate the current density of the solar cell (i_{sc}) and the heat sources in it (P_{nabs}, Q_{tot}, Q_b). These values are then introduced as inputs for the SOE model into COMSOL, which computes the new calculated value of the solar cell temperature, $T_{sc,new}$ (along with other parameters, including the temperature field in the model and the voltage required to drive the electrolyser, V_{el}).

Once this step is reached, a comparison between the initial value of T_{sc} and the calculated one is made. If the difference between them is smaller than the given tolerance, the voltage required to drive the electrolyser (V_{el}, computed in the SOE model in COMSOL) is compared to the initial V_{sc}. A second comparison is made here. If the difference between them is smaller than a fixed tolerance, the solution converges, and we have reached the operating point. If, however in the first comparison, the difference between the 2 temperatures doesn't satisfy the requirement of being lower than a certain tolerance, the equations of the HTSC model are computed all again, using as input temperature the "new solar cell temperature", $T_{sc,new}$ calculated in the previous iteration. If it is the second comparison is the one which isn't satisfied, again, all the process starts again, setting the photovoltage in the solar cell for this new iteration is equal to the voltage required in the electrolyser computed in the previous iteration. In other word, the process of comparing the temperatures is repeated for several photovoltages, until the difference between the required voltage in the electrolyser and the given photovoltage is smaller than a tolerance. Once this is done, the converged voltage corresponds to the operating point of the integrated HTSC-SOE device.

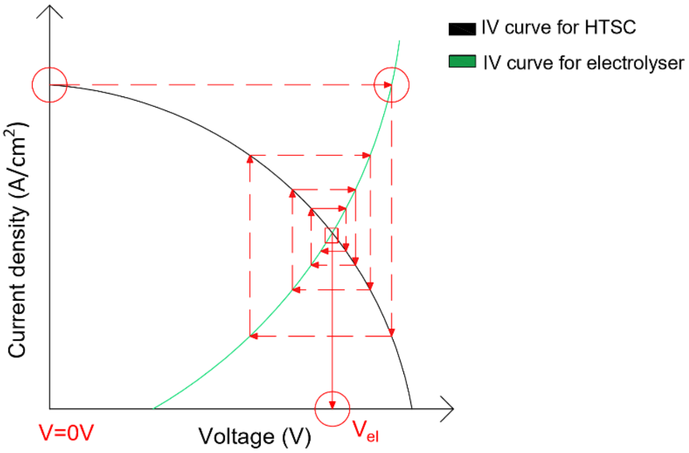

Figure 10- *Procedure followed to calculate the operating point of the HTSC-SOE device.*

3.3 EQUATIONS

3.3.1 HIGH-TEMPERATURE SOLAR CELL MODEL

A series of equations are used in Matlab to compute the high-temperature solar current density and the heat sources in the HTSC.

In first place, Poisson's equation (*2a*) is used to calculate the electric field in the semiconductor and thus to know the steepness of the band bending in the barrier. The life time of electrons and holes is computed using equation (*2b*), by making use of the three recombination mechanisms that can occur, the Shockley-Read-Hall recombination lifetime, the Auger recombination lifetime and the radiative recombination lifetime. The total recombination rate of the minority carriers in each material is the sum of the multiple processes, and inverse lifetimes are additive. The parameters used to compute the photogenerated carrier's lifetimes are shown in *table 1*. Both the electric field E calculated in eq. *2a* and the minority carrier's lifetimes calculated in eq. *2b* are used as input parameters in the continuity-transport equation (*2c*), which is used to compute the minority charge carrier's concentration. Considering that the barrier is n-doped, the hole density is calculated, and as the absorber layer is a p-doped material, the number of electrons is computed. The transport equation represents the balance between the photogenerated charge carriers being diffused (first term) and the ones driven by the electric field caused by the band bending (second term). These two terms represent the movement/transport of carriers, either by diffusion or by drift, and are balanced with recombination (R) and generation (G) of these carriers.

Equation *2c* makes use of boundary conditions for the barrier and the absorber, which take into account surface recombination (S_1, S_2, S_3), as well as the emitted and reversed photocarriers by thermionic emission. These boundary conditions were additionally computed in Matlab. Equations *2d* and *2e* represent the boundary conditions used in the barrier, and equations *2f* and *2g* those in the absorber. In the equations where the subscript 'i' is used, it represents electrons (e) and holes (h). With this, *equations 2d* and *2e* represent the boundary conditions in the barrier, and *equations 2f* and *2g*, those in the absorber.

The energy equation for the HTSC was not solved in Matlab, but rather in COMSOL.

$$\nabla^2\emptyset = -\frac{dE}{dy} = \frac{q}{\varepsilon}\left(n_{\mathrm{eq,e}} - n_{\mathrm{eq,h}} + N_{\mathrm{A}} - N_{\mathrm{D}}\right) \qquad (2a)$$

$$\frac{1}{\tau_i} = \frac{1}{\tau_{\mathrm{srh},i}} + \frac{1}{\tau_{\mathrm{aug},i}} + \frac{1}{\tau_{\mathrm{rad},i}} = \frac{1}{\tau_{\mathrm{srh},i}} + C_i \cdot n_{\mathrm{eq},i}^2 + B \cdot n_{\mathrm{eq},i} \qquad (2b)$$

$$D_i \frac{d^2 n_i}{dy^2} \pm \mu_i \frac{d(E \cdot n_i)}{dy} = R - G = \frac{n_i}{\tau_i} - G \qquad (2c)$$

$$D_{\mathrm{h}} \frac{dn_{\mathrm{h}}}{dy}\bigg|_{y=0} = n_{\mathrm{h}} \cdot S_1 \qquad (2d)$$

$$D_{\mathrm{h}} \frac{dn_{\mathrm{h}}}{dy}\bigg|_{y=d_1} = n_{\mathrm{h}} \cdot S_2 \qquad (2e)$$

$$D_{\mathrm{e}} \frac{dn_{\mathrm{e}}}{dy}\bigg|_{y=d_1} = n_{\mathrm{e}} \cdot S_2 + \frac{J_{\mathrm{em}} - J_{\mathrm{rev}}}{q} \qquad (2f)$$

$$D_{\mathrm{e}} \frac{dn_{\mathrm{e}}}{dy}\bigg|_{y=d_2} = -n_{\mathrm{e}} \cdot S_3 \qquad (2g)$$

Table 1- *Values of the parameters describing the three recombination mechanisms used to compute the lifetime of photogenerated charge carriers* [1].

	GaP	**GaAs**
B (cm^3/s)	3e-15	1e-10
C_{e} (cm^6/s)	5e-30	5e-30
C_{h} (cm^6/s)	3e-30	3e-30
$\tau_{\mathrm{srh,e}}$ (s)	1e-7	5e-9
$\tau_{\mathrm{srh,h}}$ (s)	1e-6	3e-6

The emitted and reversed photocurrents, and the total photocurrent are calculated in *equations 3a, 3b* and *3d*. The current density emitted from the absorber to the barrier (emitted electrons from the absorber: J_{em}) and the current density flowing from the barrier to the absorber (reversed photocurrent from the metal electrode: J_{rev}) have a dependency on the temperature of the solar cell at each point in the device (local temperature: T_{sc}), on the relative work function of the absorber (V_{c}) and of the electrode (V_{a}), the operating voltage (V_{sc}), Richardson constant (A) and the flat band potential ($V_\mathrm{fb} = V_\mathrm{C} - V_\mathrm{A}$). The last being the potential required for the semiconductor band edges to return to their flat band position from the bending position in the junction. The physical representation of these parameters can be observed in *figure 7*. Both relative work functions are measured from the barrier's conduction band and represent the minimum amount of energy required by the electrons to escape from the metal surface, and to be emitted from the absorber to the barrier.

The total photocurrent (*3d*) is calculated by adding the electron and hole current densities (*3c*), which represent the currents of each minority carrier flowing at the interface between the barrier and the absorber. The total electron and hole current densities are the sum of the drift due to the electric field E and the diffusion due to the concentration gradient components.

$$J_\mathrm{em} = \begin{cases} AT_\mathrm{sc}^2 \cdot exp\left(-\dfrac{V_\mathrm{C}}{k_B T_\mathrm{sc}}\right) \cdot \dfrac{n_\mathrm{e} + n_\mathrm{eq,e}}{n_\mathrm{eq,e}}, & V_\mathrm{sc} \le V_\mathrm{fb} \\ AT_\mathrm{sc}^2 \cdot exp\left(-\dfrac{V_\mathrm{C} + V_\mathrm{sc} - V_\mathrm{fb}}{k_B T_\mathrm{sc}}\right) \cdot \dfrac{n_\mathrm{e} + n_\mathrm{eq,e}}{n_\mathrm{eq,e}}, & V_\mathrm{sc} > V_\mathrm{fb} \end{cases} \qquad (3a)$$

$$J_\mathrm{rev} = \begin{cases} AT_\mathrm{sc}^2 \cdot exp\left(-\dfrac{V_\mathrm{A} + V_\mathrm{fb} - V_{sc}}{k_B T_\mathrm{sc}}\right), & V_\mathrm{sc} \le V_\mathrm{fb} \\ AT_\mathrm{sc}^2 \cdot exp\left(-\dfrac{V_\mathrm{A}}{k_\mathrm{B} T_\mathrm{sc}}\right), & V_\mathrm{sc} > V_\mathrm{fb} \end{cases} \qquad (3b)$$

$$J_i(y) = q\mu_i n_i(y)E(y) \pm qD_i \frac{dn_i(y)}{dy} \qquad (3c)$$

$$J(y) = J_\mathrm{e}(y) + J_\mathrm{h}(y) \qquad (3d)$$

In the equations where the subscript 'i' is used, it represents electrons (e) and holes (h), and when the sign ± appears, the positive sign is used for the electron case.

An energy balance (*4a*) is carried out to compute the temperature and heat sources of the high-temperature solar cell. In this study we assume an initial temperature for the HTSC of $T_\mathrm{sc,guess}$ with which the heat sources are calculated, and become inputs in the COMSOL model.

This balance considers various heat sources including heat lost by thermalisation Q_t (when E_{photon}>>>$E_{band\ gap}$, the excess energy is released as heat), Joule heating Q_j (due to the electric field in the interface between the barrier and absorber), the heat produced due to recombination of charge carriers (nonradiative recombination) Q_rec (due to the two recombination mechanisms present) and the self-radiation from the solar cell or local radiative heat source Q_sr (due to the balance between the absorption and thermal emission in the solar cell volume, in other words, to the internal radiation from inside the solar cell). In the balance, the first term represents the gradient of heat released by conduction, whilst the rest represent the different heat sources.

This balance requires two boundary conditions (one for holes in the barrier and another for electrons in the absorber), which take into account the heat sources on the surface of the metal contacts and the Peltier losses (that occur when different materials are placed together, as losses are generated by current flow at metal-semiconductor interface). These last ones are due to surface recombination of the photogenerated carriers. Internal heat conduction and heat losses due to convection at the HTSC's boundaries are also considered. In *equation 4b*, the term on the right-hand side of the equation represents the convection losses between the barrier and the cathode chamber. Meanwhile in equation 4c, the term on the right of the equation stands for the conduction heat transfer from the absorber to the glass support beneath it. We do not consider heat transfer by radiation neither in the barrier nor absorber.

$$\begin{aligned}\nabla\big(k_{\mathrm{c}}(y)\nabla T_{\mathrm{sc}}(y)\big) &= Q_{\mathrm{t}}(y) + Q_{\mathrm{j}}(y) + Q_{\mathrm{rec}}(y) - Q_{\mathrm{sr}}(y)\\ &= Q_{\mathrm{t}}(y) + J(y)\cdot E(y) + R(y)\Big(E_{\mathrm{g}}(y) + 3kT_{\mathrm{sc}}(y)\Big) - Q_{\mathrm{sr}}(y) \qquad (4a)\end{aligned}$$

$$-k_c \left.\frac{dT_{\mathrm{sc}}}{dy}\right|_{y=0} + S_1\big(E_{\mathrm{g}} + 3k_{\mathrm{c}}T_{\mathrm{sc}}\big)n_{\mathrm{h}} + (E_{\mathrm{C}} - E_{\mathrm{Fn}})J = \ h_{\mathrm{c,f}}\big(T_{\mathrm{sc}} - T_{\mathrm{c,ch}}\big) \qquad (4b)$$

$$-k_c \left.\frac{dT_{\mathrm{sc}}}{dy}\right|_{y=d_2} + S_3\big(E_{\mathrm{g}} + 3k_{\mathrm{c}}T_{\mathrm{sc}}\big)n_{\mathrm{e}} + \big(E_{\mathrm{V}} - E_{\mathrm{Fp}}\big)J = Q_{\mathrm{conduction,glass}} \qquad (4c)$$

3.3.2 ELECTROLYSER MODEL

Regarding the electrolyser, we aim to simulate the H_2O, and H_2O and CO_2 electrolysis reactions. COMSOL is used to solve the high-temperature electrolyser model. The electrochemical reactions, thermochemical reactions, fluid dynamics, transport of concentrated species, free and porous media flow and heat transfer though porous media is considered in this section.

The thermochemical reactions happening in the electrolyser during water electrolysis are the ones that follow, *5a* being the overall reaction, *5b* the half reaction at the porous cathode electrode and *5c* the half reaction at the porous anode electrode.

$$\mathrm{H_2O} \leftrightarrow \mathrm{H_2} + \frac{1}{2}\mathrm{O_2} \qquad (5a)$$

$$\mathrm{H_2O} + 2\mathrm{e^-} \rightarrow \mathrm{H_2} + \mathrm{O^{2-}} \qquad (5b)$$

$$\mathrm{O^{2-}} \rightarrow \frac{1}{2}\mathrm{O_2} + 2\mathrm{e^-} \qquad (5c)$$

Meanwhile, during the syngas generation scenario, the reactions occurring and the porous cathode electrode are shown in *equations 6a* to *6c*, and the thermochemical half reaction within the porous anode electrode is shown in *equation 6d*.

$$\mathrm{H_2O} + 2\mathrm{e^-} \rightarrow \mathrm{H_2} + \mathrm{O^{2-}} \qquad (6a)$$

$$\mathrm{CO_2} + 2\mathrm{e^-} \rightarrow \mathrm{CO} + \mathrm{O^{2-}} \qquad (6b)$$

$$\mathrm{H_2O} + \mathrm{CO} \leftrightarrow \mathrm{H_2} + \mathrm{CO_2} \qquad (6c)$$

$$2\mathrm{O_2} \rightarrow \mathrm{O_2} + 4\mathrm{e^-} \qquad (6d)$$

The electrochemical model is solved in order to determine the electrolyser's operating voltage V_e (*equation 7a*). This is done considering the equilibrium potential for the half reaction in the anode (7*b*), the equilibrium potential for the half reaction at the cathode (*7c*), the activation overpotentials at the cathode and anode (additional voltage needed in each element to drive the reaction) and the ohmic resistance in the electrolyte and electrodes. This last parameter is mainly due to the resistance of the movement of negative oxide ions though the electrolyte. Equation *7b* uses the Nernst equation to calculate the equilibrium potential for the anode's half reaction and *7c* does the same for the cathode's half reaction.

Equation *7d* and *7f* are used together to compute the overpotentials at the cathode and at the anode. Equations $7d_a$ and $7d_b$ calculate the exchange current densities at the anode and the cathode respectively, whilst $7e_a$ and $7e_b$ are solved for the molar flow rate of O_2 and H_2 at the anode and cathode, respectively. The equilibrium potentials are partial pressure and temperature dependent. The exchange current density follows and Arrhenius-type behaviour with regard to its dependence on temperature.

The ohmic overpotential is determined in equation *7i* with the use of the ionic conductivities of the electrodes and solid electrolyte computed in equations *7g* and 7*h*, respectively.

$$V_\mathrm{e} = E_{\mathrm{O_2}} - E_{\mathrm{H_2/CO}} + \eta_{\mathrm{O_2}} + \eta_{\mathrm{H_2/CO}} + \eta_{\mathrm{ohm}} \qquad (7a)$$

$$E_{\mathrm{O_2}} = E^{\circ}_{\mathrm{O_2}} - \frac{RT}{nF} \cdot \ln\left(\frac{1}{p_{\mathrm{O_2,ref}}}\right) \qquad (7b)$$

$$E_{\mathrm{H_2/CO}} = E^{\circ}_{\mathrm{H_2/CO}} - \frac{RT}{nF} \cdot \ln\left(\frac{p_{\mathrm{H_2/CO,\,ref}}}{p_{\mathrm{H_2O/CO_2,\,ref}}}\right) \qquad (7c)$$

$$i_{0,\mathrm{O_2}}(x,y) = k_{\mathrm{O_2}} \cdot exp\left(-\frac{E_{\mathrm{act,O_2}}}{R \cdot T_{\mathrm{anode}}(x,y)}\right) \cdot \left(\frac{p_{\mathrm{O_2}}(x,y)}{p_{\mathrm{O_2,ref}}}\right)^{-\alpha_\mathrm{a}} \qquad (7d_a)$$

$$i_{0,\mathrm{H_2/CO}}(x,y) = k_{\mathrm{H_2/CO}} \cdot exp\left(-\frac{E_{\mathrm{act,H_2/CO}}}{R \cdot T_{\mathrm{cathode}}(x,y)}\right) \cdot \left(\frac{p_{\mathrm{H_2/CO}}(x,y)}{p_{\mathrm{H_2/CO,\,ref}}}\right)^{-\alpha_\mathrm{c}} \cdot \left(\frac{p_{\mathrm{H_2O/CO_2}}(x,y)}{p_{\mathrm{H_2O/CO_2,\,ref}}}\right)^{-\alpha_\mathrm{a}} \qquad (7d_b)$$

$$n_{\mathrm{O_2}} = \frac{i_{\mathrm{O_2}}}{nF} \qquad (7e_a)$$

$$n_{\mathrm{H_2/CO}} = \frac{i_{\mathrm{H_2/CO}}}{nF} \qquad (7e_b)$$

$$i_{\mathrm{O_2}}(x,y) = a_\mathrm{V} \cdot i_{0,\mathrm{O_2}}(x,y) \cdot \left(exp\left(\frac{\alpha_\mathrm{a} nF \cdot \eta_{\mathrm{O_2}}(x,y)}{R \cdot T_{\mathrm{anode}}(x,y)}\right) - \frac{p_{\mathrm{O_2}}(x,y)}{p_{\mathrm{O_2,ref}}} \cdot exp\left(\frac{-\alpha_\mathrm{c} nF \cdot \eta_{\mathrm{O_2}}(x,y)}{R \cdot T_{\mathrm{anode}}(x,y)}\right)\right) \qquad (7f_a)$$

$$\begin{aligned} i_{\mathrm{H_2/CO}}(x,y) = {} & a_\mathrm{V} \cdot i_{0,\mathrm{H_2/CO}}(x,y) \\ & \cdot \left(\frac{p_{\mathrm{H_2/CO}}(x,y)}{p_{\mathrm{H_2/CO,\,ref}}} \cdot exp\left(\frac{\alpha_\mathrm{a} nF \cdot \eta_{\mathrm{H_2/CO}}(x,y)}{R \cdot T_{\mathrm{cathode}}(x,y)}\right) - \frac{p_{\mathrm{H_2O/CO_2}}(x,y)}{p_{\mathrm{H_2O/CO_2,\,ref}}}\right. \\ & \left. \cdot\, exp\left(\frac{-\alpha_\mathrm{c} nF \cdot \eta_{\mathrm{H_2/CO}}(x,y)}{R \cdot T_{\mathrm{cathode}}(x,y)}\right)\right) \qquad (7f_b) \end{aligned}$$

$$\sigma_{\mathrm{a,c}}(x,y) = \frac{\sigma^{\circ}_{\mathrm{a,c}}}{T_{\mathrm{a,c}}(x,y)} \cdot exp\left(-\frac{E_{\mathrm{a,c}}}{k \cdot T_{\mathrm{a,c}}(x,y)}\right) \qquad (7g)$$

$$\sigma_{\mathrm{elec}}(x,y) = \overset{\circ}{\sigma}_{\mathrm{elec}} \cdot exp\left(-\frac{E_{\mathrm{elec}}}{k \cdot T(x,y)}\right) \qquad (7h)$$

$$\eta_{\mathrm{ohm}} = \phi_{\mathrm{I,anode}} - \phi_{\mathrm{I,cathode}} \qquad (7i)$$

In this set of equations, the sub-indices H_2, CO and O_2 distinguish between the products of the redox reaction at the cathode and at the anode.

Table 2- *Values used to compute the activation and ohmic overpotentials at the cathode and anode* [1].

Parameter	**Value**	**Material**
Activation energy, $E_{\mathrm{act,H_2}}$ (Jmol^{-1})	1e5	Ni-YSZ
Pre-exponential factor, $k_{\mathrm{H_2}}$ (Am^{-2})	3.911e8	
Asymmetry factor, $\alpha_{\mathrm{H_2}}$ (-)	0.5	
Activation energy, E_{c} (eV)	0.099	
Pre-exponential factor, $\overset{\circ}{\sigma}_{\mathrm{c}}$ (SKm^{-1})	9.5e7	
Specific surface area, $a_{\mathrm{v,c}}$ (m^{-1})	1.025e5	
Activation energy, $E_{\mathrm{act,O_2}}$ (Jmol^{-1})	1.2e5	LSM-YSZ
Pre-exponential factor, $k_{\mathrm{O_2}}$ (Am^{-2})	1.389e9	
Asymmetry factor, α_{O_2} (-)	0.5	
Activation energy, E_{a} (eV)	0.103	
Pre-exponential factor, $\overset{\circ}{\sigma}_{\mathrm{a}}$ (SKm^{-1})	4.2e7	
Specific surface area, $a_{\mathrm{v,a}}$ (m^{-1})	1.025e5	
Activation energy, E_{elec} (Jmol^{-1})	0.887	YSZ
Pre-exponential factor, $\overset{\circ}{\sigma}_{\mathrm{elec}}$ (Sm^{-1})	33.4e3	
Activation energy, $E_{\mathrm{act,O_2}}$ (Jmol$_{-1}$)	0.602	CGO
Pre-exponential factor, $\overset{\circ}{\sigma}_{\mathrm{elec}}$ (Sm^{-1})	8.7e4/T	

Table 2 doesn't show the parameters concerning CO as $i_{\mathrm{CO,0}}$ is computed based on $i_{\mathrm{H_2,0}}$.

As pressures and velocities are needed in the electrochemical model and heat transfer model respectively, the free and porous media flow model is proposed. The pressure and velocity field are computed using the Navier-Stoles and continuity equation in the fluid region (chambers) with equations *8a* and 8*b*, and the Stokes-Brinkmann and continuity equations in the porous region (electrodes) with equations *8c* and *8d*. The velocity field varies as the species flow at different velocities in different media, for example, the speed of flow is higher in the free media (chambers) than in the porous media (electrodes). In equation *8d*, the term Q_{br} represents the addition of mass due to the electrochemical reactions occurring in the electrolyser (oxygen and hydrogen are produced). The assumptions taken into consideration in these equations are the inlet velocity being laminar, the velocity in the solid electrolyte-porous electrode interface being zero and no back-flow present in the outlet of both chambers.

$$\rho(u \cdot \nabla)u = \nabla \cdot \left[-pI + \mu(\nabla u + (\nabla u)^T) - \frac{2}{3}\mu(\nabla \cdot u)I\right] + F \qquad (8a)$$

$$\nabla \cdot (\rho u) = 0 \qquad (8b)$$

$$\frac{\rho}{\varepsilon_{\mathrm{p}}}\left((u\cdot\nabla)\frac{u}{\varepsilon_{\mathrm{p}}}\right)=\nabla\cdot\left[-pI+\mu(\nabla u+(\nabla u)^{T})-\frac{2\mu}{3\varepsilon_{\mathrm{p}}}\mu(\nabla\cdot u)I\right]-\left(\mu\kappa^{-1}+\beta_{\mathrm{F}}|u|+\frac{Q_{\mathrm{br}}}{\varepsilon_{\mathrm{p}}{}^{2}}\right)u+F \qquad (8c)$$

$$\nabla\cdot(\rho u)=Q_{\mathrm{br}} \qquad (8d)$$

The transport of concentrated species model evaluates the evolution of species throughout the cathode and anode chambers. Equations *9a*, *9b* and *9c* are used for this purpose. The term on the left of *equation 9a* represents the diffusive transport (Maxwell-Stefan diffusion model). The second term on the left relates to the convective transport, and the term on the right-hand side of the equation 8a corresponds to the species sources. Equation 9c shows that this last term involves the generation of species through thermochemical and electrochemical reactions occurring in the electrolyser model. Equation *9c* uses as an input the rate of the water gas shift reaction R_{WGSR}. This parameter is calculated using equations *9d to 9g*. The signs in equation 9c are positive for products.

$$\nabla\cdot j_i+\rho(u\cdot\nabla)\omega_i=R_i \qquad (9a)$$

$$j_i=-\rho\omega_i\sum_k D_{ik}\left(\nabla x_k+\frac{1}{p_{\mathrm{A}}}((x_k-\omega_i)\nabla p_{\mathrm{A}})\right) \qquad (9b)$$

$$R_i=\pm\frac{v_i i_{\mathrm{v}}}{nF}\pm R_{\mathrm{WGSR}}M_i \qquad (9c)$$

$$R_{\mathrm{WGSR}}=k_{\mathrm{sf}}\left(p_{\mathrm{H_2O}}p_{\mathrm{CO}}-\frac{p_{\mathrm{H_2}}p_{\mathrm{CO_2}}}{K_{\mathrm{ps}}}\right)(molm^{-3}s^{-1}) \qquad (9d)$$

$$k_{\mathrm{sf}}=0.0171exp\left(-\frac{103191}{RT}\right)(molm^{-3}Pa^{-2}s^{-1}) \qquad (9e)$$

$$K_{\mathrm{ps}}=\exp\left(-0.2935Z^3+0.6351Z^2+4.1788Z+0.3169\right) \qquad (9f)$$

$$Z=\frac{1000}{T(K)}-1 \qquad (9g)$$

The temperature at each point in the device (temperature field) and the heat sources are determined in the heat transfer model. The heat transfer equation (*10a*) is used to compute the local temperatures of the device. The volumetric heat sources in the device are taken into account. The term k_{eff} in the energy balance represents the effective conductivity (*10b*), and is calculated as a volume average of the bulk conductivity. Both the Joule heating due to the charge transport in the solid conductors (*10d*) and the heating due to the electrochemical reactions (*10e*) are considered. This last heat source is composed as follows, the first term of the equation represents heat source due to the activation overpotentials (the irreversible activation losses), and the second term represents the heat sink due to the electrochemical reaction (the reversible heat change due to the net change of entropy in the conversion process). In the cathode, this first term is positive whilst the second is negative. Both terms are positive in the case of the anode. Heat losses by convection and radiation through the glass surface towards the environment are taken into account in *equations 10f* and *10g*.

$$\rho C_{\mathrm{p}} u \cdot \nabla T = \nabla \cdot (k_{\mathrm{eff}} \nabla T) + Q \qquad (10a)$$

$$k_{\mathrm{eff}} = \theta_{\mathrm{p}} k_{\mathrm{p}} + (1 - \theta_{\mathrm{p}}) k \qquad (10b)$$

$$Q = Q_{\mathrm{JH}} + Q_{\mathrm{EC}} + Q_{\mathrm{tot}} + Q_{\mathrm{b}} + Q_{\mathrm{r,g}} \qquad (10c)$$

$$Q_{\mathrm{JH}} = -(i_{\mathrm{s}} \nabla \emptyset_{\mathrm{s}} + i_{\mathrm{l}} \nabla \emptyset_{\mathrm{l}}) \qquad (10d)$$

$$Q_{\mathrm{EC}} = \sum_i \left(\eta_i + T \frac{\partial E_i}{\partial T} \right) i_i \qquad (10e)$$

$$Q_{\mathrm{r,g}} = \varepsilon \sigma A (T^4 - T_{\mathrm{amb}}^4) \qquad (10f)$$

$$Q_{\mathrm{c,g}} = h (T^4 - T_{\mathrm{amb}}^4) \qquad (10g)$$

3.3.3 ENERGY BALANCE IN THE INTEGRATED DEVICE

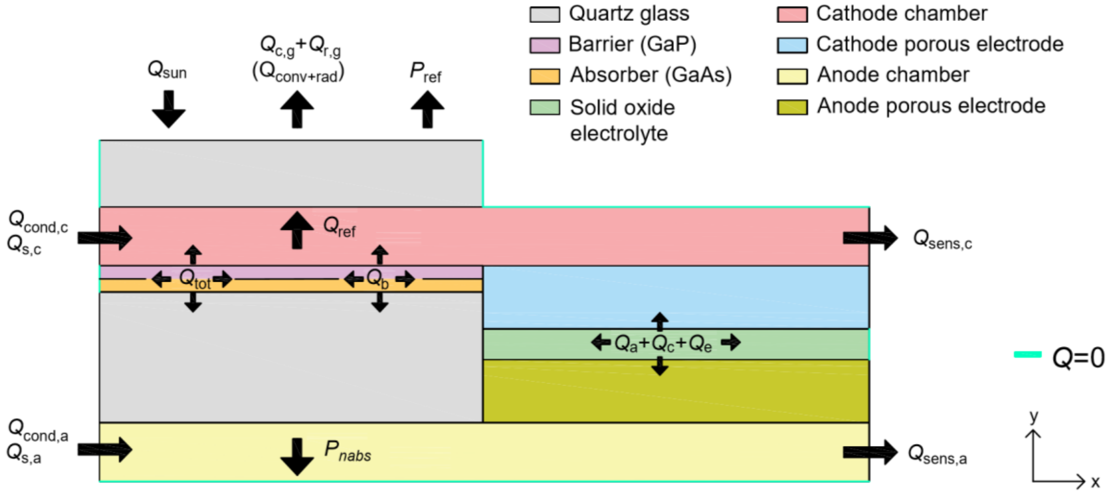

Figure 11- Heat sources in the integrated device.

An energy balance has to be considered in the integrated device to verify of our results.

Equation 11 is a heat transfer equation and solves the temperature in the HTSC and electrolyser. On the other hand, *equation 15* represents the balance for the whole device.

For the heat energy reaching the solar cell in the device, the energy entering (Q_{sun}) must be equal to the energy coming out of the system ($P_{\mathrm{ref}}, Q_{\mathrm{ref}}, P_{\mathrm{nabs}}$) plus the energy used inside it absorbed by the solar cell (Q_{absorbed}). In other words, for the energy balance in the HTSC, the entering energy must be equal to the exiting energy of the system:

$$Q_{\mathrm{sun}} = P_{\mathrm{ref}} + Q_{\mathrm{ref}} + Q_{\mathrm{absorbed}} + P_{\mathrm{nabs}} \qquad (11a)$$

$$Q_{\mathrm{sun}} = P_{\mathrm{ref}} + Q_{\mathrm{ref}} + (\,P_{\mathrm{sc}} + Q_{\mathrm{losses}}) + P_{\mathrm{nabs}} \qquad (11b)$$

$$Q_{\mathrm{sun}} = P_{\mathrm{ref}} + Q_{\mathrm{ref}} + (\,P_{\mathrm{sc}} + (Q_{tot} + Q_{\mathrm{b}})) + P_{\mathrm{nabs}} \qquad (11c)$$

$$Q_{\mathrm{sun}} = P_{\mathrm{ref}} + Q_{\mathrm{ref}} + (\,P_{\mathrm{sc}} + (Q_{\mathrm{t}} + Q_{\mathrm{j}} + Q_{\mathrm{rec}} - Q_{\mathrm{sr}}) + (Q_{\mathrm{rec,b}} + Q_{\mathrm{P}} + Q_{\mathrm{lost}})) + P_{\mathrm{nabs}} \qquad (11d)$$

From equation *11a* to *11b*: $Q_{\mathrm{absorbed}} = Q_{\mathrm{sc}} + Q_{\mathrm{losses}}$, from *11b* to *11c*: $Q_{\mathrm{losses}} = Q_{\mathrm{tot}} + Q_{\mathrm{b}}$ and from *11c* to *11d*: $Q_{\mathrm{tot}} = Q_{\mathrm{t}} + Q_{\mathrm{j}} + Q_{\mathrm{rec}} - Q_{\mathrm{sr}}$; $Q_{\mathrm{b}} = Q_{\mathrm{rec,b}} + Q_{P} + Q_{\mathrm{lost}}$.

The following Sankey diagram shows, graphically, the reasonable weight of the heat sources into which the incoming solar energy is divided in the HTSC. In other words, it illustrates *equation 11d*. Q_{lost} represents the difference between all the heat sources and the incoming solar radiation, it is used to close the balance. During this report, we combined this heat lost with the one due to the Peltier effect, in order to plot the resuts. This is why Q_{lost} does not appear neither in the sankey diagram nor in the bar plots of the results.

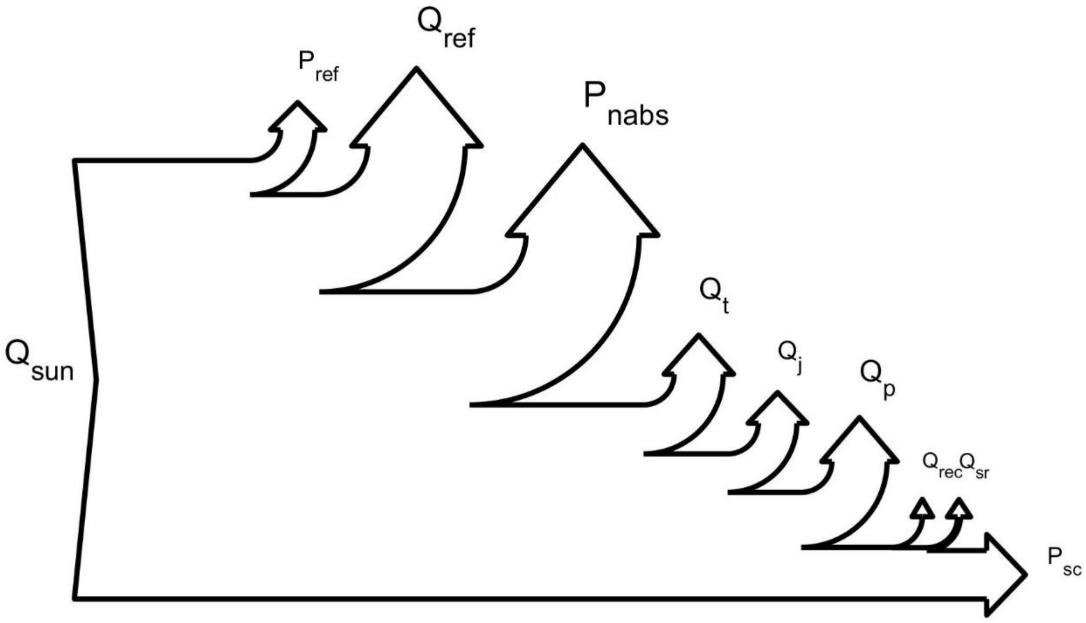

Figure 12- *Sankey diagram representing the energy breakdown of the incoming solar energy in the HTSC.*

In *figure 12*, the parameter named Q_{rec} represents $Q_{\mathrm{rec}} + Q_{\mathrm{rec,b}} + Q_{\mathrm{lost}}$ in *equation 11d*. P_{nabs} represents the portion of the solar energy that is not absorbed by the photoabsorber assembly and heats directly the internal elements of the device by convection. Meanwhile, P_{sc} is the energy used in the solar cell to produce electrical power (produced energy inside the solar cell).

Applying the first law of thermodynamics for open systems to the electrolyser system, the net amount of energy added into the system is contained in the electrolyser fluids, in the form of sensible heat ($Q_{\mathrm{s},i}$), conduction ($Q_{\mathrm{cond},i}$) and chemical energy (P_{fuel}):

$$Q_{\mathrm{s}} - W_{\mathrm{s}} = Q_{\mathrm{s,a}} + Q_{\mathrm{cond,a}} + Q_{\mathrm{s,c}} + Q_{\mathrm{cond,c}} + P_{\mathrm{fuel}} \qquad (12)$$

Where Q_s and W_s represent the added or removed heat and power into the system, respectively.

$$Q_{\mathrm{s}} - W_{\mathrm{s}} = Q_{\mathrm{ref}} + Q_{\mathrm{t}} + Q_{\mathrm{j}} + Q_{\mathrm{rec}} - Q_{\mathrm{sr}} + Q_{\mathrm{rec,b}} + Q_{\mathrm{P}} + Q_{\mathrm{lost}} + P_{\mathrm{nabs}} - \left(Q_{\mathrm{c,g}} + Q_{\mathrm{r,g}}\right) + P_{\mathrm{sc}} \qquad (13)$$

Replacing *equation 13* into *11*:

$$Q_{\mathrm{sun}} = P_{\mathrm{ref}} + Q_{\mathrm{s}} - W_{\mathrm{s}} + Q_{\mathrm{c,g}} + Q_{\mathrm{r,g}} \qquad (14)$$

Finally, replacing *eq. 12* into *14* and taking into account numerical errors, a term ΔQ is added to make a perfect balance, to obtain the total energy balance of the whole system:

$$Q_{\mathrm{sun}} = P_{\mathrm{ref}} + Q_{\mathrm{s,a}} + Q_{\mathrm{cond,a}} + Q_{\mathrm{s,c}} + Q_{\mathrm{cond,c}} + P_{\mathrm{fuel}} + Q_{\mathrm{c,g}} + Q_{\mathrm{r,g}} + \Delta\mathrm{Q} \qquad (15)$$

As mentioned, this last equation corresponds to the energy balance of the whole system, considering the total energy input into the system, Q_{sun} is equal to the energy contained inside the fluids in the electrolyser device ($Q_{\mathrm{cond},i}, Q_{\mathrm{s},i}, P_{\mathrm{fuel}}$) plus the energy escaping into the atmosphere ($Q_{\mathrm{ref,1}}, Q_{\mathrm{c,g}}, Q_{\mathrm{r,g}}$).

The following Sankey diagram shows, graphically, a reasonable energy breakdown in the whole integrated device. In other words, it illustrates *equation 15*.

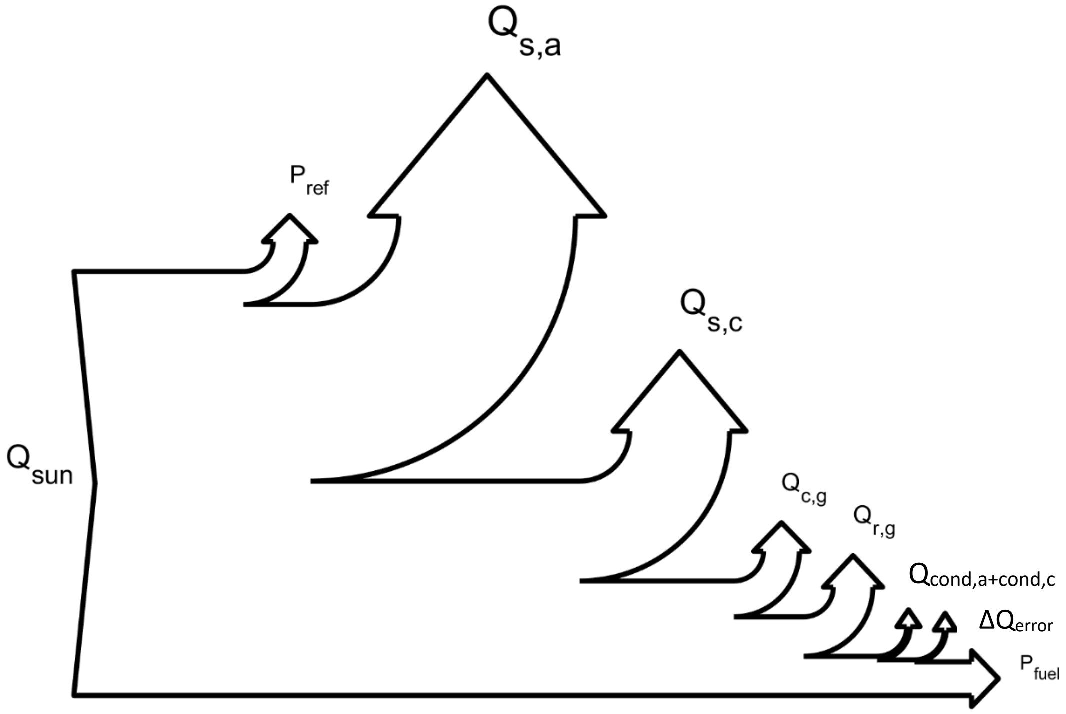

Figure 13- *Sankey diagram representing the energy breakdown of the incoming solar energy in the whole device.*

3.3.4 PERFORMANCE METRICS

The performance of the HTSC-SOE device under each scenario was assessed considering the solar-to-fuel efficiency, η_{STF}, (*equation 16*) and the molar flow rate of hydrogen produced at the outlet of the device, n_i. The molar flow produced is calculated through Faraday's equation using the current density. Faraday's law of electrolysis state that, during and electrochemical reaction, the amount of hydrogen produced at an electrode is directly proportional to the total conducted current [21].

$$\eta_{\text{STF}} = \frac{\sum_{i=1}^{n} n_i \Delta G_i^{\circ}}{C \cdot I_{\text{sun}}} \qquad (16)$$

In both equations, the sub-index i stands for either H_2 or CO. In *equation 16*, n_i represents the molar flow rate of fuel produced at the outlet of the device, ΔG_i° is the Gibbs free energy at 298K ($\Delta G_{\text{H}_2\text{O}}^{\circ} = 237\ kJmol^{-1},\ \Delta G_{\text{CO}_2}^{\circ} = 256.5\ kJmol^{-1}$), C is the solar concentration and I_{sun} the solar radiation (taken as $I_{\text{sun}} = 1000W/m^2$).

3.4 MATLAB AND COMSOL MODELS

A Matlab code was used to carry out the computation of the HTSC's parameters, calculating the 1D heat source distribution in the solar cell and the photocurrent. The studied variables were first specified, and we were able to select between different modalities of the study. Various parameters including the type of reaction, the type of mesh and the type of flow have different options from which the user selects the one needed to carry out a certain simulation. Further into the code, the script calls a specific COMSOL model, depending, as said, on the specific characteristics of the simulation wanted to be carried out, as different COMOL models are designed depending on certain characteristics, such as the type of reaction. Once the model is called, parameters required for the computations are imported from Matlab into COMSOL.

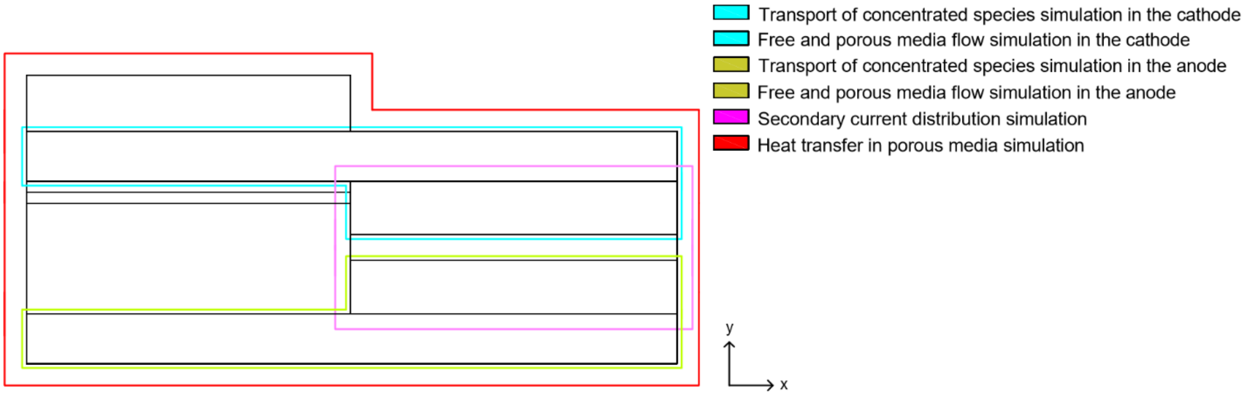

Figure 14- *COMSOL models.*

COMSOL uses a "thin layer" to represent the presence of the HTSC. Due to the small thickness of the solar cell in comparison with the other elements in the device, we avoid adding the barrier and the absorber directly into the geometry of the device, as this would cause problems with the meshing and considerably increase the computational effort. The program then computes the desired plots and parameters with the help of a number of different simulations and models. These include: secondary current distribution simulation, which calculates the heat sources int the electrolyser and the voltage required for it to operate; the transport of concentrated species simulation for the anode and cathode, which is used to calculate the molar fraction of each species present in the electrode and chamber at each point with the use of the Maxwell-Stefan diffusion model; the free and porous media flow for the anode and cathode, with the help of the Navier-Stokes, Stokes-Brinckmann and continuity equations, computes the pressure and velocities of each of the species present; and lastly, the heat transfer in porous media, which computes the temperature distribution, being the temperature at each position in the device.

3.5 DEVICE SETUP

The parameters set for our reference case are the same as the ones used in the quasi-integrated model[13].

Two different materials were analysed for the absorber: Si and GaAs, and assembled them with GaP, the material chosen for the barrier. Each of the two absorber materials were selected as they had a characteristic which made them appealing for the design. Silicon has a small band gap (1.1eV at room temperature), whilst gallium arsenide has a high absorption coefficient, which would allow the use of thinner solar absorbers. Meanwhile, gallium phosphide was chosen as the barrier material due to its large bandgap, which made it a good selective electron contact, and the position of its band levels. Simulations were carried out using the two assemblies GaP/Si and GaP/GaAs under the same conditions, and their results were analysed and compared. The GaP/GaAs assembly was shown to perform better, providing higher current densities and voltages. This was attributed, in first place, to the higher absorption coefficient of the GaAs material, which results in higher generation of photocarriers. Secondly, the higher value of the built-in voltage with this assembly (and so the electric field), which is determined by the relative position of the fermi levels of the barrier and absorber, also favoured the performance.

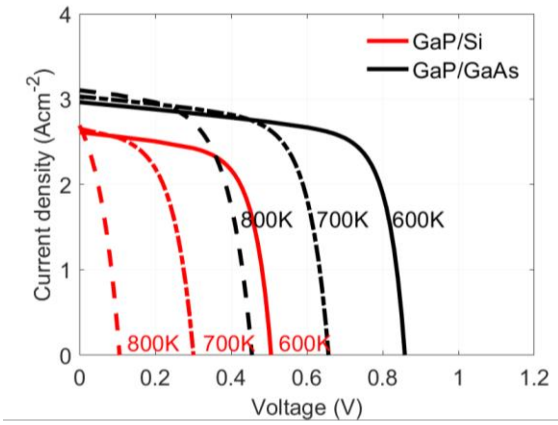

Figure 15- *Current-voltage performance comparison of the HTSC using GaP/Si and GaP/GaAs assemblies, under a temperature of 600K (solid line), 700K (dash-dot line) and 800K (dashed line), and a solar concentration of 100 suns*[13].

A study regarding the material of the electrolyte used was also conducted, where a series of materials were analysed, including yttria-stabilized zirconia (YSZ), gadolinium-doped ceria (CGO), lanthanum strontium gallium magnesium oxide (LGSM) and yttrium doped $BaZrO_3$ (BZY). It was concluded that gadolinium-doped ceria (CGO) was the material which offered the best performance, mainly due to its higher ionic conductivity at lower temperatures than other electrolyte materials. This was the material which was therefore selected as the reference case.

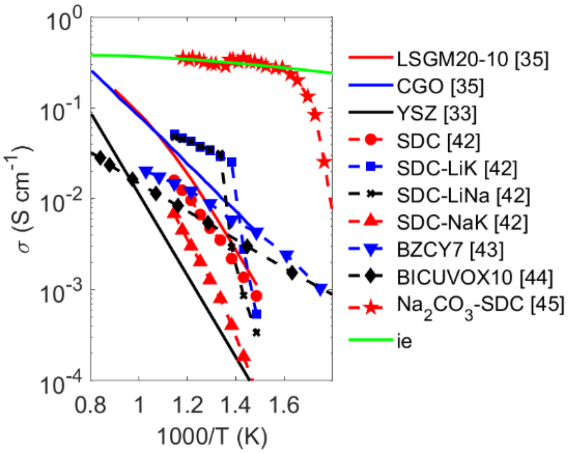

Figure 16- *Ion conductivity as function of the temperature for different electrolytes* [13].

A photoabsorber assembly with four solar cells operating in series was chosen to be used in the reference case. Using only one photoabsorber gave high current densities but low photovoltages which did not allow to power satisfactorily the electrochemical reaction in the electrolyser. Having four photoabsorbers working in series allowed to provide enough photovoltage to the electrolyser, whereas the photocurrent density injected into the electrolyser was reduced.

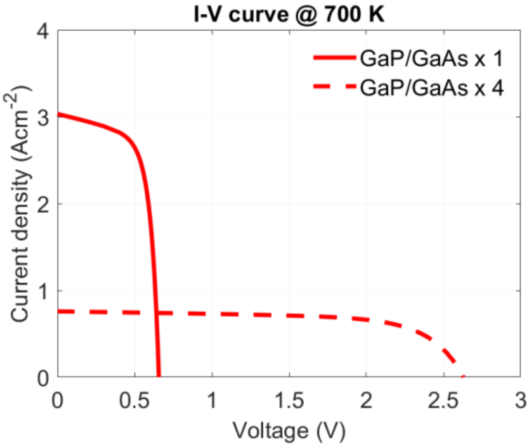

Figure 17- *Current-voltage performance for the case 1 and 4 photoabsorbers operating in series* [13].

3.6 MESH ANALYSIS

A mesh analysis was the first step carried out before beginning the hydrogen and syngas production simulations. The objective of this study was to choose the appropriate mesh in order to carry out the simulations. We run the same simulation, with the same parameters used in each one (these are summarised in *table 3* and *table 5*, for the hydrogen production simulation and syngas production simulation respectively), using a variety of different meshes with different numbers of elements. Increased number of mesh elements led to increased accuracy of the computed results, but also to higher computational efforts. The results were analysed, and the selected mesh for our reference case and parametric study was the one in which the value of the voltage in the electrolyser (V_{el}) started to be stable. This resulting mesh then assures us that the results obtained in the next simulations have an acceptable accuracy and precision with a reasonable computational time.

Finding a compromise between the computational time and efforts and the quality of our results, we performed the mesh analysis considering the solar cell voltage equal to 0V. The Matlab-COMSOL model calculated the voltage required by the electrolyser when the current density provided by the HTSC was generated when the solar cell received no voltage, i.e. at V_{sc}=0V. From a mesh to another, the current density provided by the solar cell at V=0V varies, so the voltage required by the electrolyser will, in consequence, varies.

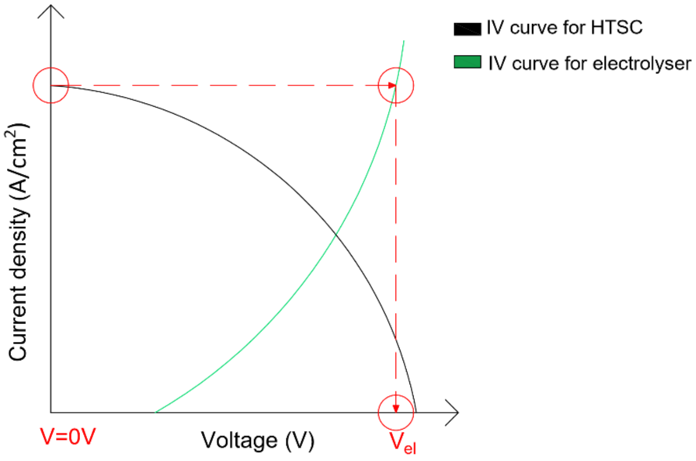

Figure 18- Mesh analysis procedure.

The results of the mesh analysis carried out are shown in *figures 19 to 22*. As we can observe, for the mesh analsis pf the hydrogen production simulation, the calculated value of V_{el} gradually increases until reaching a constant value of 1.632V in the last three meshes. We are also able to observe how the difference in calculated values of V_{el} obtained from one mesh to the other drastically decreases the first meshes, and then does so gradually, as convergence is approached. The desired flat behaviour of the curve is obtained. In conclusion, the mesh chosen as the reference case is the one containing a total number of 1049048 triangular elements in the mesh. This was the first mesh to obtain the commented value of 1.632V. It is not only chosen for that reason, but the time taken to compute the value is low in comparison with the next two iterations, meaning less computational effort is required.

Similarly, the mesh analysis carried out for the syngas production simlation showed the desired flat behaviour of the curve was reached with a mesh of 908595 triangular elements, obtaining a value of V_{el} of 1.625V. As a consecuence, this was the mesh chosen for the reference case of this simulation.

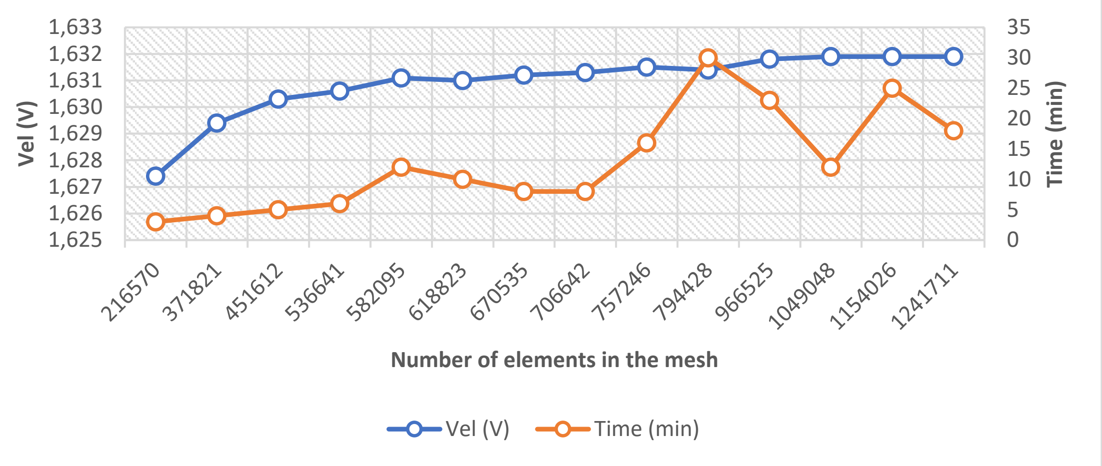

Figure 19- *Mesh analysis results for hydrogen production simulation (V_{el} vs Number of elements in the mesh and Time vs Number of elements in the mesh).*

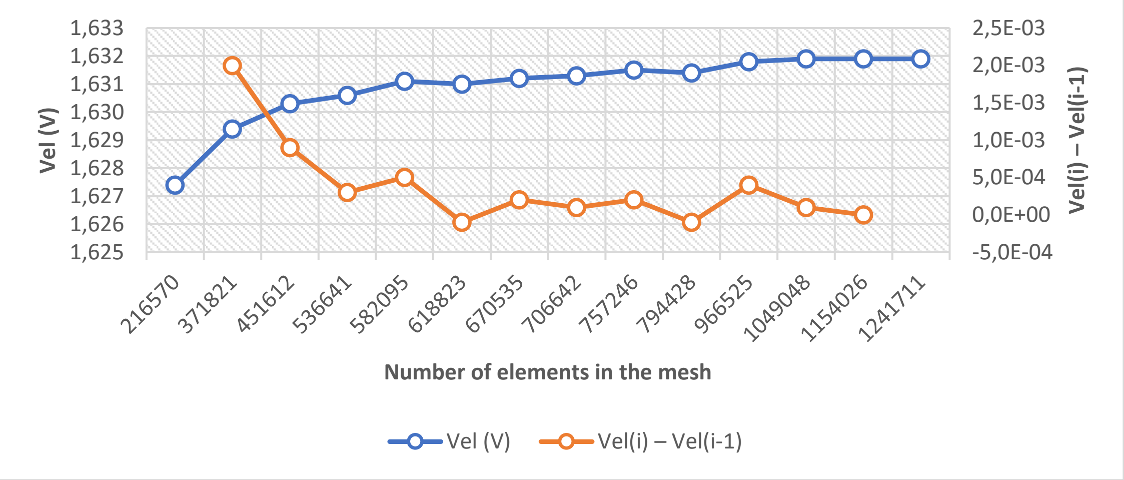

Figure 20- *Mesh analysis for hydrogen production simulation (V_{el} vs Number of elements in the mesh and $V_{el}(i) - V_{el}(i-1)$ vs Number of elements in the mesh).*

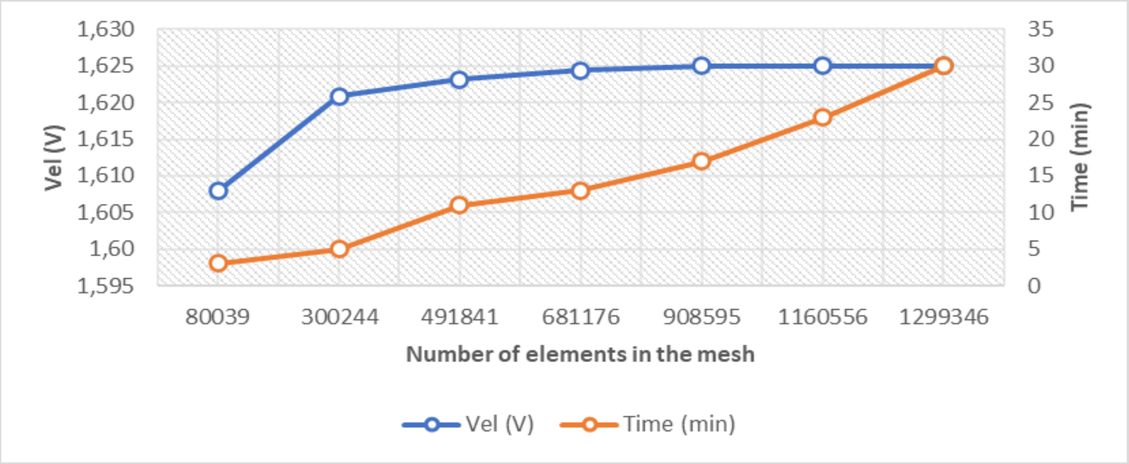

Figure 21- *Mesh analysis for syngas production simulation (V_{el} vs Number of elements in the mesh and Time vs number of elements in the mesh).*

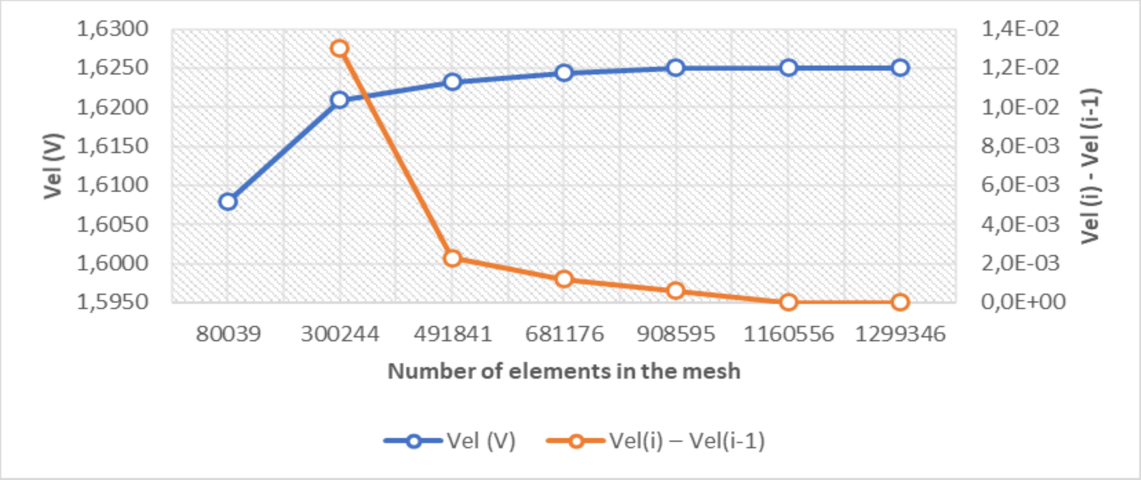

Figure 22- *Mesh analysis for syngas production simulation (V_{el} vs Number of elements in the mesh and $V_{el}(i) - V_{el}(i-1)$ vs Number of elements in the mesh).*

4. H_2 PRODUCTION SIMULATION

With the aim of assessing the potential of this integrated device and being able to provide general design guidelines, a parametric study was performed. The performance was assessed by the use of the solar-to-fuel efficiency (STF efficiency) and the molar rate of hydrogen production. The variables of interest we aim to modify in order to increase these parameters are: the current density, the solar cell temperature and the electrolyser temperature. A high operating current density leads to higher values of efficiency, however, too high values of the mean solar cell's temperature cause decreases in efficiency (800K being, approximately, the limit at which the photoabsorber starts failing at high temperatures, see *figure 15*). High temperature steam electrolysis typically operates at temperatures around 1023K-1223K [22], but we will not reach that maximum working temperature at which the electrolyte will start failing. Consequently, we simulated different parameters assessing its impact in the device's performance both from the energetic and production point of view. Variations of the integrated device's design, operating conditions and material properties were studied.

Increasing the solar concentration should lead to higher operating temperatures of the solar cell and electrolyte. However, due to the time limitations we faced during the course of the research, the focus of this study is investigating the different scenarios operating solely at a concentration of 50 suns. Meanwhile, it was discovered that increased T_{sc} led to a reduced maximum photovoltage and photocurrent the photoabsorber assembly is able to provide, and so the power density the assembly is able to deliver also decreases. On the other hand, an increased T_{el} caused the electrochemical potentials of the electrolyser to be reduced, and so led to reduced voltage requirements by the electrolyser, reducing its operating voltage and o increasing the rate of the product production.

An exhaustive study of each parameter was carried out, where we tried to improve the value of the parameter under investigation until we reached the limit where the device would no longer be able to keep functioning.

4.1 REFERENCE CASE

The values of the parameters used in the reference case are summarised in *table 3*.

Table 3- *Fixed parameters in the reference case for the hydrogen production simulation.*

PARAMETER	**REFERENCE CASE**
Inlet temperature of the species at the electrolyser (K)	423
Inlet velocity at the cathode (m/s)	2
Inlet velocity at the anode (m/s)	2
Anode inlet gas molar ratio O_2/N_2	0.21/0.79
Cathode inlet gas molar ratio H_2/H_2O	0.4/0.6
Cathode chamber height (mm)	1
Cathode thickness (μm)	100
Cathode porosity	0.48
Cathode tortuosity	5.4
Electrode thickness (μm)	10
Anode chamber height (mm)	2
Anode thickness (μm)	100
Anode porosity	0.48
Anode tortuosity	5.4
Chamber length (cm)	8
HTSC length (cm)	4
Electrolyser length (cm)	4
Flow direction	Parallel flow
Number of photoabsorbers in series	4
Solar concentration (suns)	50
Electrolyte type	CGO
Operating pressure (atm)	1

In the reference case scenario, the results exposed the non-isothermal characteristic of the device by showing how the temperature of the device increases from the photoabsorber assembly to the electrolyser components. This can be observed in *figure 23*, from which it is also useful to note how the temperature in all the electrolyser components is uniform, as the diagram shows them with the same colour. The voltage required by the electrolyser is shown to be practically constant along the anode electrode and solid electrolyte.

From the energetic point of view, the device is able to achieve a 7.77% solar-to-fuel efficiency at a solar concentration of 50 suns. Meanwhile, from the production point of view, a hydrogen molar flow rate of 16.38 mmol $m^{-2}s^{-1}$ is attained (*figure 24a*). The mean temperature of the solar cell obtained is 584.8K, whilst for the electrolyser a value of 664.6K is managed. With the electrolyser efficiency and the photoabsorber assembly efficiency being 69.87% and 11.05%, respectively, the efficiency of the whole integrated device gives a very low value (*figure 24b*). The low photoabsorber assembly efficiency can be explained by the limited current density produced by four HTSC connected in series (see *figure 17*). As the electrolyser performs better than the HTSC, the overall efficiency of the integrated device is constrained by the low performance of the HTSC.

The voltage required is considered to be relatively high, and can be attributed to the non-uniform temperature in the electrolyser (shown in *figure 23*). The inlet temperature is low, fixed at 423K, whilst it then increases. In the energy balance of the whole device, depicted in *figure 25a* we are shown how that 7.79% of the incoming solar radiation is reflected back into the atmosphere at the glass cover, P_{ref}; 41.66% and 23.55% are used for heating the fluids at the anode and the cathode, $Q_{\mathrm{s,a}}$ and $Q_{\mathrm{s,c}}$, respectively; 8.46% and 9.32% of the incoming energy is lost to the atmosphere due to convection and radiation, $Q_{\mathrm{c,g}}$ and $Q_{\mathrm{r,g}}$; a negligible amount of energy is lost by conduction at the cathode and anode inlet chambers, $Q_{\mathrm{cond,a+cond,c}}$; and 7.92% is kept in the produced fuel P_{fuel}. Considering the HTSC balance illustrated in *figure 25c*, we learn that 7.79% of the incoming solar radiation is reflected back into the atmosphere at the glass cover, P_{ref}; 22.17% of the heat energy is reflect at the top layer of the HTSC , Q_{ref}; 25.77% is not absorbed by the HTSC and is used to heat the electrolyser components, P_{nabs}; 32.52% is lost internally un the HTSC (due to self-heating); and the remaining 11.05% is transformed into useful power by the solar cell (account towards the solar cell's efficiency), P_{sc}.

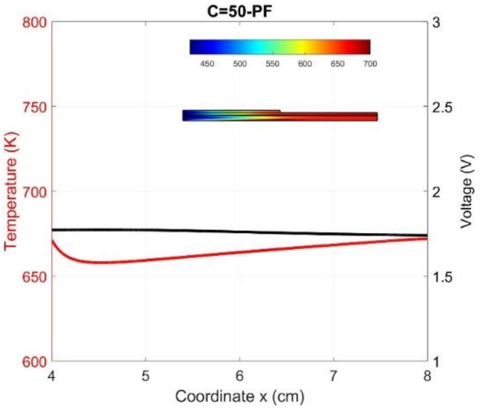

Figure 23- *Temperature and voltage evolution along the solid electrolyte and the anode electrode, respectively. The inset shows the temperature evolution of the whole device.*

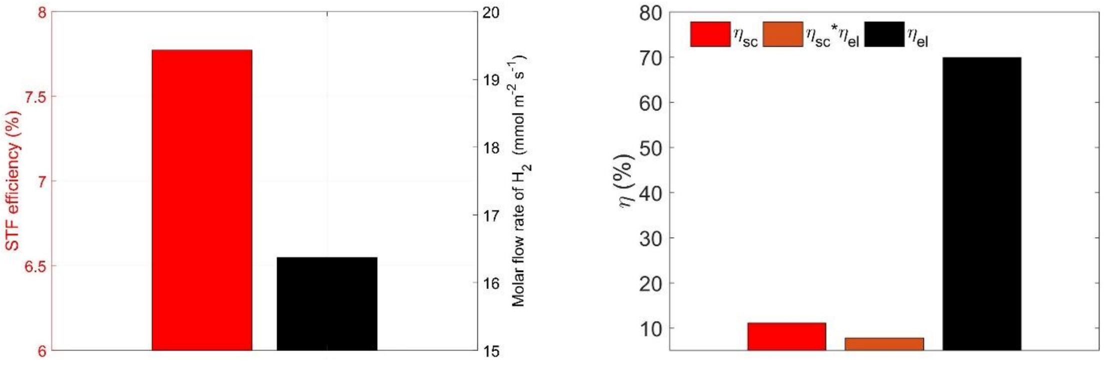

a)

b)

Figure 24- *Performance of the reference case:* ***a)*** *STF efficiency of device and molar flow rate of hydrogen,* ***b)*** *Solar cell efficiency, electrolyser efficiency and integrated device efficiency at 50 suns.*

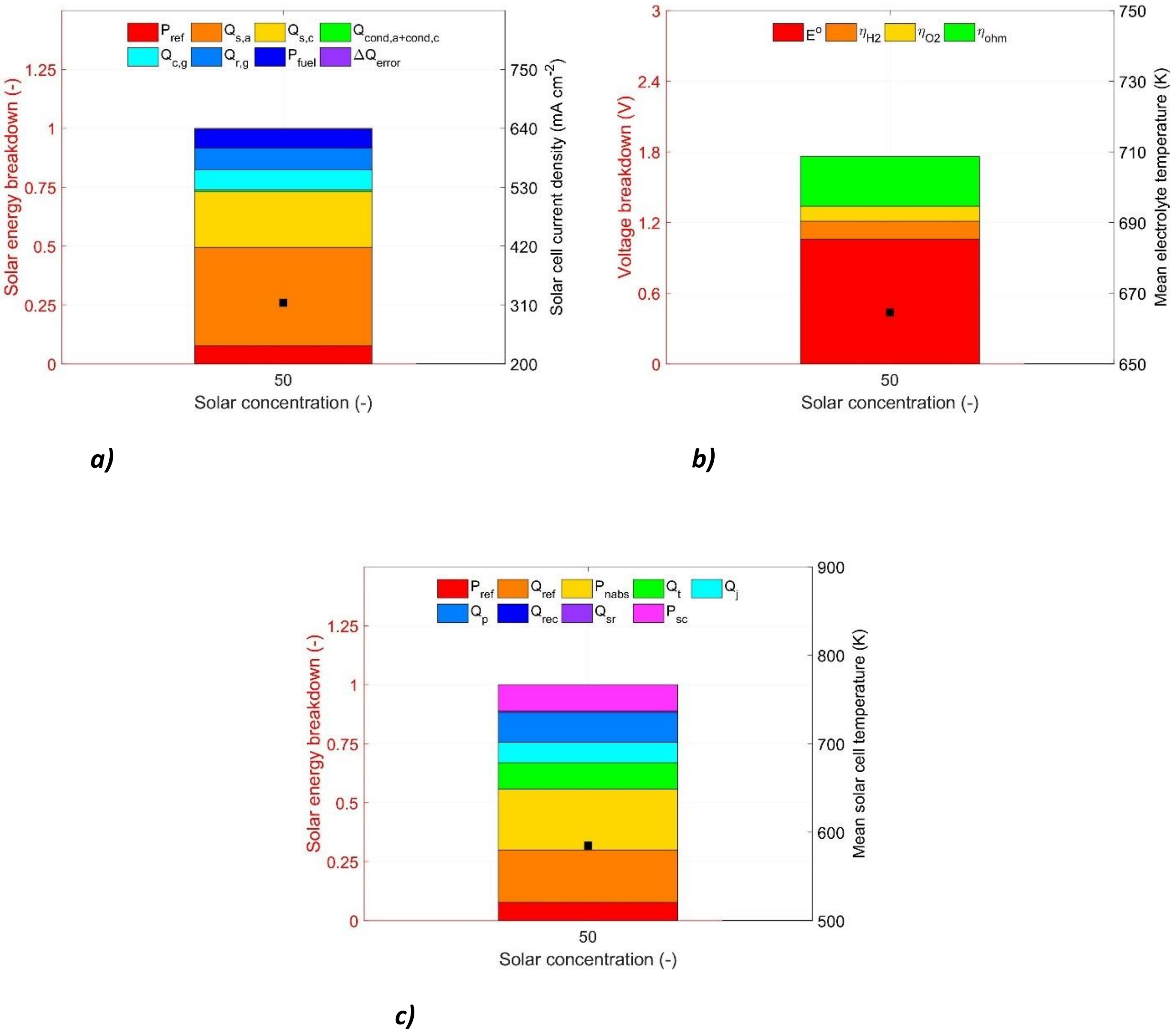

Figure 25- *Breakdown, in the reference case scenario, of* ***a)*** *the energy in the whole device, plus current density,* ***b)*** *the voltage in the electrolyser, plus* T_{el}*,* ***c)*** *the energy in the HTSC, plus* T_{sc}*.*

4.2 RESULTS OF THE PARAMETRIC ANALYSIS

The parameters studied in each different scenario during the hydrogen production parametric analysis are summarised in the following table.

Table 4- *Parameters used in each different case scenario for the hydrogen production simulation. The symbol '-' indicates no modification with respect to the reference case.*

SCENARIO	N_{sc}	$u_{c,0}$ **(m/s)**	**Electrolyte**	h_c **(mm)**	**Cathode electrode**	h_a **(mm)**	t_c **(µm)**
Reference case	4	2	CGO	1	Reference	2	100
1	3	-	-	-	-	-	-
2	-	1.5	-	-	-	-	-
3	-	1	-	-	-	-	-
4	-	0.5	-	-	-	-	-
5	-	0.1	-	-	-	-	-
6	-	-	Ideal	-	-	-	-
7	-	-	-	2	-	-	-
8	-	-	-	3	-	-	-
9	-	-	-	-	Ideal	-	-
10	-	-	-	-	-	1	-
11	-	-	-	-	-	-	500
Combination of parameters (1)	2	0.1	Ideal	1	Ideal	1	100
Combination of parameters (2)	2	0.5	Ideal	1	Ideal	1	100
Combination of parameters (3)	2	1	Ideal	1	Ideal	1	100

4.2.1 HEIGHT OF THE CATHODE CHAMBER

The cathode chamber height was varied from 1mm to 3mm in order to reduce the heat losses by convection and radiation from the quartz glass towards the exterior. Considering the heat energy in the solar cell, the closer the glass cover is positioned with respect to the HTSC, the hotter the glass will get, as the heat transferred by convection across the chamber from the photoabsorber to the quartz glass increases. Therefore, the temperature of the glass cover increases, resulting in an increase of the temperature difference between the glass and the external environment. This would cause higher heat losses by convection and radiation from the glass to the environment, worsening the performance of the device. Increasing the separation between the HTSC and the glass cover was expected to have an inverse effect. Furthermore, increasing the height of the cathode chamber results in an increase in the mass flow in the chamber, causing the sensible heat of the cathode to increase. This leads to a decrease in the temperature of the species in the chamber (the heat is shared between a larger number of molecules). This was expected to lead to an increase in the temperature difference between the top of the photoabsorber and the chamber, increasing the heat transferred by convection. The temperature of the solar cell, T_{sc}, would then experience a decrease, contributing to the improvement of the performance of the device.

The hydrogen molar rate decreased as the height increased from 1 to 2 mm (from 16.38 to 16.25 mmolm^{-2}s-1), and kept constant from 2 to 3mm (see *figure 27*). The same occurred with the STF efficiency (decreased from 7.77% to 7.714% and then stayed constant, *figure 26*) as the current density was also a parameter that experienced a decrease. This last parameter experienced a 1.43% decrease from h_c being 1mm to 2mm, and a 2.13% decrease from h_c being 1mm to 3mm. This current density variation can be observed in *figure 29a*, and causes a decrease in the Peltier source.

On the other hand, *figure 29c* shows the mean temperature of the solar cell T_sc decreased as expected, obtaining a maximum decrease of 7.35% with respect to the reference case when h_c=3mm. We also observed the desired effect of the decrease of the heat losses by convection and radiation, decreasing 27.24% and 35.17% with respect to the reference case, for the cases of h_c being 2mm and 3mm respectively (see *figure 29a*). From the same graph we can detect how the contribution of the sensible heat of the anode chamber $Q_\mathrm{s,a}$ slightly decreased, whilst the contribution of $Q_\mathrm{s,c}$ to the total heat sources increases considerably. The equation that describes the sensible heats at the electrode chambers is the following, with i being cathode or anode:

$$Q_{\mathrm{s},i} = mass\ flow * c_\mathrm{p} * (T_{\mathrm{outlet},i} - T_{\mathrm{inlet},i}) \qquad (17)$$

Taking *equation 17* into consideration, the sensible heat at the cathode chamber increases as the height of the chamber increases due to the fact that the mass flow of species in the chamber increases (a bigger mass is able to flow in the same time, due to the increased volume provided by the increased height of the chamber). This increase in sensible heat means more energy is needed to heat the species in the cathode, so the temperature of the fluid will be lower. This, in turn, causes a decrease in the temperature of the electrolyser’s components.

Figure 29c displays how the power produced by the solar cell (P_sc) experienced an increase (obtaining a maximum of 24.89% increase when working with the largest height), meaning that, as the current density gradually decreased its value (see *figure 29a*), the voltage produced by the solar cell must have in turn increased. On the other hand, the electrolyser’s operating temperature T_el experienced an 8.49% and 12.20% decrease with respect to the reference case when working with 2mm and 3mm heights respectively (see *figure 29b*). This led to a considerable increment in the overpotentials at the cathode and anode electrodes, η_{H_2} and η_{O_2} and a more meaningful one in the voltage lost in the electrolyte, η_ohm (28.12%, 19.86% and 93.08% increase, respectively, with respect to the reference case when working with a 3mm high cathode chamber). As a consequence, the electrolyser’s voltage requirement increased from 1.76V (when h_c=1mm) to 2.06V (when h_c=2mm) to 2.25V (when h_c=3mm). We can also perceive this from the IV curves shown in *figure 28,* as the voltage increases with the height.

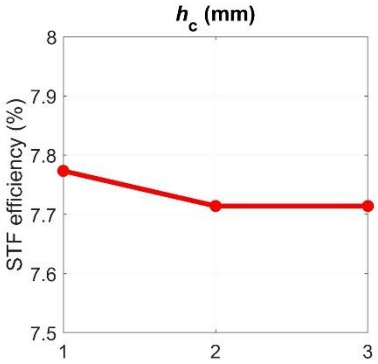

Figure 26- *STF efficiencies for the different heights of the cathode chamber.*

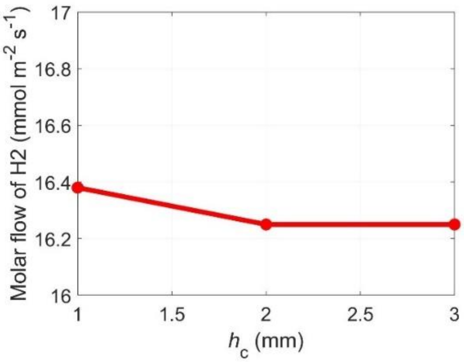

Figure 27- *Molar flow rate of hydrogen produced vs height of the cathode chamber.*

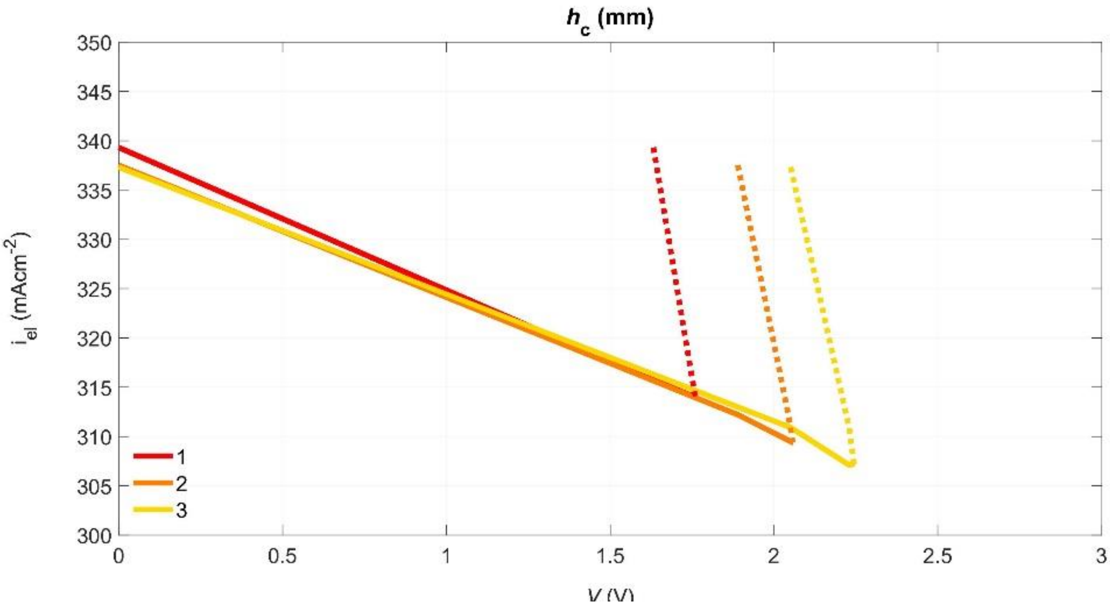

__Figure 28__- IV curves for the different heights of the cathode chamber.

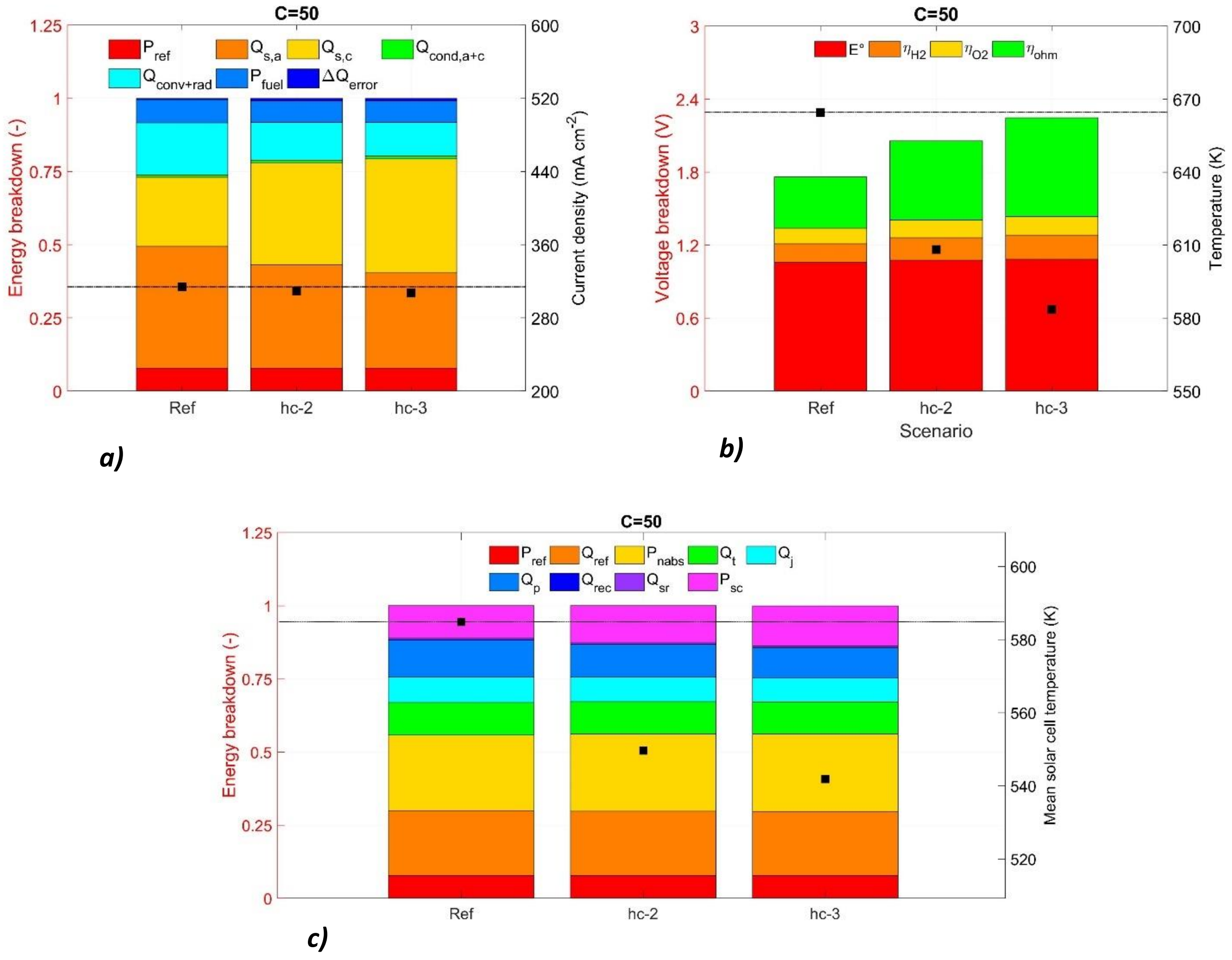

__Figure 29__- Breakdown, varying the height of the cathode chamber, of __a)__ the energy in the whole device, plus current density, __b)__ the voltage in the electrolyser, plus T_{el}, __c)__ the energy in the HTSC, plus T_{sc}.

4.2.2 HEIGHT OF THE ANODE CHAMBER

In order to rise the temperature of the electrolyser components and further reduce the voltage required by the electrolyser, we decreased the height of the anode chamber from 2mm to 1mm. Heat source P_{nabs} (the non-absorbed fraction of the solar energy by the photoabsorber which heats directly the internal elements of the device by convection) was expected to cause a greater increase of the temperature at the bottom layer of the device, which will in turn cause the temperature of the electrolyser components to increase.

It was proved that reducing the anode chamber height from 2mm to 1mm considerably increased the mean temperature of the electrolyser T_{el}, from 664.6K to 757.2K. This caused the overpotentials at both electrodes and the voltage lost in the electrolyser ($\eta_{\mathrm{H_2}}, \eta_{\mathrm{O_2}}$ and η_{ohm}) to decrease (43.30%, 28.13% and 49.17% decrease with respect to the reference case, respectively), leading to a noticeable decrease in the required voltage, from 1.76V to 1.42V. This made the height of the anode chamber the parameter which managed the biggest decrease in V_{el}. All of these effects can be visually seen in *figure 32* and *33b*. This increase in the temperature of the electrolyser components was due to the fact that, as the height of the chamber decreased, the mass flow through it decreased too. Taking *equation 17* into consideration, this causes a decrease in the sensible heat of the anode chamber, $Q_{\mathrm{s,a}}$ (see *figure 33a*), which means that less energy is needed in order to heat the fluid in the chamber. In turn, this causes the temperature of the species in the chamber to increase, and therefore the temperature of the electrolyser to increase, as heat is transferred from the chamber to the electrode.

The mean temperature of the solar cell T_{sc} experiences an increase of 6.29% with respect to the reference case, provoking the power density the photoabsorber assembly (P_{sc} in *figure 33c*) to decrease. This means even though the required voltage decreases (*figure 33b*), as the provided one decreases too, the molar flow of hydrogen gas is only able to produce a practically insignificant increase (from 16.38 to 16.75 mmolm^{-2}s^{-1}, *figure 31*). Due to the increase in the HTSC temperature, the STF efficiency slightly decreases from 2mm to 1mm height of the anode chamber, from 7.77% to 7.71% respectively (see *figure 30*).

The energy breakdown of the balance in the HTSC depicted in *figure 33c* shows slight augment in the current density, from 313.9 mAcm^{-2} to 320.6 mAcm^{-2} (due to the increase in solar cell temperature). Furthermore, it shows how the contribution of each volumetric heat source remains practically unchanged, with the exception of P_{nabs} and P_{sc}, which slightly decreased due to the reasons mentioned.

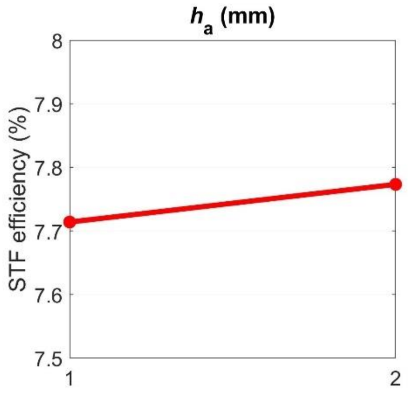

Figure 30- *STF efficiencies for the different heights of the anode chamber.*

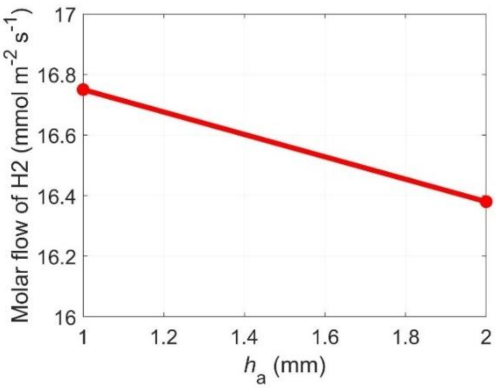

Figure 31- *Molar flow rate of hydrogen produced vs height of the anode chamber.*

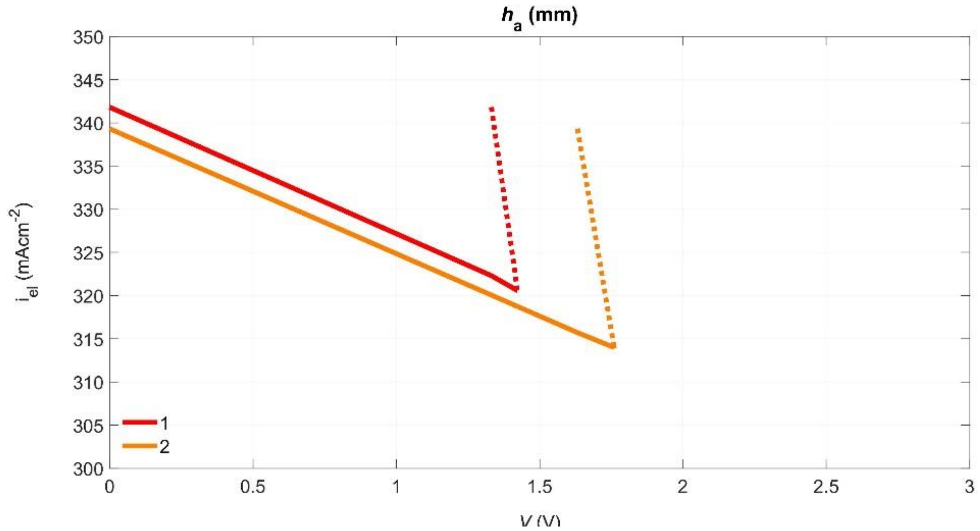

Figure 32- IV curves for the different heights of the anode chamber.

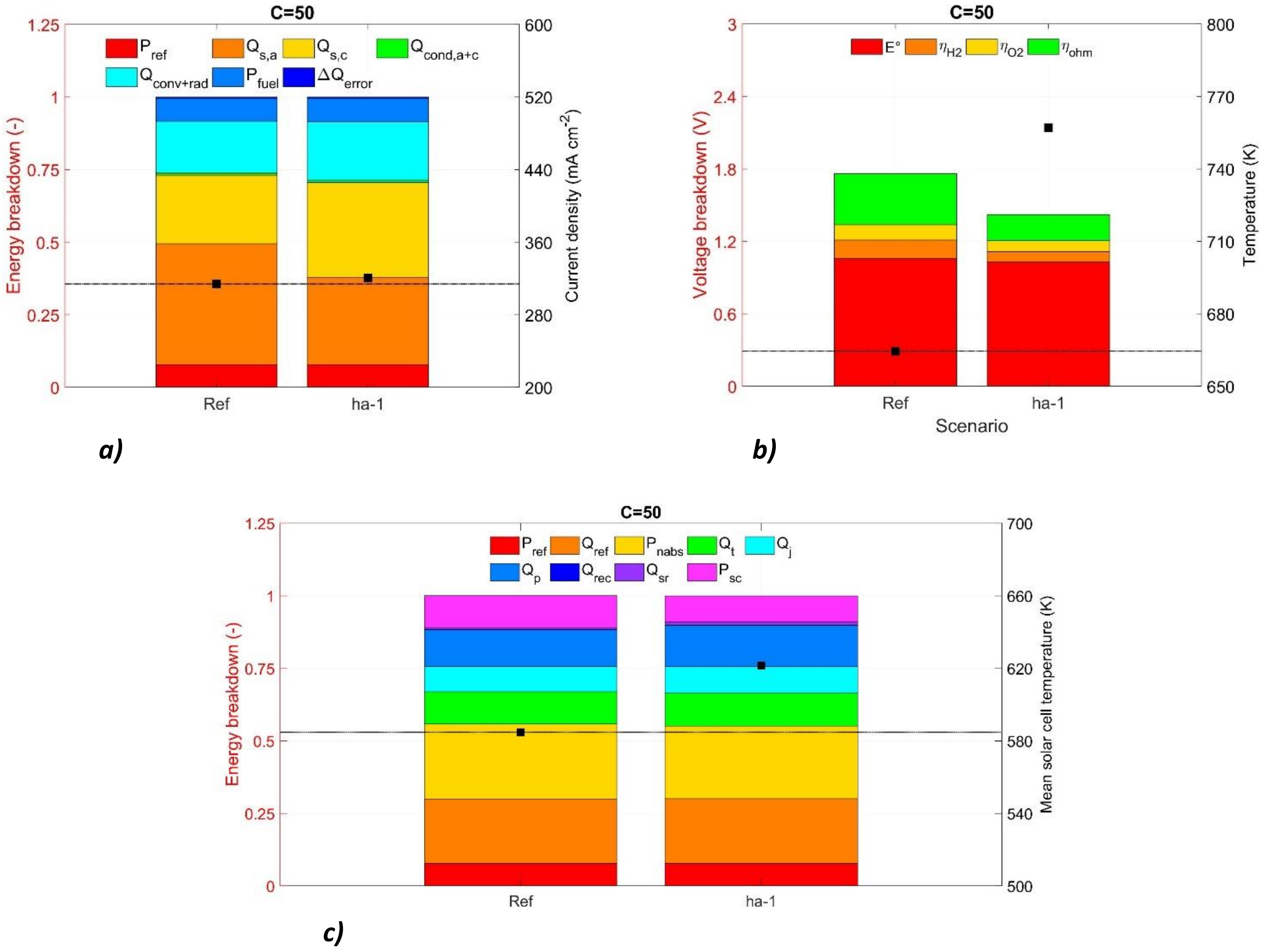

Figure 33- *Breakdown, varying the height of the anode chamber, of* ***a)*** *the energy in the whole device, plus current density,* ***b)*** *the voltage in the electrolyser, plus T_{el},* ***c)*** *the energy in the HTSC, plus T_{sc}.*

4.2.3 NUMBER OF SOLAR CELLS

In order to increase the current density provided to the electrolyser and therefore increase the molar flow rate of hydrogen and the STF efficiency, the number of solar cells was reduced to three. As a side effect, the maximum voltage at which they can work, would decrease (see *figure 17*). In addition, this factor is of interest as it contributes to the cost and scalability of the device.

The results showed that operating with three photoabsorbers in series was able to notoriously increase the efficiency from 7.7% up to a value of 9.97% (*figure 34*). Similarly, the hydrogen molar flow rate resulted 28.2% higher with respect to the reference case, increasing up to 21 mmolm^{-2}s^{-1} (*figure 35*). The obtained desired effect can be seen in *figure 37a*, which shows the increase in current density produced. However, this leads to a higher working voltage of the electrolyser. This can be seen in *figures 36* and *37b*. Results also showed that both the mean operating temperature of the electrolyser and the solar cell were slightly lower in comparison with the reference case (see *figures 37b and 37c*).

The 2.55% decrease in the T_{sc} with respect to the reference case was explain due to the fact that the internal heat sources of the solar cell were lower when reducing the number of photoabsorber assemblies from four to three. That is concluded from the *figure 37c*, as the sum of Q_{tot} and Q_{b} (joint contribution of Q_{p}, Q_{j}, Q_{t}, Q_{rec}, Q_{sc}) was smaller when only three solar cells operated in series. Having less internal heating leads to lower temperatures of the solar cell, as more energy is used to create power (P_{sc} can be seen to increase from four to three solar cells). In other words, the absorbed energy is used to produce electrical power, instead of being transformed into heat (which would in turn cause an increase in T_{sc}).

On the other hand, the 1.26% decrease in the electrolyser temperature T_{el} (shown in *figure 37b*) with respect to the reference case can be explained by observing *figures 38a and 38b*. As we can see, the heat sources related to the solar cell (H_{s1}, P_{nabs} and H_{s3}) are much higher than the ones related to the electrolyser ($Q_{\mathrm{a+c}}$ and $Q_{\mathrm{ohm,e}}$), meaning the solar cell has a bigger contribution to the overall heating of the device than the electrolyser (94.1% and 5.9% respectively), and thus to the temperature of the device. It is true that the temperature of the electrolyser is not influenced directly by the heat sources H_{s1} and H_{s3}, however, the contribution of P_{nabs} is still much larger than that of $Q_{\mathrm{a+c}}$ and $Q_{\mathrm{ohm,e}}$. As a consequence, the temperature of the electrolyte is mainly influenced by the solar cell's heat sources.

From *figure 37b* we can observe the voltage lost in the electrolyte η_{ohm} significantly increases when having three photoabsorbers operating, it does so 22.3% with respect to the reference case. The contribution of this increase plus the 28.51% increase in current density (seen in *figure 37c)* cause the ohmic heat source ($Q_{\mathrm{ohm,e}}$), which represent the energy loss due to internal resistances in the electrolyser caused by the resistance for ions to move through the electrolyte (calculated as current*voltage) to increase from four to three solar cells (see *figures 38a and 38b*). However, even with this situation, T_{el} decreases. From this we extract that the ohmic heat sources don't control the temperature, T_{el}, as their contribution to the overall heat sources is practically negligible over the others.

For the case of three solar cells, the power vs solar cell voltage graph (*figure 39a*) has the shown shape, as, once the operating point is reached, it stops further calculating values. From this graph we know the device is working before its maximum power point, but relatively close to it. We can also extract this same conclusion from *figure 40*, as T_{sc} experiences a continuous decrease until it reaches the operating point. However, if the maximum power point was exceeded, this graph would have shown T_{sc} reaching a minimum value and then increasing again. The operating point being closer to the maximum power point explains why the heat losses in the photoabsorber were smaller than in the reference case. We then decided to further decrease the number of photoabsorbers operating in series from three to two, aiming to further increase the efficiency and production of the device. As T_{sc} in the case of three photoabsorbers was still far from its limit it was thought the functioning of the device was attainable, however, the results showed the operating point was not been able to be reached. This probably occurred due to overheating of the solar cell which substantially reduced the maximum photovoltage. From *figure 39b* we can see how the operating point was not reached.

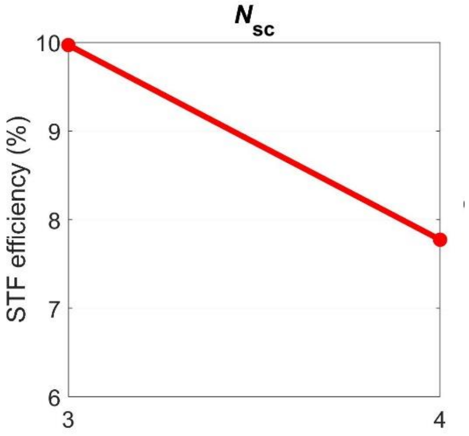

Figure 34- *STF efficiencies varying the number of photoabsorbers.*

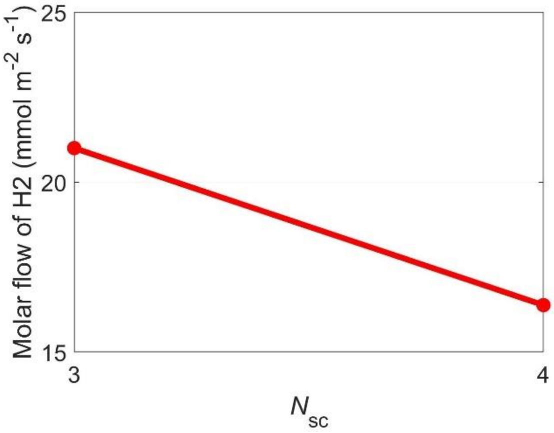

Figure 35- *Molar flow rate of hydrogen produced vs the number of operating photoabsorbers.*

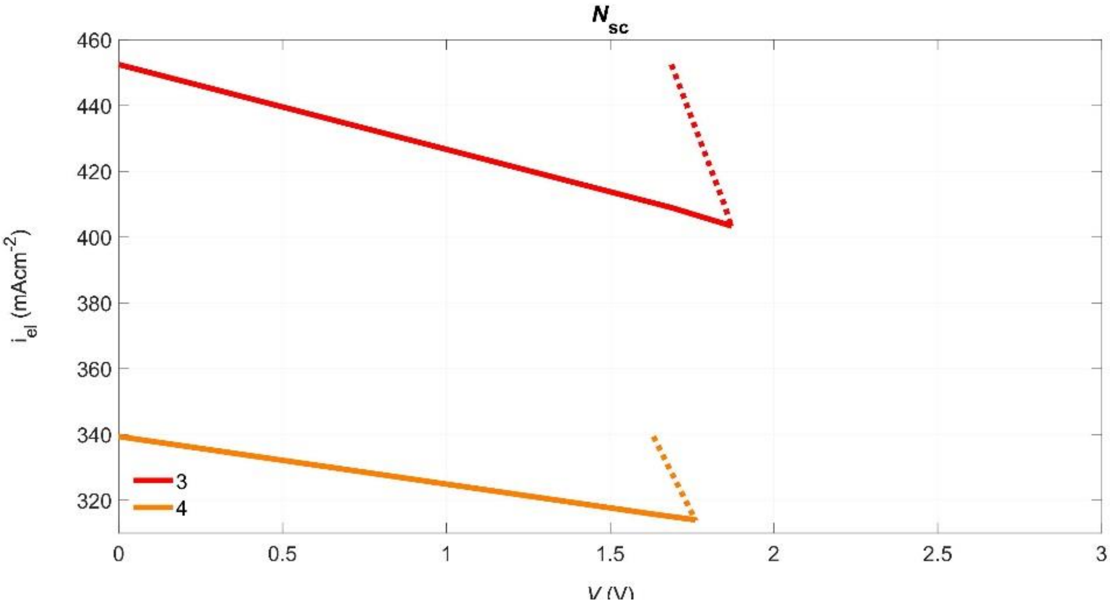

Figure 36- *IV curves for the different number of operating photoabsorbers.*

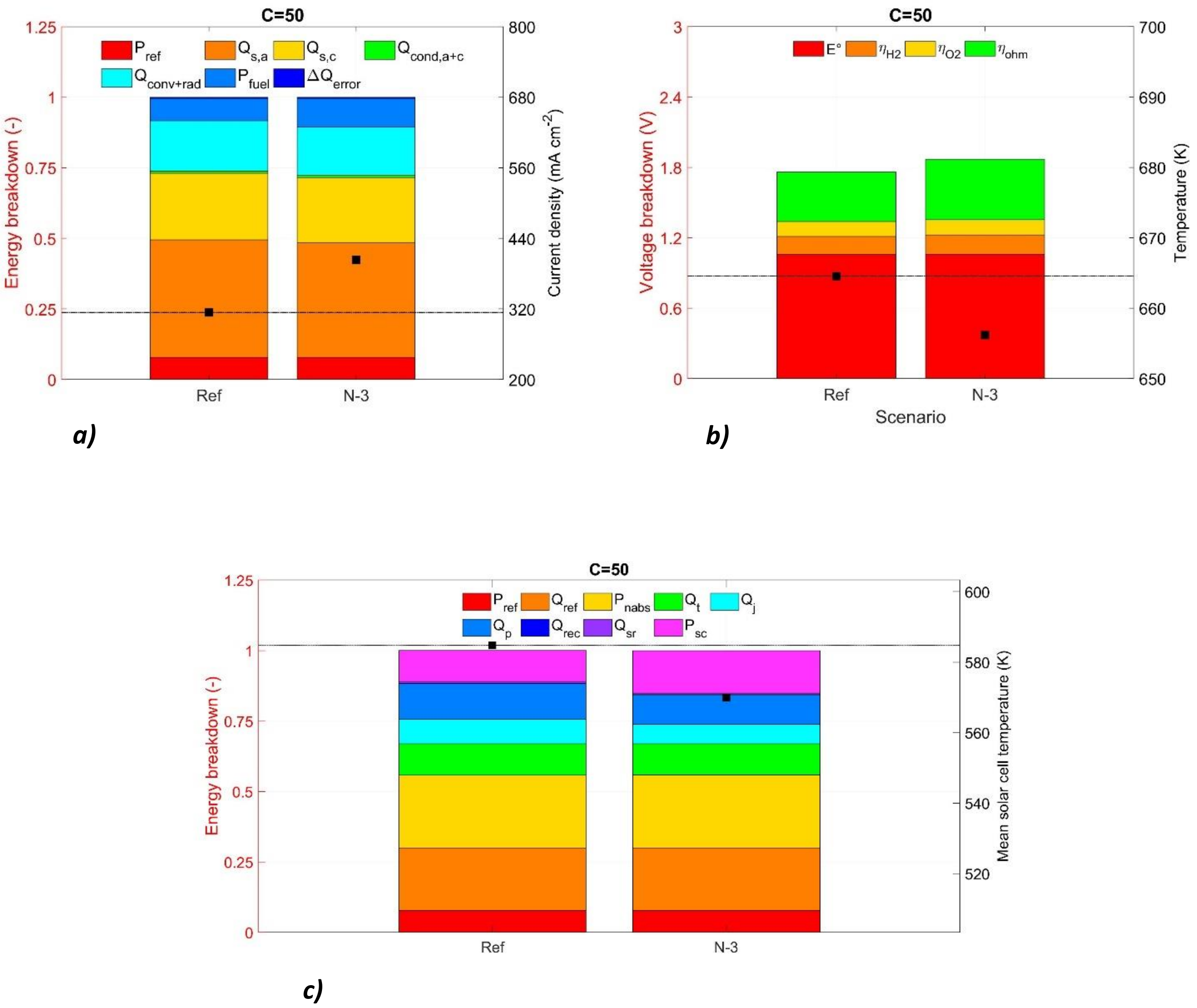

Figure 37- *Breakdown, varying N_{sc}, of* ***a)*** *the energy in the whole device, plus current density,* ***b)*** *the voltage in the electrolyser, plus T_{el},* ***c)*** *the energy in the HTSC, plus T_{sc}.*

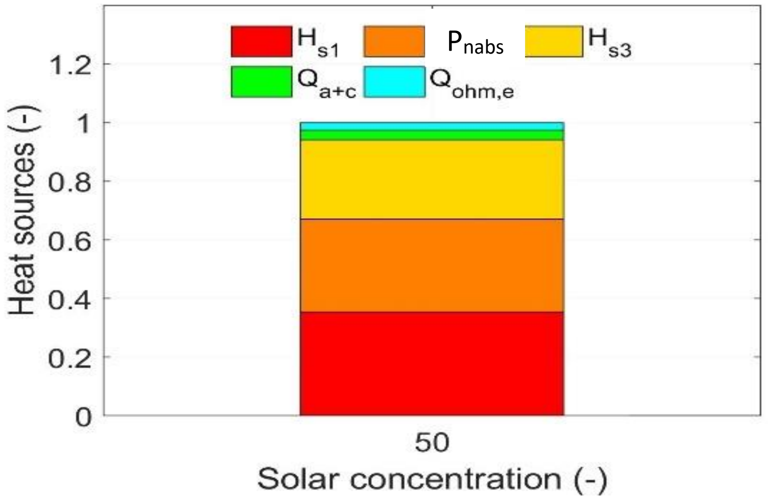

Figure 38a) *Heat sources in the case of 3 solar cells.*

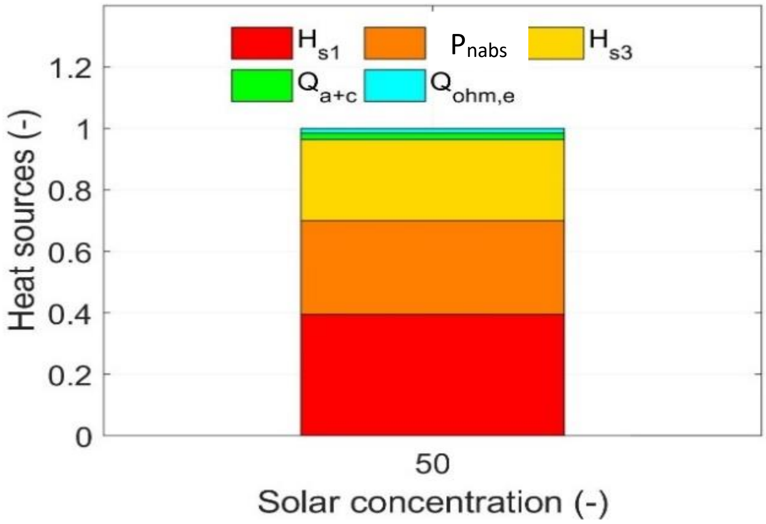

Figure 38b) *Heat sources in the reference case, during the hydrogen production parametric analysis.*

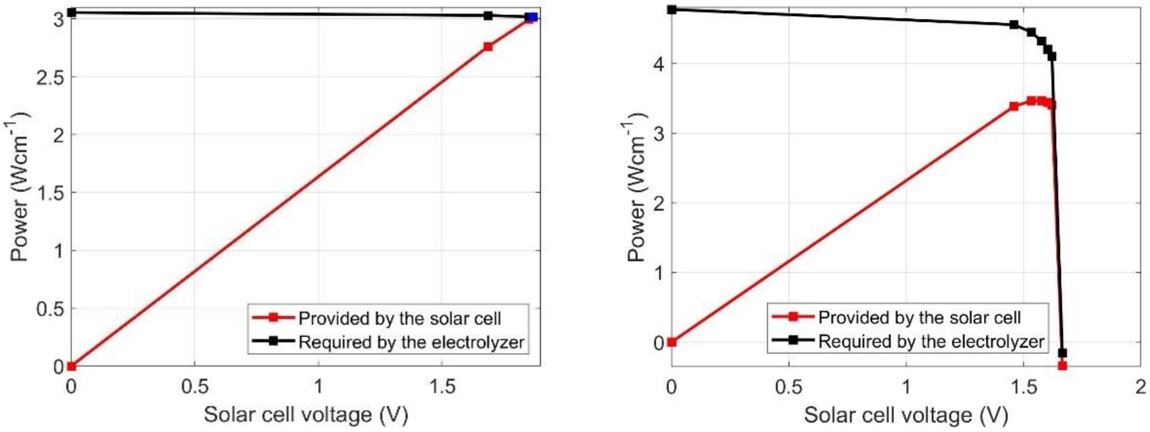

a) ***b)***

Figure 39- *Power vs Voltage graph for the case of* ***a)*** *3 photoabsorbers,* ***b)*** *2 photoabsorbers, during the hydrogen production parametric analysis.*

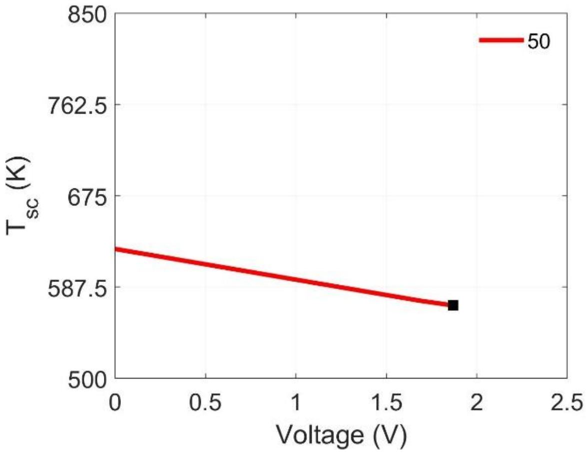

Figure 40- *T_{sc} vs Voltage in the case of 3 photoabsorbers during the hydrogen production parametric analysis.*

4.2.4 CATHODE ELECTRODE THICKNESS

In order to verify the molar flow rate of hydrogen fuel produced was not limited by the available surface area of the porous cathode electrode where the reaction takes place, its thickness was increased.

The obtained results showed that, in fact, the amount of hydrogen produced remained the same when using a thicker electrode, 16.38 mmolm^{-2}s^{-1} (*figure 42*). Similarly, the STF efficiency maintained its value of 7.77%, both with a cathode of 100µm and 500µm thickness (*figure 41*). This shows the electrode surface area was not a limiting factor in the amount of H_2 produced.

The variation in this parameter did not have an effect either on the operating temperature of the electrolyser and of the photoabsorber assembly, as they only experienced a 0.17% and 0.15% decrease, respectively, with respect to the reference case (*figures 44b* and *44c* respectively). Likewise, the calculated current density provided by the HTSC with a cathode thickness of 100µm and 500µm were the same, 313.9 mAcm^{-2} (*figure 44a*).

The energy breakdown between the different heat sources in the whole device (*figure 44a*) remains unaffected, whilst in the energy breakdown between the heat sources in the solar cell (*figure 44c*) we see that the contribution of the heat losses due to the Peltier effect Q_{p} slightly decrease from 12.57% to 11.32%, whilst the radiative heat source contribution, Q_{sr}, increases from 0.65% to 1.89%.

The voltage breakdown comparison (*figure 44b*) showed us how the overpotential at the anode $\eta_{\mathrm{O_2}}$ remains constant whilst the one at the cathode $\eta_{\mathrm{H_2}}$ decreases notoriously due the increased volume of the electrode, however the voltage lost in the electrolyte η_{ohm} increases, having the overall effect of increasing the voltage required V_{el}, from 1.76V to 1.77V. As the cathode electrode is a mixture of solid electrolyte and a catalyst, increasing the thickness of the cathode causes an increase in the ionic resistance, η_{ohm}. We can see how the IV curves of these two scenarios (*figure 43*) overlap, as the current density remains the same and the change experienced by the voltage is negligible.

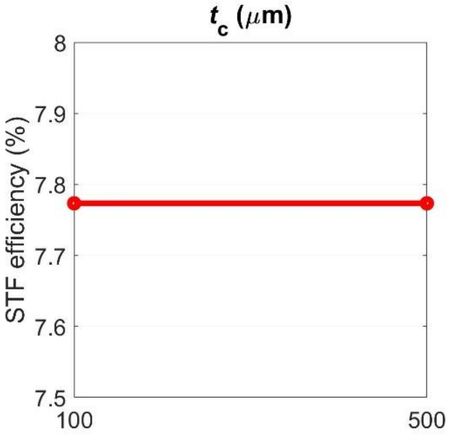

Figure 41- *STF efficiencies varying the cathode electrode thickness.*

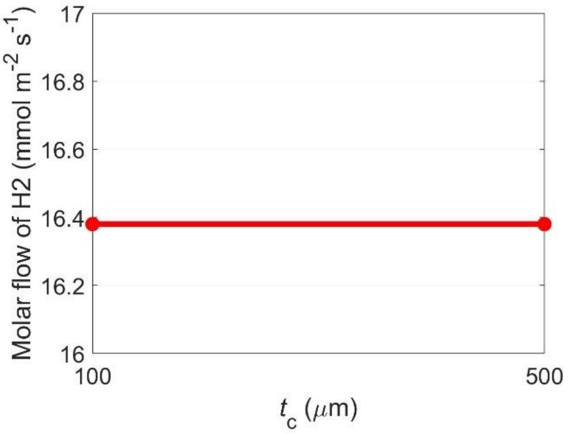

Figure 42- *Molar flow rate of hydrogen produced vs the thickness of the cathode electrode.*

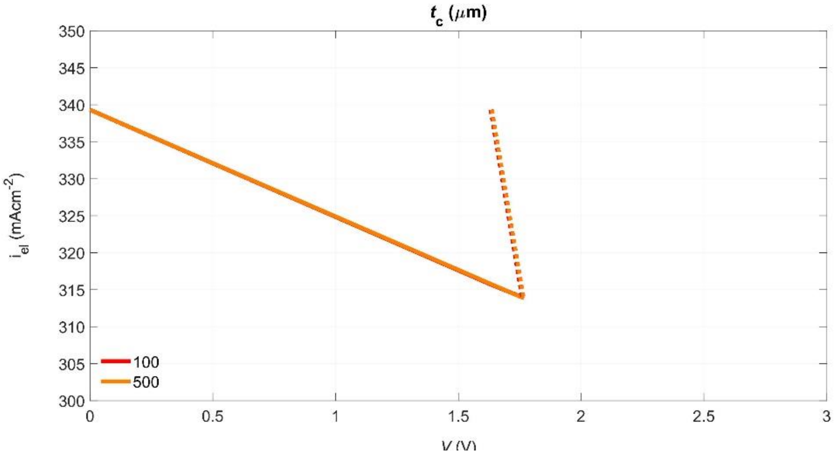

Figure 43- *IV curves for the different cathode electrode thicknesses.*

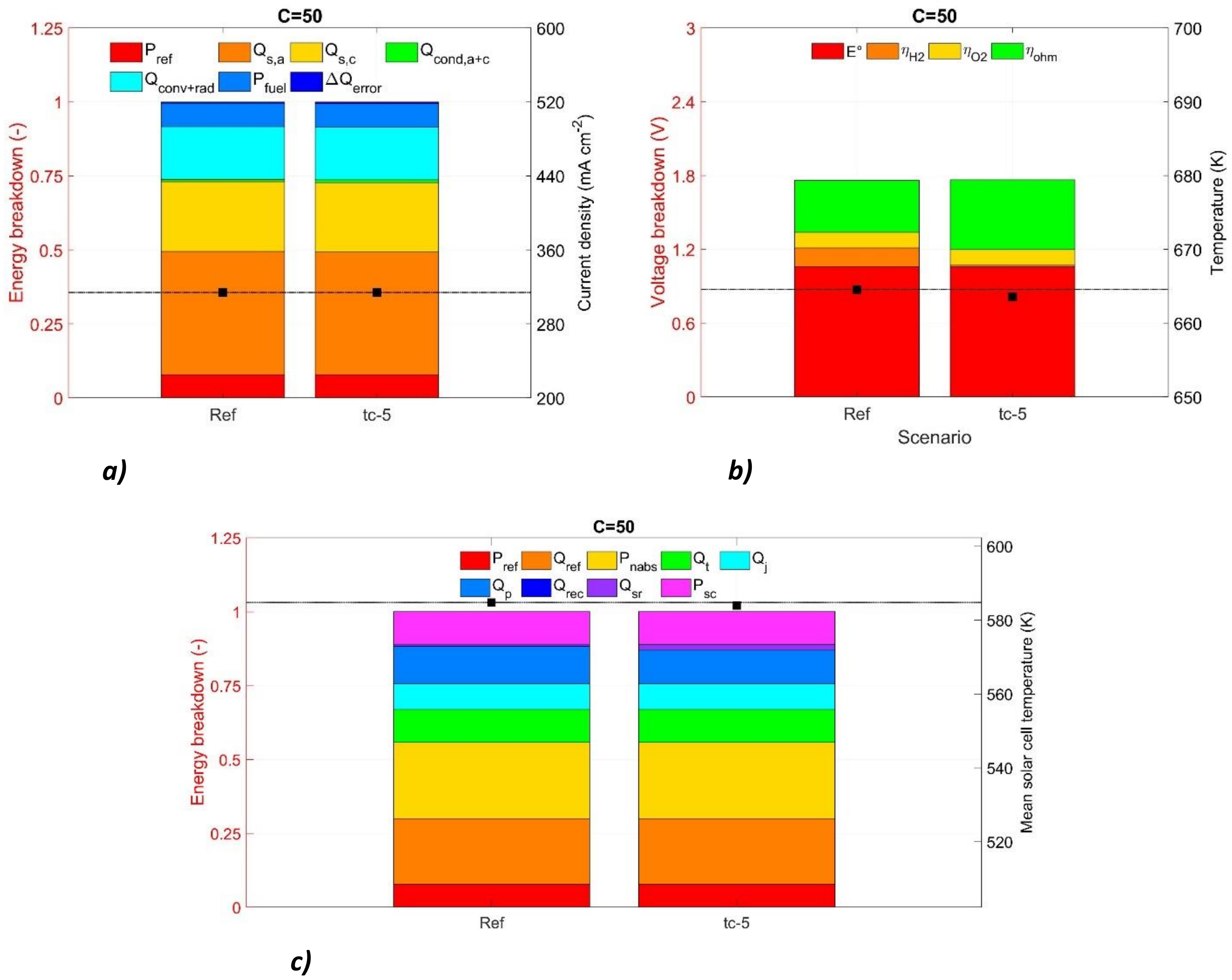

a) ***b)***

c)

Figure 44- *Breakdown, varying the cathode thickness, of* ***a)*** *the energy in the whole device, plus current density,* ***b)*** *the voltage in the electrolyser, plus* T_{el}, ***c)*** *the energy in the HTSC, plus* T_{sc}.

4.2.5 INLET VELOCITY AT THE CATHODE CHAMBER

The inlet velocity of the reactants in the cathode was reduced from 2m/s to 1.5m/s, 1m/s 0.5m/s and finally to 0.1m/s. Lower velocities were expected to increase the heat transfer in the chamber, and so permit the temperature of the electrolyser components to rise. Reducing the velocity at the inlet of the chamber reduces the mass flow in it, this means the fluid in the chamber should reach higher temperatures as it requires less energy to do so ($Q_{\mathrm{s,c}}$ decreases as the mass flow decreases). With this we aimed at positively increasing the temperature of the electrolyser components (as a higher temperature in the cathode chamber would lead to an increase in the temperature of the cathode electrode), impacting the electrolyser's voltage requirements and thus the hydrogen production and device efficiency.

The results confirmed our beliefs, as the mean temperature of the electrolyser T_{el} increased each time the velocity was reduced, obtaining a maximum temperature of 791K at 0.1m/s, this can be visually seen in *figure 47b*. As a consequence, the STF efficiency experienced a positive effect, increasing as the temperature of the electrolyser increased. It was calculated that reducing the inlet velocity to 1.5m/s led to a 0.77% increase in efficiency with respect to the reference case, whilst reducing it to 0.1m/s caused a 2.75% increase (*figure 45*). However, as observed, the rise in efficiency occurred in a much more gradual manner in comparison with the notorious increase in efficiency caused by the reduction of the number of operating photoabsorbers. The molar hydrogen flow experienced a slight increase, 0.73% from 2 to 1.5m/s, 2.26% from 2 to 1m/s, 3.05% from 2 to 0.5m/s and 2.74% from 2 to 0.1m/s. These are considered, however, practically negligible increases.

On the negative side, as the decrease in speed led to an increase in the temperature of the species in the chamber, not only T_{el} increased, but so did T_{sc}. This is proved in *figure 47c*, T_{sc} attaining a maximum at the 0.1m/s scenario, with a 18.8% increase with respect to the reference case. The same figure represents the energy breakdown in the HTSC, and illustrates how the proportion of contribution of each heat source to the assembly remained fairly constant from one scenario to the next. The voltage requirements by the electrolyser also experienced a positive impact, decreasing as the velocity decreased. This is due to the reduction in η_{ohm}, caused by the decrease in T_{el}. This can be seen in *figure 47b*, where best value was found at 0.1m/s, obtaining an 11.08% decrease in voltage with respect to the reference case. Meanwhile, the energy balance of the whole system, seen in *figure 47a*, demonstrates how, as the velocity decreased, the sensible heat at the cathode ($Q_{\mathrm{s,c}}$) considerably decreased whilst the one at the anode ($Q_{\mathrm{s,a}}$) and the convective and radiative heat losses ($Q_{\mathrm{conv+rad}}$) increased. This last increase can be easily explained. As the fluid in the cathode is at a higher temperature than the glass cover, heat energy is transferred from the fluid to the glass. Therefore, the glass would achieve a higher thermal difference with the external environment, which leads to higher convective and radiative losses. Considering *equation 17*, the decrease in the contribution of $Q_{\mathrm{s,c}}$ is therefore due to the fact that lower mass flow rate is coming into the cathode chamber. As the temperature of the fluid in the cathode, and therefore the temperature of the electrolyser components increases, heat energy will be transferred to the fluid in the anode chamber. As the inlet temperature is fixed, increasing the temperature in the chamber leads to an increase in the difference of temperatures between the inlet and outlet of the chamber, thus increasing the sensible heat at the anode, $Q_{\mathrm{s,a}}$ (see *equation 17*).

When the last simulation was carried out, with velocity equal to 0.1m/s, the results showed how the STF efficiency, the current density produced by the solar cell and the molar rate of hydrogen produced suffered a slight decrease with respect to the previous scenario of 0.5m/s (0.3%, 0.09%

and 0.3% decrease respectively). This can be seen in *figures 45, 47a* and *46* respectively. These results were unexpected, as both T_{el} and T_{sc} further increased under these conditions. The voltage of the electrolyser decreased; however, it is probably the case that the decrease in the voltage of the photoabsorber assembly was higher.

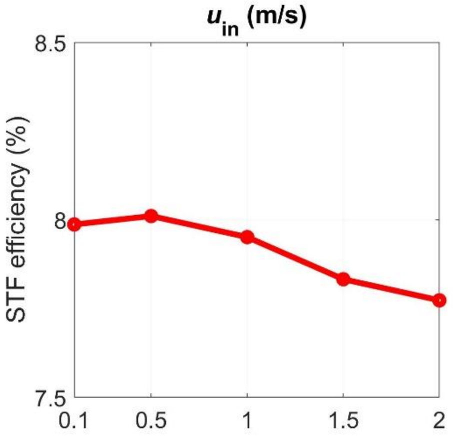

Figure 45- *STF efficiencies varying the velocity at the inlet of the cathode chamber.*

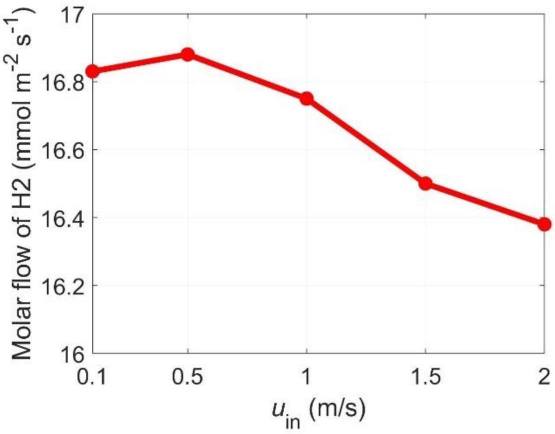

Figure 46- *Molar flow rate of hydrogen produced vs the different inlet velocities at the cathode chamber.*

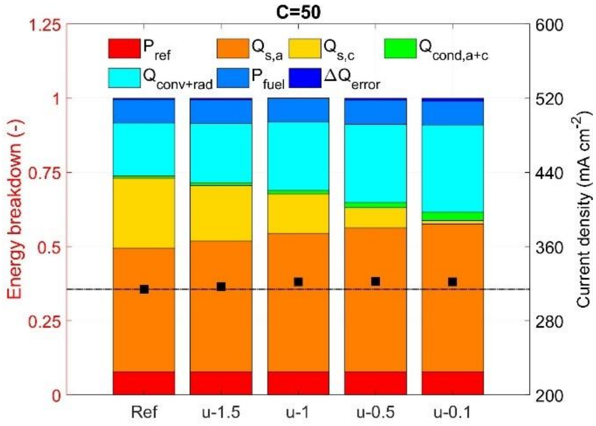

Figure 47a) *Breakdown, varying the inlet velocity at the cathode chamber of the energy in the whole device, plus current density.*

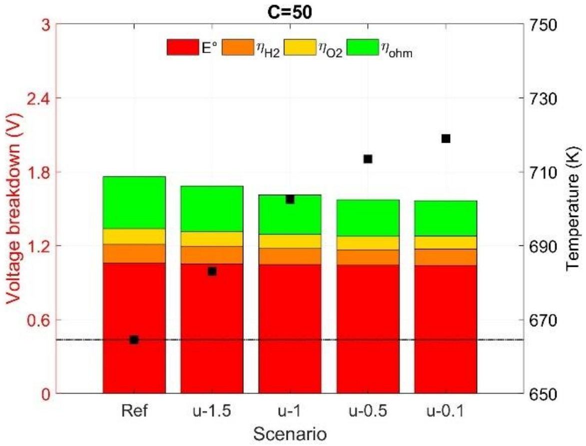

Figure 47b) *Breakdown, varying the inlet velocity at the cathode chamber of the voltage in the electrolyser, plus* T_{el}.

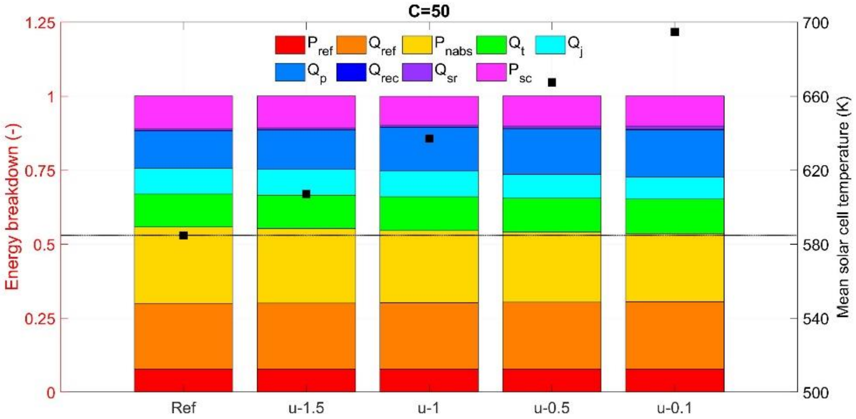

Figure 47c) *Breakdown, varying the inlet velocity at the cathode chamber, of the energy in the HTSC, plus T_{sc}.*

4.2.6 ELECTROLYTE TYPE

We tried to reduce the required voltage by the electrolyser by controlling the electrolyte type. The high voltage loss in the electrolyte in the reference scenario (η_{ohm}) was addressed by replacing the CGO solid electrolyte used by an ideal solid electrolyte with high ionic conductivity. For this purpose, we used the ideal electrolyte "ie". We expected the efficiency and the hydrogen fuel production to increase, as the ions should face lower resistance to their flow across the electrolyte.

The simulation showed that using an ideal electrolyte allowed the STF efficiency and the molar flow rate of hydrogen to slightly increase, improving the performance of the device. The STF efficiency increased from 7.77% in the reference case to 7.89% when using an ideal electrolyte (*figure 48*). Parallelly, the molar flow rate of hydrogen increased in 0.25 mmolm^{-2}s^{-1} (*figure 49*). The increase in the efficiency is due to the slight increase in the operating current density (1.47% increase with respect to the reference case, see *figure 51a*).

Figure 51b shows both, how T_{el} decreases with respect to the reference case (from 664.6K to 663.6K) and how $\eta_{\mathrm{H_2}}$ and $\eta_{\mathrm{O_2}}$increase from the reference case to the current situation (51.75% and 43.55% increase with respect to the reference case, respectively). It is also revealed how η_{ohm} experiences an important decrease, from a value of 0.42V in the reference case to a value of 0.012V, caused by the increased ion conductivity (less voltage is lost in the electrolyte, meaning less voltage is needed to power the electrochemical reaction taking place in the electrolyser). The reduction in η_{ohm} causes, in turn, a decrease of the ohmic losses ($Q_{\mathrm{ohm,e}}$) by reducing the resistance for ions to move through the electrolyte, and thus to the decrease of its contribution to the volumetric heat sources in the device, from 1.65% contribution in the reference case to 0% contribution in the present scenario (this can be observed in *figures 52a* and *52b*). Although the contribution of $Q_{\mathrm{ohm,e}}$ to the overall heat sources in the device is small, the increase in the internal heat sources of the HTSC (joint contribution of Q_{p}, Q_{j}, Q_{t}, Q_{rec}, Q_{sc}, seen in *figure 51c*) has an even smaller impact, resulting in the overall effect of slightly decreasing T_{el}. If less heat is released from the cathode and anode, it means more heat must have been absorbed, meaning the heat sink in the cathode must have increased. Due to this increase, less energy is used to increase the temperature of the electrolyser. In other words, and in a more summarised manner, as the voltage required decreases, the operating point gets closer to the maximum power point of the HTSC, which means the heat sources decrease. This causes the temperature of the electrolyser to decrease.

As just mentioned, the internal heat sources in the HTSC experience a slight increase when operating with an ideal electrolyte (*figure 51c*), being the reason of the increase in T_{sc}. By looking at the IV curves in *figure 50* we can see that less voltage is required, this means less energy is converted into electrical power, and more into heat energy, which is also a reason why a rise in the temperature of the solar cell is seen.

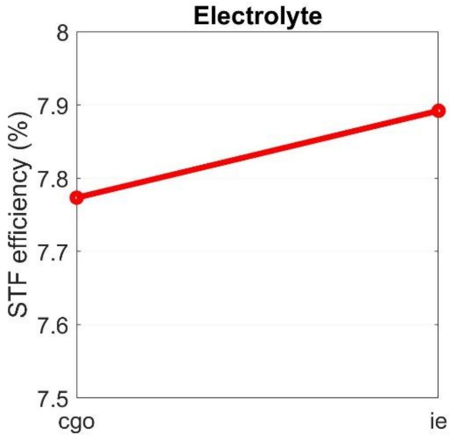

Figure 48- *STF efficiencies varying the electrolyte type.*

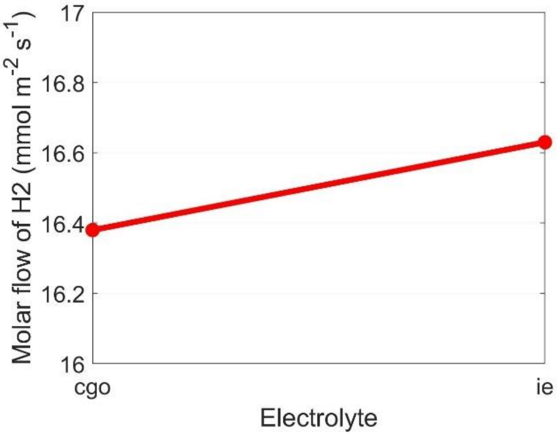

Figure 49- *Molar flow rate of hydrogen produced vs the electrolyte type.*

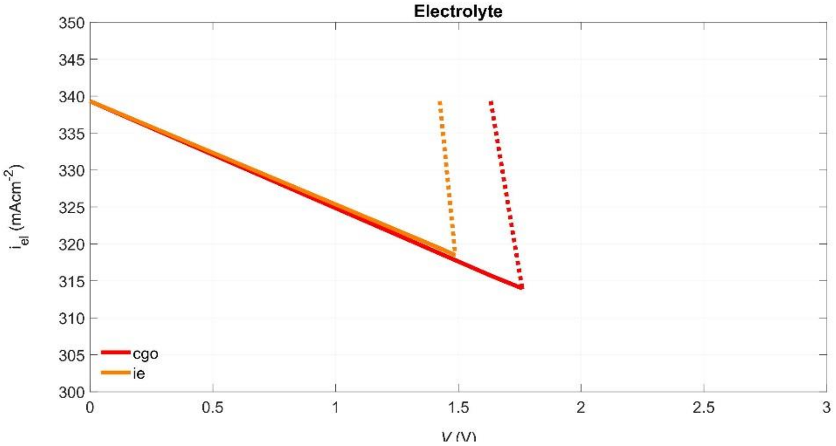

Figure 50- *IV curves for the different electrolyte types.*

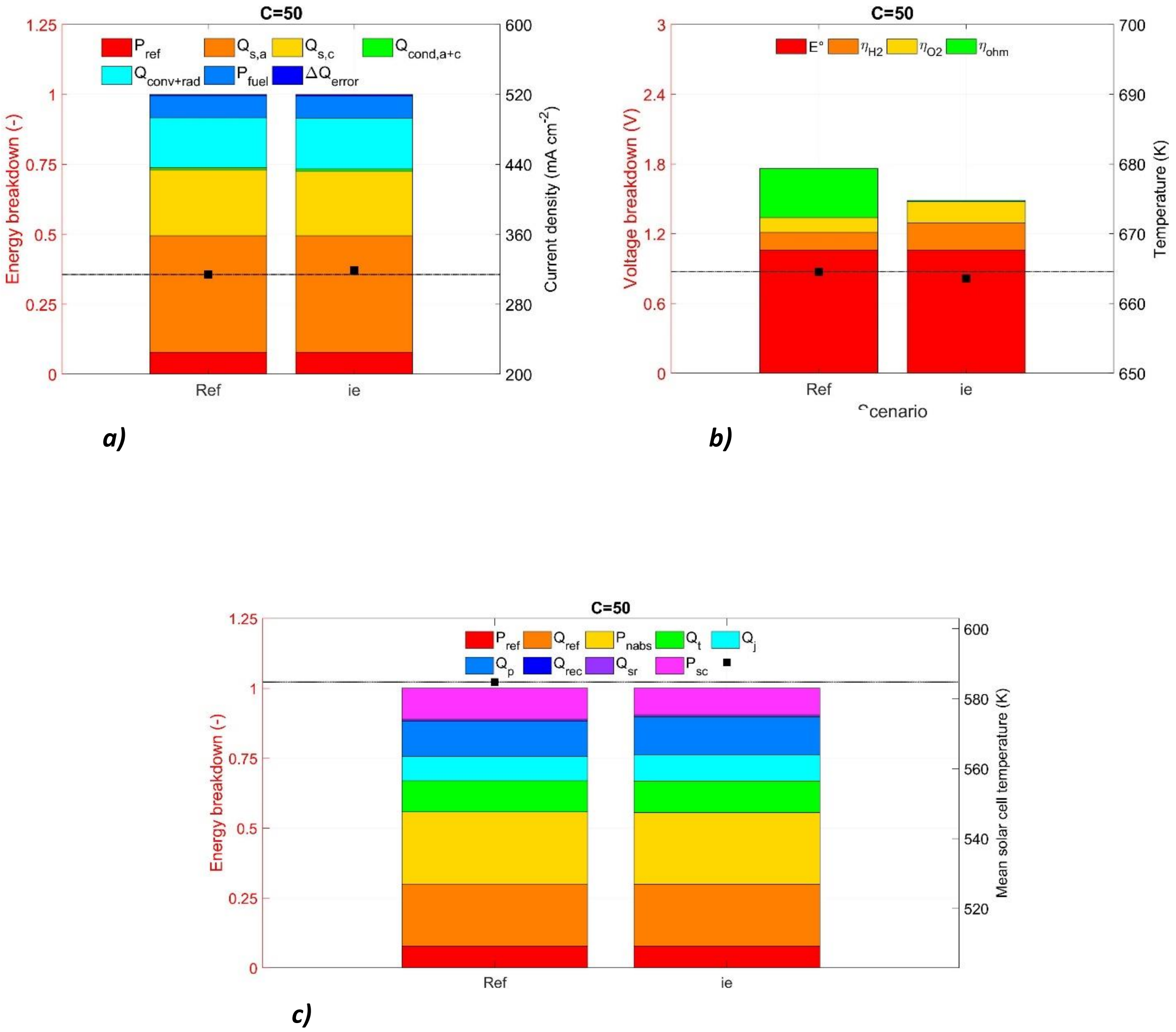

Figure 51- *Breakdown, varying the type of electrolyte, of* ***a)*** *the energy in the whole device, plus current density,* ***b)*** *the voltage in the electrolyser, plus T_{el},* ***c)*** *the energy in the HTSC, plus T_{sc}.*

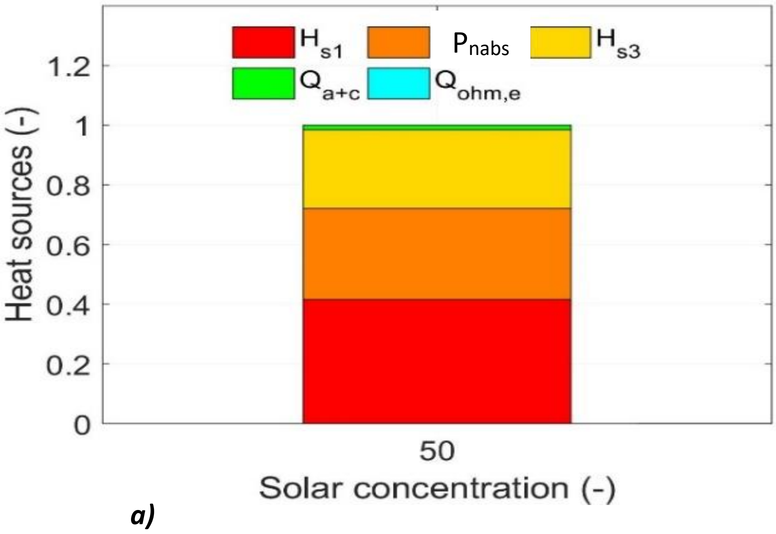

a)

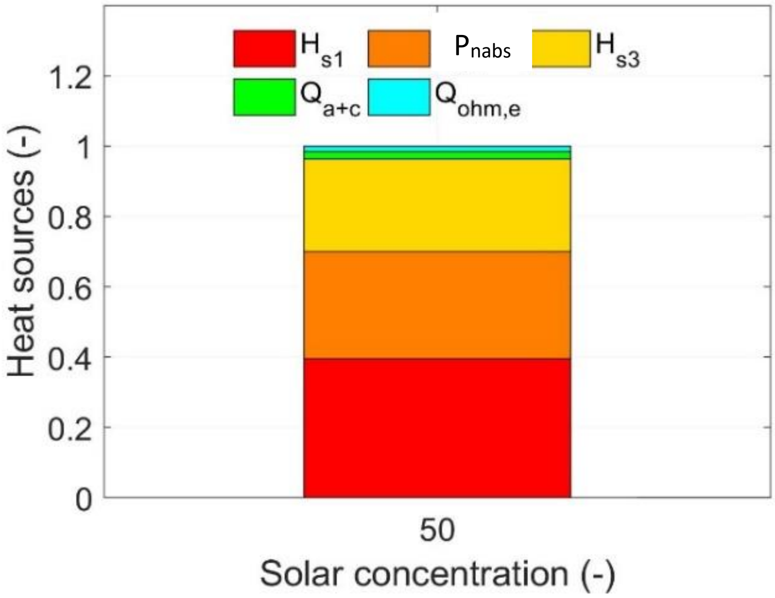

b)

Figure 52- *Heat sources in* ***a)*** *the case of an ideal electrolyte,* ***b)*** *the reference case, during the hydrogen production parametric analysis.*

4.2.7 CATHODE ELECTRODE TYPE

The required voltage by the electrolyser (V_{el}) was also aimed to be reduced by reducing the activation overpotential at the cathode ($\eta_{\mathrm{H_2}}$). For this purpose, we replaced the reference cathode electrode by an ideal one. The characteristic which gave the electrode this attribute was the increased pre-exponential factor of the exchange current density ($k_{\mathrm{H_2}}$).

The results confirmed our expectations, as the overpotential at the cathode, $\eta_{\mathrm{H_2}}$ was reduced from 0.154V in the reference case, to 0.034V in the ideal electrode scenario, due to the increased $k_{\mathrm{H_2}}$. *Figure 56b* shows illustrates this decrease, which enabled the value of V_{el} to be lowered. As $\eta_{\mathrm{O_2}}$ and η_{ohm} remained constant, the voltage required by the electrolyte could only be reduced 7.39% with respect to the reference case. As a consequence, the STF efficiency only experienced a slight increase, from 7.77% in the reference case to 7.83% in this scenario (*figure 53*). The IV curve for this simulation also shows how the current density remains stable whilst the operating voltage decreases, when using an ideal cathode (*figure 55*).

All the other characteristic parameters, remained practically unchanged between the reference case and using an ideal cathode electrode. For example, the molar flow of hydrogen produced increased 0.74% (*figure 54*), the current density increased 0.54% (*figure 56a*), the mean temperature at the solar cell increased 0.44% (*figure 56c*) and the mean temperature of the electrolyser remained exactly at a value of 664.6K (*figure 56b*). As conclusion, the use of an ideal cathode allowed improvements in the performance, but minor ones.

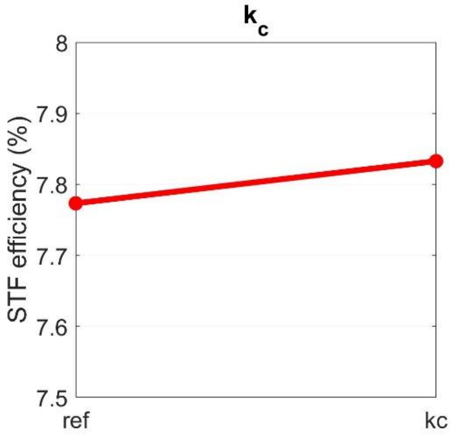

Figure 53- *STF efficiencies varying the cathode electrode type.*

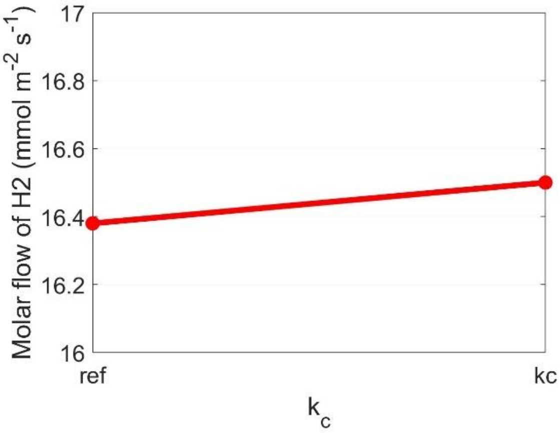

Figure 54- *Molar flow rate of hydrogen produced vs the cathode electrode type.*

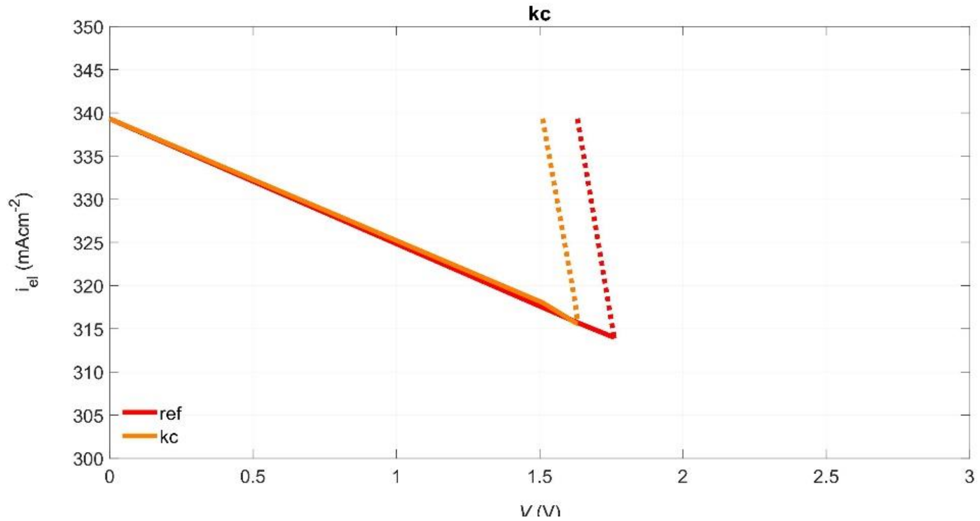

***Figure 55**- IV curves for the different cathode electrode types.*

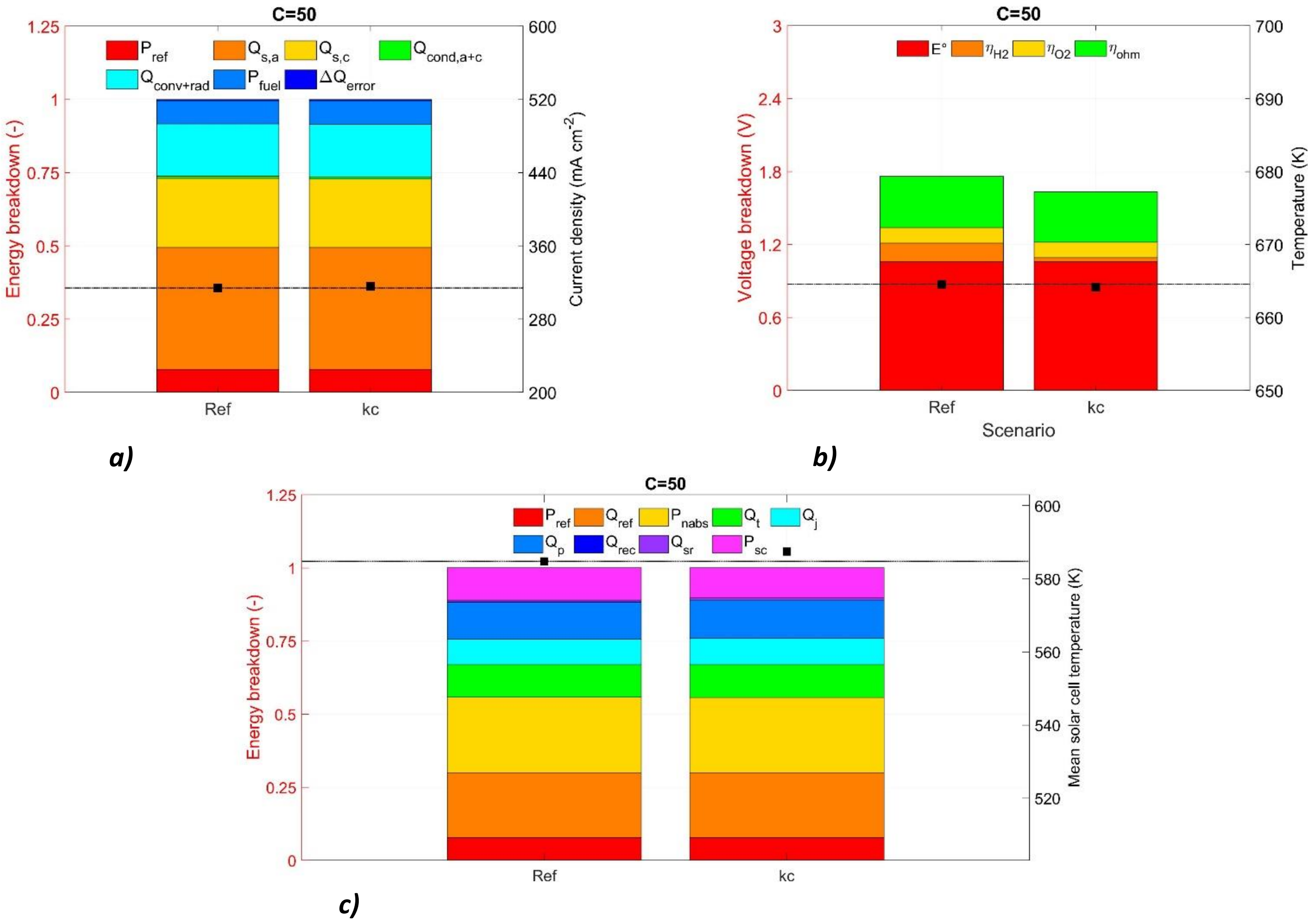

***Figure 56**- Breakdown, varying the cathode electrode type, of **a)** the energy in the whole device, plus current density, **b)** the voltage in the electrolyser, plus T_{el}, **c)** the energy in the HTSC, plus T_{sc}.*

4.2.8 COMBINATION SCENARIO

The parameter studied that most positively affects the energetic and production performance of the device is the number of photoabsorbers operating in series. Operating with three photoabsorbers resulted in an efficiency of 9.97% and a molar flow of 21 mmolm^{-2}s^{-1}. As studied and mentioned in the section "4.2.3 Number of solar cells", when keeping the parameters with the dimensions used in the reference case, the device was unable to operate with two solar cells, and the operation point was unable to be reached, as the voltage required by the electrolyser exceeded the photovoltage produced. In order to be able to further decrease the voltage requirement in the electrolyser and operate using two photoabsorbers, with the aim of improving the STF efficiency and hydrogen production of the device, we aimed at finding a combination of parameters which decrease the voltage required by the electrolyser.

Considering only the effect of each parameter on the V_{el} required, we observe that the values of each parameter that allow the voltage requirements of the electrolyser to be the lowest are the following:

- Height of cathode chamber: 1mm
- Height of anode chamber: 1mm
- Cathode electrode thickness: 100μm
- Inlet velocity at the cathode chamber: 0.1m/s
- Electrolyte type: ideal
- Cathode electrode type: ideal

A simulation was carried out with the combination of the previous values. However, due to the high solar cell temperature risen by this combination, the operating point was unable to be reached. In order to solve this problem and successfully use two photoabsorbers, we compared the solar cell temperatures T_{sc} given when each of these parameters was simulated independently from the others during the parametric study. It was found out that the inlet velocity at the cathode chamber being 0.1m/s was the parameter which lead to the highest HTSC temperature increase, in comparison with the reference case (18.79% increase), with a difference of 73.1K from the next highest temperature increase, caused by the height of the anode chamber being 1mm (this caused a 6.30% increase in T_{sc} with respect to the reference case). For this reason, we decided to modify the value of the inlet velocity at the cathode chamber, increasing it starting from 0.1m/s until we were able to successfully obtain the operating point of the integrated device (using the same values as used in the parametric study: 0.1m/s, 0.5m/s, 1m/s, 1.5m/s and 2m/s).

The operating point was achieved with an inlet velocity value of 1m/s, in other words, with "combination of parameters 3" in *table 4*. As a result, the HTSC-SOE integrated device was able to operate successfully with two photoabsorbers, working at temperatures of T_{sc}=652.6K (*figure 58a*) and T_{el}=793.8K (*figure 59a*). Although the operating temperature of the photoabsorber assembly T_{sc} increased 11.59% with the reference case, the photocurrent was improved from the value of 313.9 mAcm^{-2} to 527.5 mAcm^{-2} (*figures 57a* and *57b*). Furthermore, the voltage required by the electrolyser experienced a 33.35% decrease with respect to the reference case (1.76V was lowered to 1.173V), due to the high operating T_{el} which led to a drastic decrease in the ohmic and cathode overpotentials. This can be observed in *figures 59a* and *59b.*

Each of the positive impacts on the performance of the individual parameters tested in the parametric analysis can be perceived in the results of this simulation. The energy balance of the whole integrated device in *figure 57a* shows the significant increase in current density and P_{fuel}

with respect to the reference case. The balance of the solar cell shows, in turn, the increase in P_{sc} (*figure 58a*). *Figures 59a* and *59b* illustrates the massive decrease in the voltage lost in the electrolyte η_{ohm} (mostly due to the use of an ideal electrolyte), and in the cathode overpotential η_{H_2}(mostly due to the use of an ideal cathode electrode), which together lead to the massive decrease in the voltage requirements by the electrolyte. All these enhancements lead to significant improvements in the energetic and production performance of the device, obtaining an efficiency of 14.18% and a molar flow rate of hydrogen of 29.87 mmolm^{-2}s^{-1} (the results of the reference case were 7.77% and 16.38 mmolm^{-2}s^{-1}).

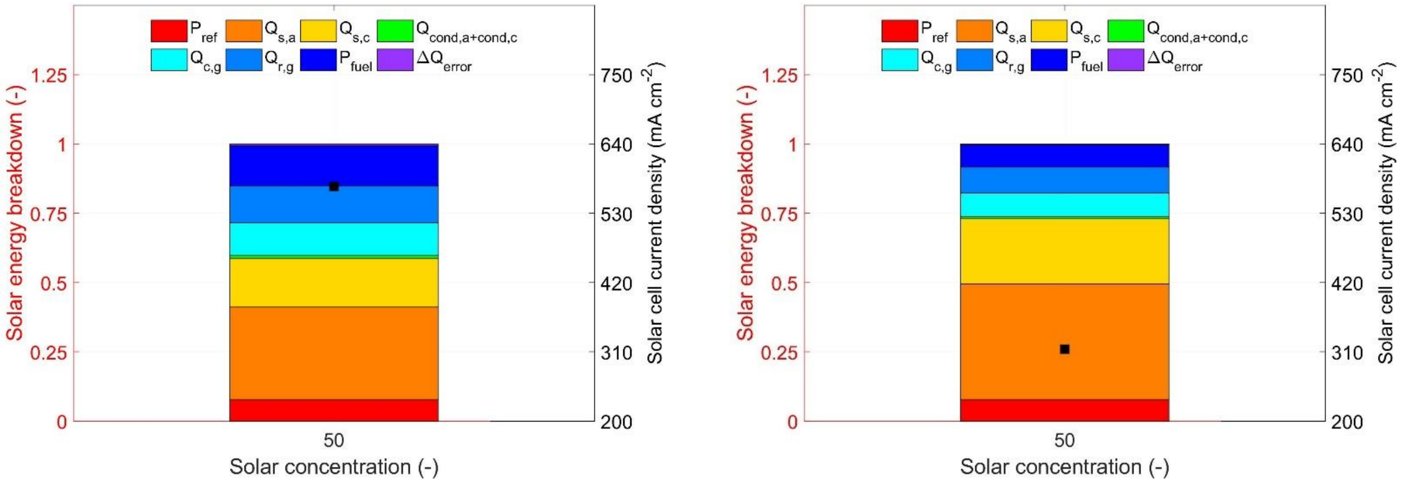

a) ***b)***

Figure 57*- Energy breakdown of the whole device plus current density in the case of* ***a)*** *combination of parameters (3),* ***b)*** *reference case.*

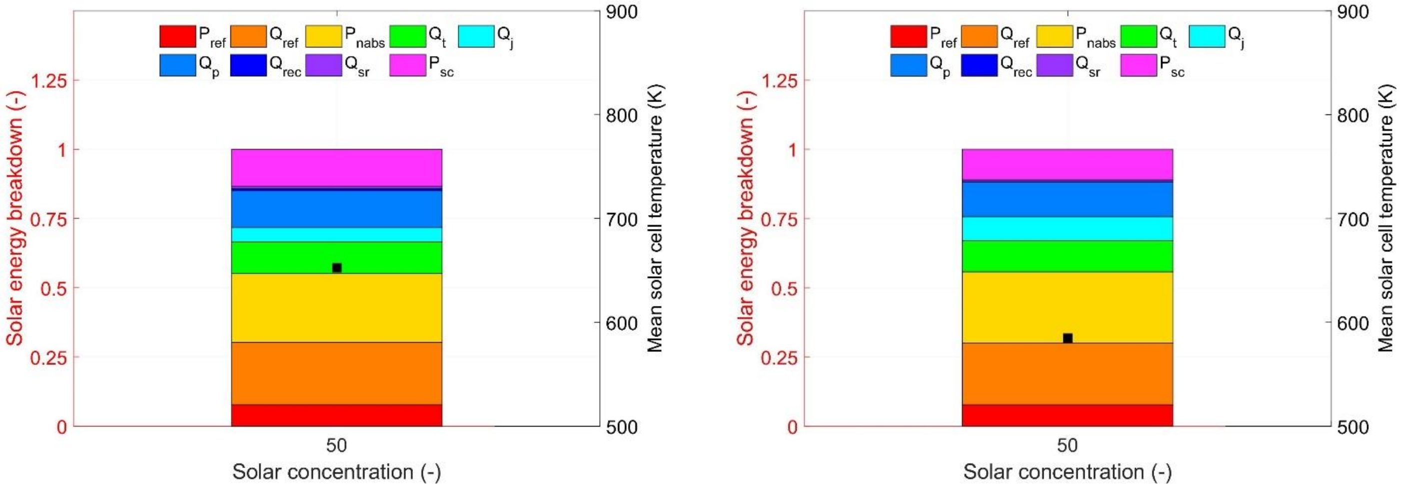

a) ***b)***

Figure 58*- Energy breakdown of the HTSC plus* T_{sc} *in the case of* ***a)*** *combination of parameters (3),* ***b)*** *reference case.*

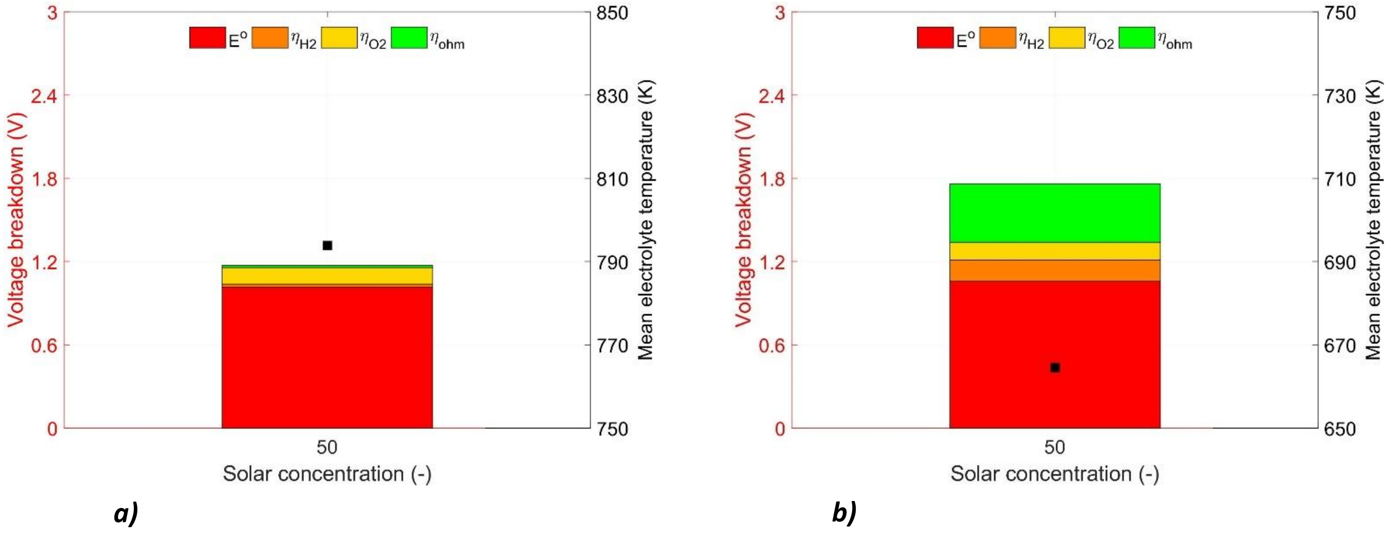

Figure 59- *Voltage breakdown plus T_{el} in the case of* ***a)*** *combination of parameters (3),* ***b)*** *reference case.*

5. SYNGAS PRODUCTION SIMULATION

In the same way to the hydrogen production simulation, we carried out a parametric analysis in order to assess the impact of a certain number of variables on the energetic and production performance of the device under the conditions for syngas production.

As mentioned, we aim to generate synthetic fuels via the Fischer-Tropsch synthesis process, using synthetic gas (syngas) produced in our device. During this process the H_2 and CO building blocks undergo a chain growth reaction (polymerisation), forming heavy-weight liquid hydrocarbons according to the following reaction, represented by *equation 18* (being $\sim\mathrm{CH_2}\sim$ the product building blocks that concatenate in order to form the liquid synthesis fuel). The H_2/CO ratio can be adjusted via upstream water gas shift reaction via *equation 19* [23].

$$\mathrm{CO} + 2\mathrm{H_2} \rightarrow \sim\mathrm{CH_2}\sim \; + \; \mathrm{H_2O} \qquad (18)$$

$$\mathrm{CO_2} + \mathrm{H_2} \leftrightarrow \mathrm{CO} + \mathrm{H_2O} \qquad (19)$$

As represented in *equation 18*, the needed H_2/CO ratio of the syngas in order for the Fischer-Tropsch reaction is $H_2/CO = 2$. This is, in consequence, the ratio of products we aim to achieve during the operation of the integrated HTSC-SOE device and, thus, the parameter we are going to focus on in order to assess the performance of the device.

5.1 REFERENCE CASE

The values of the parameters used in the reference case are summarised in *table 5*.

Table 5- *Fixed parameters in the reference case for the syngas production simulation.*

PARAMETER	**REFERENCE CASE**
Inlet temperature of the species at the electrolyser (K)	423
Inlet velocity at the cathode (m/s)	2
Inlet velocity at the anode (m/s)	2
Anode inlet gas molar ratio O_2/N_2	0.21/0.79
Cathode inlet gas molar ratio H_2/H_2O	0.1/0.6
Cathode inlet gas molar ratio CO/CO_2	0.05/0.25
Cathode chamber height (mm)	1
Cathode thickness (µm)	100
Cathode porosity	0.48
Cathode tortuosity	5.4
Electrode thickness (µm)	10
Anode chamber height (mm)	2
Anode thickness (µm)	100
Anode porosity	0.48
Anode tortuosity	5.4
Chamber length (cm)	8
HTSC length (cm)	4
Electrolyser length (cm)	4
Flow direction	Parallel flow
Number of photoabsorbers in series	3
Solar concentration (suns)	50
Electrolyte type	CGO
Operating pressure (atm)	1

The simulation carried out with the previous parameters showed, to start with, a higher efficiency than the hydrogen production simulation. This was due to the fact that we directly started using three photoabsorbers. The achieved solar cell efficiency η_{sc} and electrolyser η_{el} reached values of 15.09% and 71.01% respectively. Meanwhile, the STF efficiency was worth 10.06%. These three results can be observed in *figure 60b*.

The operating temperature of the solar cell and the electrolyser components in this scenario resulted 573.5K and 647.9K, respectively. These values result to be slightly lower than the ones obtained during the reference case for the hydrogen production simulation (584.8K for the temperature of the solar cell and 664.4K for the one of the electrolyser).

In addition, the results showed the H_2/CO ratio obtained a value of 9.963, which was far from our goal ($H_2/CO=2$). This was because, as seen in *figure 60a*, the molar flow rate of production of hydrogen was much greater than that of carbon monoxide (19.12 mmolm^{-2}s^{-1} and 1.92 mmolm^{-2}s^{-1} respectively).

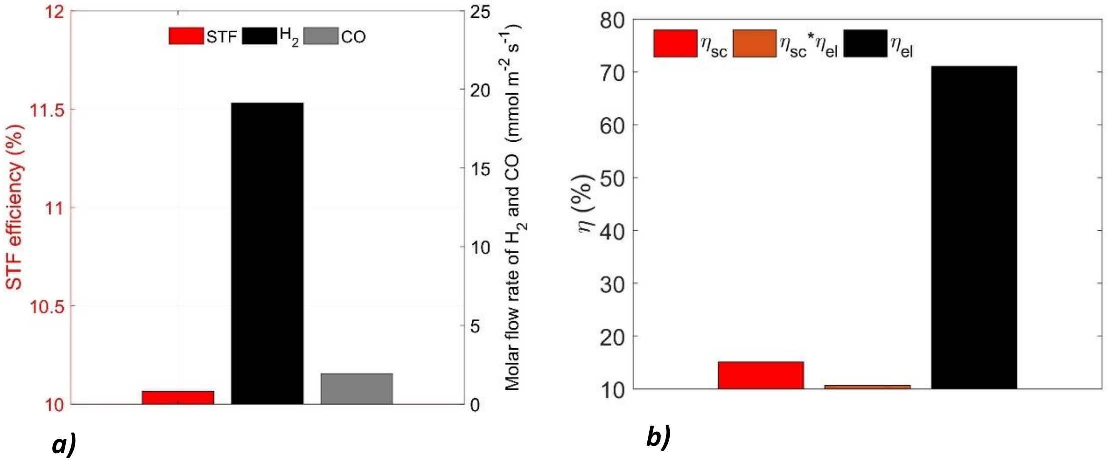

Figure 60a) *STF efficiency, molar flow rate of H_2 and CO for the reference case of the syngas production simulation,* ***b)*** *solar cell efficiency, electrolyser efficiency and device efficiency for the reference case of the syngas production simulation.*

5.2 RESULTS OF THE PARAMETRIC ANALYSIS

The parameters studied in each different scenario during the syngas production parametric analysis are summarised in the following table

Table 6- *Parameters used for the different case scenarios of the syngas production simulation. The symbol '-' indicates no modification with respect to the reference case.*

SCENARIO	$x_{H_2O,0}$ **(-)**	$u_{c,0}$ **(m/s)**
Reference case	0.60	2
1	0.50	-
2	0.40	-
3	0.25	-
4	0.15	-
5	0.10	-
6	0.05	-
7	-	0.5
8	-	0.1

5.2.1 INLET MOLAR FRACTION OF H_2O

With the aim of reducing the H_2/CO ratio from the current value of 9.963 down to the desired value of 2, we reduced the inlet molar fraction of water. As the fraction of water at the inlet decreases, that of CO_2 increases. This is because the inlet molar fraction of carbon dioxide, $x_{\mathrm{CO_2},0}$, increases, as it is calculated as:

$$x_{\mathrm{CO_2},0} = 1 - x_{\mathrm{H_2O},0} - x_{\mathrm{CO},0} - x_{\mathrm{H_2},0} \qquad (20)$$

Reducing $x_{\mathrm{H_2O},0}$ and increasing $x_{\mathrm{CO_2},0}$ was expected to reduce the formation of H_2 gas and increase the production of CO, thus reducing the H_2/CO ratio.

We carried out seven simulations varying the inlet molar fraction of water, using the values $x_{\mathrm{H_2O},0}$= 0.60, 0.50, 0.40, 0.25, 0.15, 0.10, 0.05. In fact, the results showed how the H_2/CO ratio decreased as expected, obtaining the values of 9.963, 7.813, 6.246, 4.269, 2.941, 2.142 and 1.078, respectively. *Figure 61* shows us how, as $x_{\mathrm{H_2O},0}$ decreased, the molar flow rate of produced H_2 decreased, whilst the one of CO increased. In order to better understand the correlation between these two parameters, we made a plot of the H_2/CO ratio versus the inlet molar fraction of water, shown in *figure 62*. Our next step was carrying out a polynomial curve fitting of the resulting plot, with the goal of obtaining the coefficients of the equation which best describes the behaviour shown. We adjusted the plot to a polynomial of order three, and we obtained the equation: $y = 48.0365x^3 - 43.0154x^2 + 25.2083x - 0.0472$ (y being the H_2/CO ratio and x being $x_{\mathrm{H_2O},0}$). After evaluating the accuracy of the fitting, we used it to calculate, exactly, the inlet molar fraction of water needed to obtain a H_2/CO ratio of 2, the obtained value was: $x_{\mathrm{H_2O},0}$=0.095. With this exact value we would obtain a H_2/CO ratio of 2.0006, using the adjusted polynomial.

Figure 63a shows us the current density produced by the photoabsorber assembly decreases very gradually as the inlet molar fraction of water decreases. Similarly, the overall energy balance breakdown of the whole system remains practically unaffected. Meanwhile, we can see how the mean temperature of the solar cell decreases as $x_{\mathrm{H_2O},0}$ decreases, obtaining a minimum temperature of 563.8K. The decrease in the operating temperature of the solar cell can be explained by the decrease in the internal heat sources. That is concluded as the sum of Q_{tot} and Q_{b} (joint contribution of Q_{p}, Q_{j}, Q_{t}, Q_{rec}, Q_{sc}) decreases as the inlet molar fraction of water decreases. This can be observed from *figure 63c*, which also lets us see how the power produced in the solar cell (P_{sc}) increases as the $x_{\mathrm{H_2O},0}$ decreases, in exchange for decreasing the heat loss due to the Peltier effect Q_{P} decreases. This last heat source decreases as a consequence of the current density decreasing. The maximum percentage increase in P_{sc} obtained with respect to the reference case is 6.16%, when $x_{\mathrm{H_2O},0}$=0.05, as less energy is used to heat the photoabsorber assembly, so more is converted into useful power. Adding on, the results showed how the operating temperature of the electrolyser components decreased as $x_{\mathrm{H_2O},0}$ decreased (1.77% decrease was the maximum one observed, it occurred when the inlet molar flow rate of H_2O was at its lowest value), shown in *figure 63b*. As V_{el} increases, the operating point gets closer to the maximum power point of the HTSC, which means the heat sources decrease, and so cause T_{el} to decrease. This decrease in temperature led to an increase in the required voltage by the electrolyser, as all of the components which contribute to this voltage (the equilibrium potential E°, overpotentials at cathode and anode, $\eta_{\mathrm{H_2}}$ and $\eta_{\mathrm{O_2}}$, and voltage loss in the electrolyte η_{ohm}) slightly increased as the inlet molar fraction of water decreased. The voltage required increased from 1.873V in the reference case to 2.01V in the scenario where $x_{\mathrm{H_2O},0}$=0.05. In conclusion we can depict form *figure 61* that the STF efficiency increases as the inlet molar flow rate of water decreases, achieving a maximum efficiency of 10.34% at $x_{H_2O,0}$=0.05. The STF efficiency depends on both the quantity of H_2 and CO produced and the Gibbs free energy of H_2 and CO (see *equation 16*). As reducing the inlet molar fraction of water increases the amount of CO produced, in expense of reducing that of H_2 generated, as the Gibbs free energy is bigger for CO than for H_2, the overall effect in the STF efficiency causes it to increase.

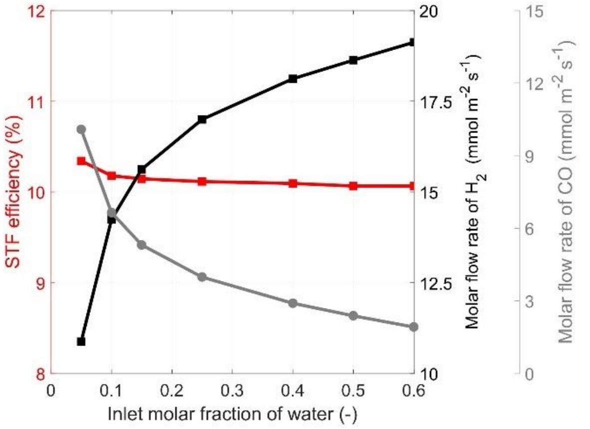

Figure 61- *Comparison of STF efficiency, molar flow rate of H_2 and molar flow rate of CO varying the inlet molar fraction of water.*

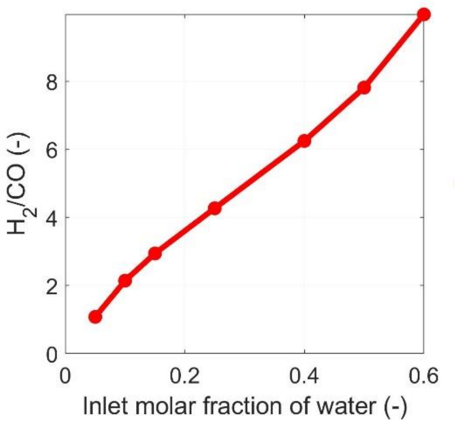

Figure 62- *Variation of the H_2/CO ratio with the inlet molar fraction of water.*

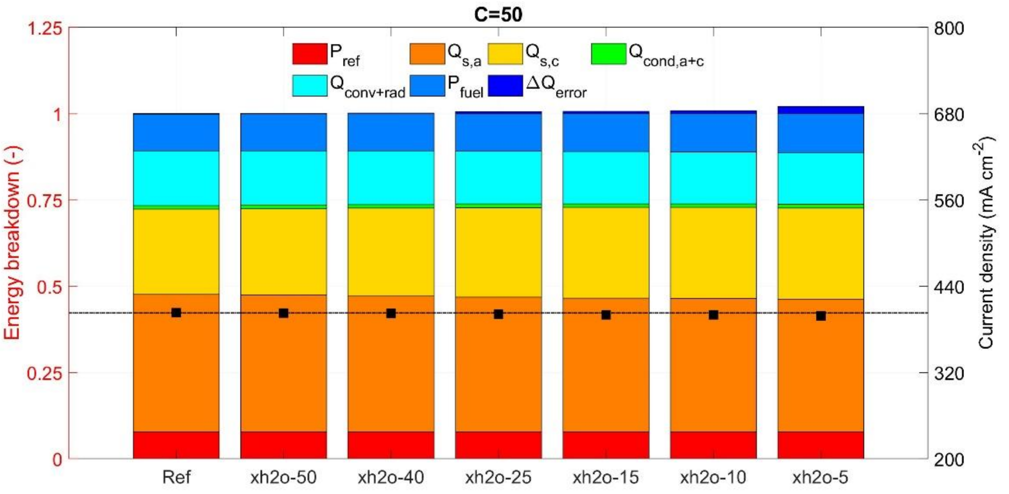

Figure 63a) *Energy breakdown in the device plus current density, varying the inlet molar fraction of water.*

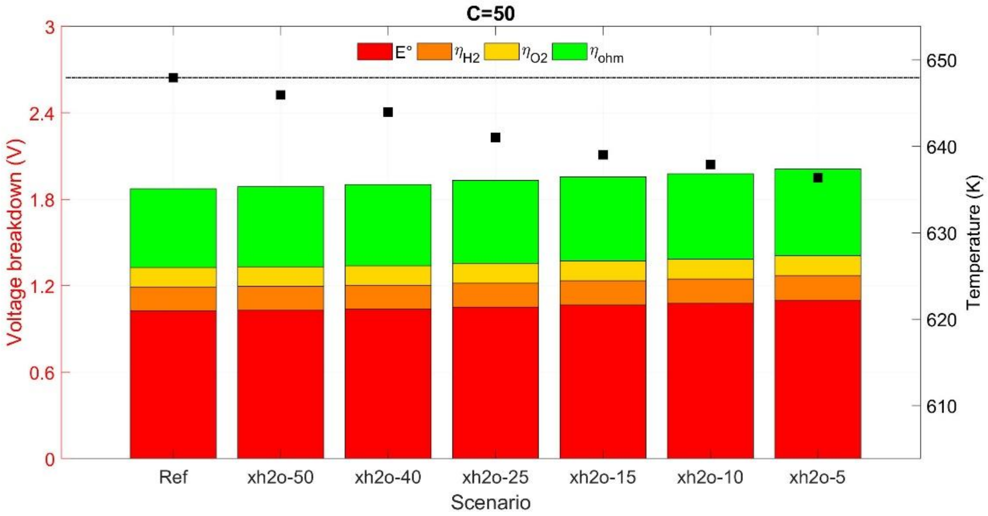

Figure 63b) *Voltage breakdown in the device plus Tel, varying the inlet molar fraction of water.*

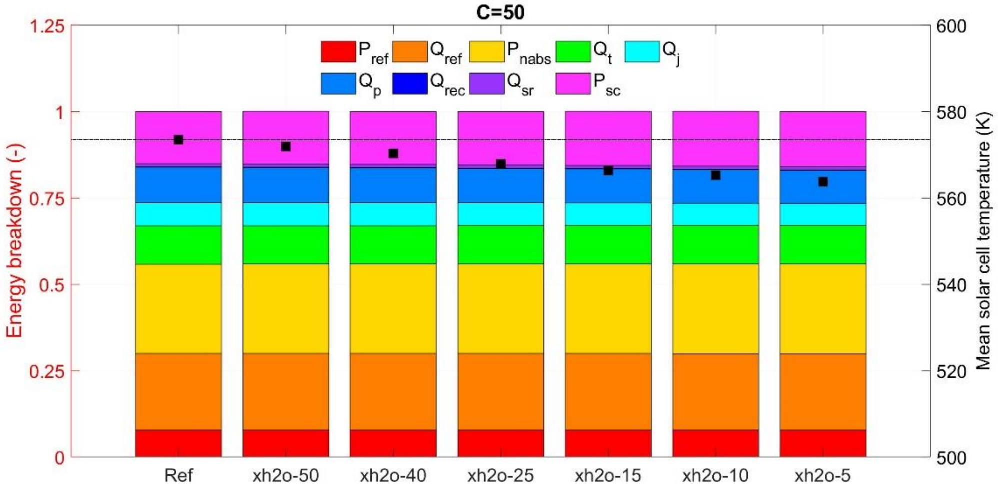

Figure 63c) *Energy breakdown in the HTSC plus T_{sc}, varying the inlet molar fraction of water.*

5.2.2 INLET VELOCITY AT THE CATHODE CHAMBER

A second approach to decrease the H_2/CO ratio obtained in the reference case to approximate it to the desired value involved increasing the temperature of the electrodes. We reduced the inlet velocity at the cathode chamber from 2m/s to 0.5m/s and then to 1m/s. With these modifications we expected the same effect as when we reduced the inlet velocity during the hydrogen production simulation. This is, reducing the molar flow in the cathode chamber causes a reduction in the sensible heat at the cathode, therefore less energy is needed to heat the species in the chamber. This would cause, in turn, an increase in T_{el}. This increase in temperature was hypothesised to cause an increase in the production of CO compared to that of H_2.

The following graph was obtained from Licht et al's paper from 2009 [10]. It provides a graphical way of understanding the indicated decrease in electrolysis energy, with increase in temperature.

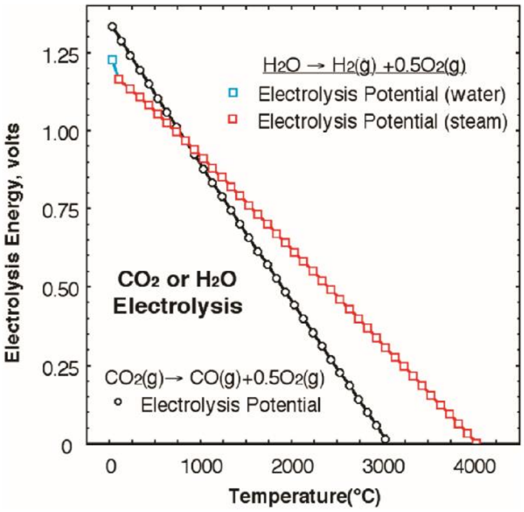

Figure 64- Potential needed to electrolyze carbon dioxide or water [10].

The results extracted from our simulations supported our hypothesis. We verified this premise though the use of COMSOL, calculating the equilibrium potentials of H_2O and CO_2 both at 2m/s and at a lower speed (we took 0.5m/s). The calculated values showed that, as the temperature increased, both the equilibrium potentials of H_2O and CO2 decreased, however comparing each of them individually we noticed the equilibrium potential of water was reduced in 0.0234V, whilst that of carbon dioxide was reduced in a bigger quantity, 0.0343V. This was able to prove that at higher electrode temperatures, the minimum voltage required becomes more favourable for CO_2 splitting than for H_2O splitting, producing more CO than H_2 and thus reducing the ratio H_2/CO. In other words, increasing the temperature in the electrodes is beneficial for increasing the CO rate.

In fact, *figure 66* illustrates the decrease in the ratio H_2/CO as the velocity decreases, obtaining a 40.63% decrease from 2 to 0.1m/s, reaching a value of ratio of 5.915. We can extract the same information from *figure 65*, as the H_2 gas production decreases as the velocity decreases, whilst the CO production increases. The increase in the operating temperature of the electrolyser can be seen in *figure 67b*, reaching a percentage increase of 11.30% with respect to the reference case.

This increase causes, in turn, a decrease in the activation and ohmic overpotentials, which together lead to a decrease in the required voltage. The minimum required voltage was obtained at the lowest inlet velocity, experiencing a reduction of 16.76% in comparison to the reference case. On the other hand, the same as in the hydrogen production simulation during the variation of the inlet chamber velocity occurred. The higher temperature of the fluid in the chamber caused a meaningful increase in the temperature of the solar cell. T_{sc} increased in 16.56% when $u_{c,0}$=0.5m/s with respect to the reference case (see *figure 67c*). This same figure shows us an increase in the convection and radiation losses to the atmosphere, explained by the fact that, as the fluid in the cathode is now at a higher temperature compared to the reference case (due to the decrease in the mass flow), the fluid will in turn heat the glass cover. A higher thermal gradient, in comparison with the reference case develops between the glass cover and the exterior, which causes the increase in heat lost by convection and radiation. The sensible heats in the cathode $Q_{s,c}$ and anode chamber $Q_{s,a}$ decrease and increase, respectively, due to the same reasons as in the same scenario during the hydrogen production simulation. The decrease in velocity causes a decrease in the mass flow rate inside the cathode chamber, which, looking at *equation 17*, decreases the sensible heat at the cathode. The sensible heat at the anode increases, in comparison with the reference case, due to the increase in the temperature difference between its inlet and outlet.

The STF efficiency experiences a slight increase from 2 to 0.5m/s, from 10.06% to 10.12% (*figure 65*), which can be explained due to the bigger increase in CO than in H_2 generation (see *equation 16*). However, when the velocity is further decreased to 0.1m/s, the efficiency is lowered from 10.12% to 9.50% because, even though the V_{el} decreases a little bit more, the current density shown in *figure 67a* suffers a meaningful decrease (404.8 to 379.3 mAcm^{-2} from 0.5 to 0.1m/s).

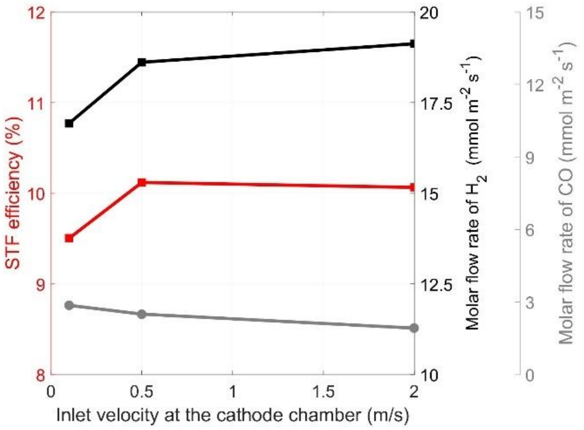

Figure 65- *Comparison of STF efficiency, molar flow rate of H_2 and molar flow rate of CO varying the inlet velocity at the cathode chamber.*

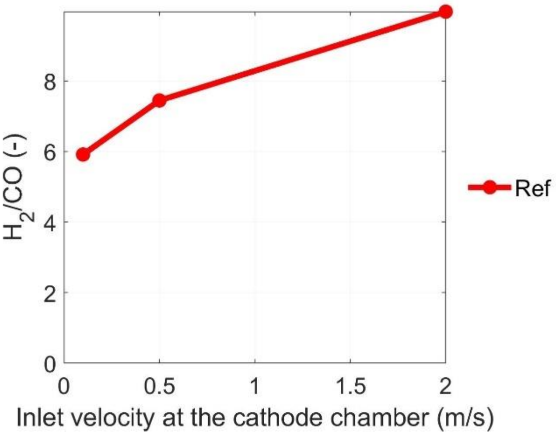

Figure 66- *Variation of the H_2/CO ratio with the inlet velocity at the cathode chamber.*

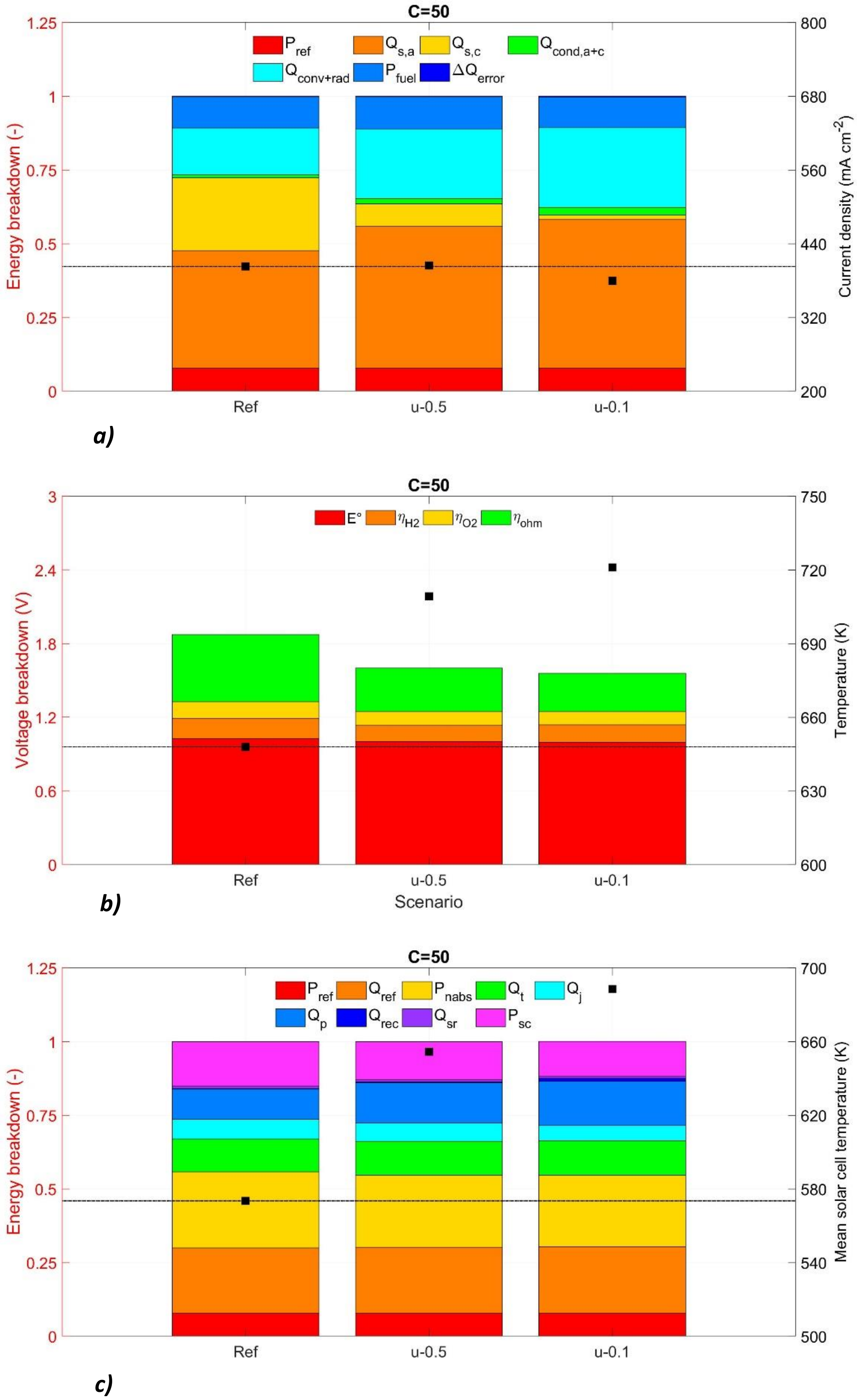

Figure 67a) *Energy breakdown in the device plus current density,* ***b)*** *voltage breakdown plus* T_{el}*,* ***c)*** *energy breakdown in the HTSC plus* T_{sc}*, varying the inlet velocity at the cathode chamber.*

6. COMPARISON BETWEEN ORIGINAL STUDY AND PRESENT STUDY

The original study was carried out at a number of different solar concentrations. As the current research was limited to a concentration of 50 suns, the comparison between both devices, structures and results is going to be focused in the case of 50 suns. As mentioned in the introduction, the main functional differences between both proposed devices are: the use of a glass cover and support and the integrated approach used in the present study.

During the hydrogen production simulation, the same values for all parameters were used in the reference case scenario, this means the comparison of the results will allow us to see, directly, the impact the changes in the device structure have on the performance. The results extracted from the hydrogen production simulation in the original research at 50 suns show an attained STF efficiency of 8.24%, and the molar flow rate of hydrogen produced accounted to 17.37 mmolm^{-2}s^{-1}. The maximum efficiency reached in the previous study was found when operating with three photoabsorbers instead of 4, and had a value of 9.78%. Meanwhile, the maximum flow of fuel produced was worth 20.62 mmolm^{-2}s^{-1}, and was achieved, too, when three photoabsorbers were used. In comparison, the results from the reference case simulation in the present study were 7.77% as the STF efficiency and 16.38 mmolm^{-2}s^{-1} of H_2 produced. The maximum efficiency and H_2 molar flow rate reached were 9.97% and 21 mmolm^{-2}s^{-1}, respectively, both results obtained when operating with three photoabsorbers. Comparing both studies, it seems both device designs show similar energetic and production performances. Only minor differences can be detected, as both the STF efficiency and the molar flow rate of hydrogen increase when using an integrated model, but only in small amounts (around 1% and 1 mmolm^{-2}s^{-1} difference between both models). However, when improvements are made in the structure, design, or material quality used, the integrated approach has a slightly more positive impact in the performance of the device, in comparison with the quasi-integrated model. It can also be determined that finding the appropriate conditions to operate with a lower number of photoabsorbers is crucial in order to improve the performance of the device, both using a quasi-integrated or a fully integrated approach. This conclusion is extracted from the fact that both, the original and current model, show the best performances when this is the parameter that is modified. Lastly, considering the fact that in the present study we conducted additional simulations where we combined various values of parameters which we believed could operate together to improve the performance, it is of interest to add in this section the importance of such kind of simulations, as with it we were able to obtain the highest possible efficiency (14.18%), in comparison with both the previous and current model, in their respective reference cases or cases of maximum performance. It would be appealing to conduct further similar simulations adding other variations, in order to try to further increase this performance metrics and provide more valuable design guidelines for the device.

Concerning the syngas production simulation, the original study operated with four photoabsorbers during the reference case, whilst the current study functioned with three. We decided to use three rather than four HTSCs in this study due to the small variations in the energetic and production performance achieved during the hydrogen simulation (when operating with four photoabsorbers). As we identified working with three photoabsorbers had a significant improvement in the performance, we established this value as our reference case, in order to achieve further enhancements with the variation of the remaining parameters. For this reason, the difference in the parameters used during the reference case scenario, we are unable to fairly compare both devices under the syngas production simulation. The quantitative results obtained during the previous study, during the reference case, were the following: 8.34% STF efficiency, 16.2 mmolm^{-2}s^{-1} of hydrogen produced and 1.34 mmolm^{-2}s^{-1} of CO produced. During the best-case scenario, the original device attained a STF efficiency value of 10.20% (when operating with three photoabsorbers) and a H_2 and CO molar flow rates of 19.72 mmolm^{-2}s^{-1} and 5.05 mmolm^{-2}s^{-1}, working with three photoabsorbers and with an inlet molar fraction of water of 0.1 respectively. In contrast, an 10.06% STF efficiency, a 19.12 mmolm^{-2}s^{-1} H_2 production flow rate and a 1.92 mmolm^{-2}s^{-1} CO production flow rate were obtained during the reference case scenario of the present study. The maximum flow rate of H_2 produced during the whole parametric study was the one generated in the reference case, whilst the maximum flow rate of CO was produced in the case of $x_{\mathrm{H_2O},0}$=0.05, and had a quantitative value of 10.09 mmolm^{-2}s^{-1}. Similarly, the maximum STF efficiency was also obtained in that case scenario ($x_{\mathrm{H_2O},0}$=0.05), and had a value of 10.34%. The comparison between both models concerning the syngas production simulation also leads us to understand that modifying and improving the photoabsorber assembly has a meaningful improvement in the performance of the device. We are unable to confirm the reason of the increase in efficiency from the previous model to the current one, as it could be due to either, operating with a lower number of photoabsorbers or to the actual structure of the device. Adding on, comparing both studies under their best-case scenarios, the results obtained in the original study show more interesting values of hydrogen production. The quasi-integrated device was able to supply a higher amount of H_2 than the integrated design, even when working with the same number of photoabsorbers. We are unable to fairly compare the maximum amount of CO gas produced in both maximum case scenarios, as not only the present study had the advantage of working with three photoabsorbers, but it was also assessed with a value of 0.05 as the inlet molar fraction of water, whilst the original study simulated the reaction with a minimum value of 0.10.

Table 7- *Summary of the numerical results obtained during the hydrogen production simulation in the original and present models.*

	Reference case result	**Maximum results obtained**
ORIGINAL MODEL		
STF efficiency (%)	8.24	9.78
H_2 molar flow rate (mmolm^{-2}s^{-1})	17.37	20.62
PRESENT MODEL		
STF efficiency (%)	7.77	9.97
H_2 molar flow rate (mmolm^{-2}s^{-1})	16.38	21

Table 8- *Summary of the numerical results obtained during the syngas production simulation in the original and present models.*

	Reference case result	**Maximum results obtained**
ORIGINAL MODEL		
STF efficiency (%)	8.34	10.20
H_2 molar flow rate (mmolm^{-2}s^{-1})	16.20	19.72
CO molar flow rate (mmolm^{-2}s^{-1})	1.34	5.05
PRESENT MODEL		
STF efficiency (%)	10.06	10.34
H_2 molar flow rate (mmolm^{-2}s^{-1})	19.12	19.12
CO molar flow rate (mmolm^{-2}s^{-1})	1.92	10.09

7. POSSIBLE FURTHER IMPROVEMENTS

As mentioned, during the syngas production simulations we aimed at achieving a H_2/CO ratio of exactly 2. This was assessed via two approaches. The first one involves controlling the amount of water at the inlet, as studied, whilst the second approach involves increasing the temperature of the electrolyser's components. Due to lack of time, we were unable to carry out more simulations, varying other parameters which we believed could help improve the performance and completing the parametric study. However, we believe T_{el} could have also been improved by increasing the temperature of the reactants at the inlet of the cathode chamber, as heat transfer by convection would have led to increased cathode electrode temperature. Increasing the solar concentration at which the simulation took place could have also helped to increase the solar heating, and thus augment the component's temperature, however this may have had increased the temperature of the photoabsorber, which is not a desired effect. Furthermore, we hypothesised that decreasing the number of photoabsorbers used in the assembly would have led to an increased current density, which may have also helped to increase the operating temperatures.

In general terms, concerning the heat lost due to reflection and convection and radiation heat losses in the top glass cover, a study can be conducted in order to find the material which most appropriately conducts heat and allows light to be transmitted into the solar cell, whilst reducing the losses. The reflectance and the thickness of the material can be two parameters of interest.

As commented in the section above, in order to improve the performance of the device, it is interesting to vary the characteristics of the employed photoabsorbers. Improving the quality of the solar cell would lead to increased photovoltages and photocurrents provided, which will increase the efficiency of the photoabsorber assembly and thus the STF efficiency of the integrated device. Good surface passivation of the front and rear contacts could be used in order to decrease their surface recombination velocity, this would lead to an increase in the excess electrical carrier density and on the open circuit current V_{oc}. If the photogenerated carriers do not recombine before they reach the contact, the short circuit current is also increased, an, as a consequence, the cell efficiency increases. A back-surface field (BSF) could also be used to limit the surface recombination at the back surface and so improve the V_{oc}. It would however be a problem if the BSF was not transparent, as the non-absorbed light by the photoabsorber would hit the opaque BSF layer and heat that material plus the HTSC, rather than heating the electrolyser components. Adding on, using a solar cell with good material quality would also help increase the efficiency, as a higher base and emitter lifetime also have a positive effect on the V_{oc}. Furthermore, the optical properties of the solar cell also have an impact on its efficiency and the V_{oc} produced, so varying parameters which increase the absorption and reduce the reflection would be interesting, as, to obtain high efficient solar cells, light needs to be effectively coupled into the wafer to be able to contribute to the photocurrent. In order to achieve this, the use of an ARC (anti-reflection coating) will reduce the external reflection of the top of the wafer, whilst introducing surface texture will create pyramid-shapes in the top layer which increase the surface area, causing light to be trapped when internal reflection occurs. If we placed a layer of silver in the back side of the cell, the light trying to escape would be reflected back inside. These two last approaches cause the light coupling inside the cell to be increased due to the double rebound effect. Designing the device to reduce front shadowing would also help to further increase the light coupled in the cell. The technology used to develop the solar cell (e.g. the doping process used) could also help its quality, and thus its efficiency to increase, although these is far from our point of interest.

With reference to the geometrical design of the device, a feasible structure which allows the non-absorbed heat energy in the photoabsorber assembly to be reflected towards the anode electrode can be searched, in order to help improve the temperature of the electrolyser components, and therefore reduce the voltage requirements. A reflective material placed at the lower boundaries of the anode chamber would contribute to the reflection of the heat towards the electrolyser's electrode. The following figures could represent examples of such configuration. Playing with the angle steepness of the reflective wall could be a parameter to consider, in order for the maximum possible heat to be reflected towards the electrolyser.

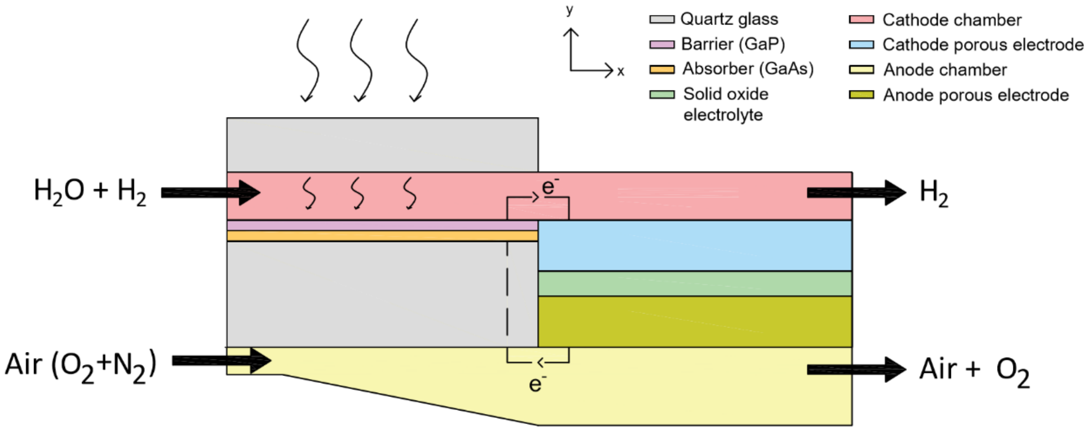

Figure 68- Proposed design configuration example 1.

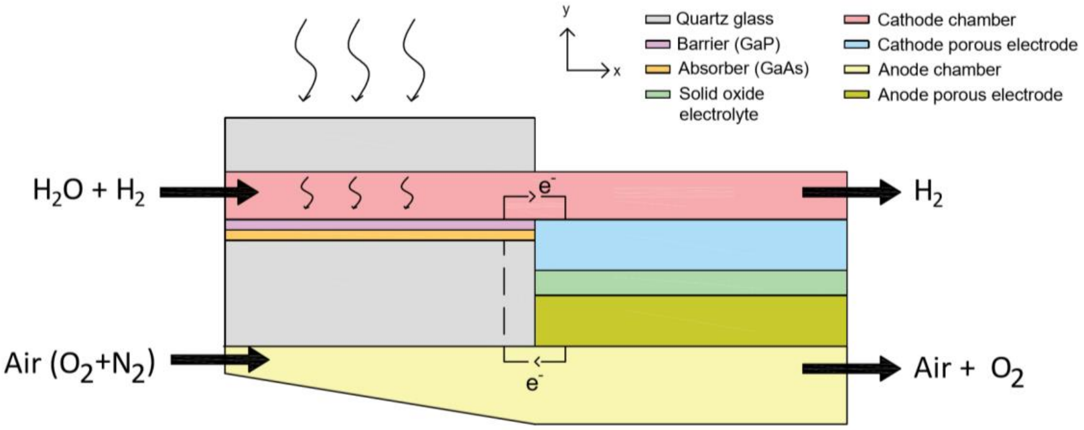

Figure 69- Proposed design configuration example 2.

8. CONCLUSION

The carried out study was able to successfully show an integrated HTSC-SOE device can operate to produce, efficiently, hydrogen and synthetic gas. Two different simulations were performed independently, one for the design of the device aimed at producing hydrogen gas, and another for the production of hydrogen and carbon monoxide (synthetic gas), mean to undergo the Fischer-Tropsch process to be converted in synthetic fuel. With this purpose, two parametric analysis were carried out, varying a number of parameters to asses their impact on the energetic and production performance of the device.

In the modelling of the device during the hydrogen production simulation, it was found out that the parameters which caused the most meaningful improvements in the performance of the device were those which led to an increased injected photocurrent. During the parametric analysis, the parameters which resulted in a positive effect in the STF efficiency, and thus on the energetic performance of the device were: reducing the number of solar cells, reducing the inlet cathode velocity and using an ideal electrolyte and cathode electrode. In opposition, those which resulted in a worsening of the efficiency of the device were: increasing the height of the cathode chamber and reducing the height of the anode chamber. Increasing the thickness of the cathode electrode had no effect on the energetic performance. The molar flow of hydrogen generated, and thus the production performance of the device was not affected in the same way by the variation of parameters. Using a lower number of photoabsorbers, decreasing he inlet velocity at the cathode chamber, reducing the height of the anode chamber and using an ideal electrolyte and cathode electrode led to an increase in the amount of H2 gas produced in the device. Increasing the height of the cathode chamber had a negative impact in the amount of gas produced, whilst, again, varying the cathode electrode thickness showed to have no impact.

Overall, the variation caused by the modification of the different parameters caused a practically negligible effect on both the energetic and production performance of the device, during the hydrogen production simulation. The maximum production improvement was attained when using three photoabsorbers (21mmolm^{-2}s^{-1}), 28.21% increase, whilst the next highest increase achieved was 3.05%, when varying the inlet velocity at the cathode chamber. When considering the effect in the energetic efficiency, it was again the variation of the photoabsorber number the parameter which caused the most meaningful improvement, achieving a 28.25% increase with respect to the reference case (efficiency of 9.97%), followed by the 3.06% increase caused by the reduction of the cathode chamber's inlet velocity. Design and operating conditions such as the variation of the chamber's heights, thickness or the use of ideal electrolytes and electrodes have a minor, not to say negligible effect in the performance of the device, approximately 1.13% increase with respect to the minimum amount of H_2 produced in the reference case and 0.77% increase with respect to the minimum STF efficiency obtained in the reference case. For this reason, we took one step further in the design of the device, combining those parameters which allowed for the use of an even lower number of operating photoabsorbers, in order to further improve the performance of the device. With this design, a 68.05% increase in the current density was achieved, resulting in an 82.43% increase in the STF efficiency, and an 82.36% increase in the hydrogen production, with respect to the reference case. In other words, a STF efficiency of 14.18% and a molar H2 flow rate of 29.87 mmolm^{-2}s^{-1} were attained.

In the case of the syngas generation simulations, it was concluded that the most transcending variable to control was the H_2/CO ratio. The desired value of 2 could be obtained via two different methods, either controlling the amount of species available for the reaction or increasing the operating temperature of the electrolyser. The first approach involved reducing the source for H_2 formation by reducing the amount of water supplied, and was proved to be effective influencing the amount of H_2 and CO produced. However, we were not able to prove in this study how the desired ratio of 2 could be obtained by increasing the temperature of the electrolyser. We predict that the correct ratio of 2 could be achieved if an inlet molar fraction of water of 0.095 is used in the operation of the device.

Regarding the usage of an integrated device in comparison with a quasi-integrated model, we concluded the integrated approach proved a higher potential than its predecessor. Even though the results of the original device presented better values during the reference case (in the H_2 production simulation), when parameter modifications were imposed, more positive effects were seen in the integrated device than in the quasi-integrated proposal. Nonetheless, it would be interesting to carry out additional research, studying a wider variety of possible improvement sources, such as the possibilities proposed in this study, in order to better provide the optimum design guidelines for an integrated high-temperature photoelectro-chemical device.

The development of this research was carried out aiming that our results could be used as guidelines for further investigation in the field, with the ultimate goal of generating clean fuels, proceeding from renewable energies.

9. BIBLIOGRAPHY

[1] James Ellsmoor, “Renewable Energy Is Now the Cheapest Option- Even Without Subsidies”, *Forbes*, Jun.15, 2019. https://www.forbes.com/sites/jamesellsmoor/2019/06/15/renewable-energy-is-now-the-cheapest-option-even-without-subsidies/#2713492f5a6b.

[2] “Renewble Power Generation Costs in 2018”, *International Renewable Energy Agency*, May 2019. https://www.irena.org/publications/2019/May/Renewable-power-generation-costs-in-2018.

[3] “Why Clean Energy?”, *NC Sustainable Energy Association*. https://energync.org/why-clean-energy/.

[4] “Hydrogen helping the environment, reducing carbon emissions”, *Open Access Government*, August 4, 2019. https://www.openaccessgovernment.org/hydrogen-reducing-carbon-emissions/65739/.

[5] “Hydrogen Applications”, *Hydrogen Europe*. https://hydrogeneurope.eu/hydrogen-applications.

[6] “Hydrogen Production”, *Hydrogen Europe*. https://hydrogeneurope.eu/hydrogen-production-0.

[7] Seval Gunduz, Dhruba J. Deka, Umit S. Ozkanm, “Advances in Hight-Temperature Electrocatalytic Reduction of CO_2 and H_2O”, *Advances in Catalysts*, vol. 62, pp. 113-165, 2018.

[8] Rachael Elder, Denis Cumming, Mogens Bjerg Mogensen, “High temperature electrolysis”, *Carbon Dioxide Utilisation*, pp. 183-209, 2015.

[9] S. Licht, *J. Phys. Chem. B*, 2003.

[10] S. Licht, “STEP (Solar Thermal Electrochemical Photo) Generation of Energetic Molecules: A Solar Chemical Process to End Anthropogenic Global Warming”, *J. Phys. Chem*, 2009.

[11] J.W. Schwede, T. Sarmiento, V.K. Narasimah, S.J. Rosenthal, D.C. Riley, F. Schmitt, I. Bargatin, K. Sahasrabuddhe, R.T. Howe, J.S. Harris, N.A. Melosh, Z.X. Shen, “Photon-enhanced thermionic emission from heterostructures with low interface recombination”, *Article Nature Communications*.

[12] Yang Yang, Wenzheng Yang, Weidong Tang and Chuandong Sun, “High-temperature solar cell for concentrated solar-power hybrid systems”, *Applied Physics Letters 103*, 2013.

[13] Ronald R. Gutierrez and Sophia Haussener, “Modelling and design guidelines of high temperature photoelectro-chemical devices”, *The Royal Society of Chemistry*, pp. 1-14, 2010.

[14] “Temperature dependence of the energy bandgap”. https://ecee.colorado.edu/~bart/book/eband5.htm.

[15] PV Education. https://www.pveducation.org.

[16] A.Dhouib, S. Filali, “Operating Temperatures of Photovoltaic Pannels”, *Energy and the environment*, pp. 494-498, 1990. https://www.sciencedirect.com/science/article/pii/B9780080375397500855.

[17] B.J. Skromme, “Junctions and Barriers”, *Encyclopedia of Materials: Science and Technology (Second Edition)*, pp. 1-12, 2003.

[18] Yang Yang, Wenzheng Yang, and Chuandong Sun, “Heterostructured cathode with graded bandgap window-layer for photon-enhanced thermionic emission solar energy converters”, *Solar Energy Materials & Solar Cells 132,* 132 pp. 410-417, 2015.

[19] Odne Stokke Burheim, “Hydroogen for Energy Storage”, Engineering Energy Storage, chp. 8, pp. 147-192, 2017.

[20] “Faraday’s Law”. https://en.wikipedia.org/wiki/Faraday%27s_laws_of_electrolysis.

[21] Di Xu, Lichun Dong, Jingzheng Ren, “Introduction to hydrogen routines”, Hydrogen Economy, chp. 2, pp- 35-54, 2017.

[22] Lecture “Biomass conversion: bioliquids”, course: Renewable Energy (for ME), EPFL, Spring semester, 2019-2020.

[23] Romain Couderc, Mohamed Amara, and Mustapha Lemiti, “In-depth analysis of heat generation in silicon solar cells”, *IEEE Journal of photovoltaics,* vol. 6, no. 5, September 2016.

[24] Meng Ni, “An electrochemical model for syngas production by co-electrolysis of H_2O and CO_2”, *Journal of Power Sources 202*, pp. 209-216, 2012.

[25] Meng Ni, Michael K.H. Leung, Dennis Y.C. Leung, “Parametric study of solid oxide steam electrolyzer for hydrogen production”, *International Journal of Hydrogen Energy 32,* pp. 2305-2313, 2007.

[26] M.A. Laguna-Bercero, “Recent advances in high temperature electrolysis using solid oxide fuel cells: A review*”, Journal of Power Sources 203*, pp. 4-16, 2012.

[27] Van Nhu Nguyen and Ludger Blum, “Syngas and Synfuels from H_2O and CO_2: Current Status”, *Chemie Ingenieur Technik*.

[28] Jan Pawel Stempien, Qiang Sun, Siew Hwa Chan, “Solid Oxide Electrolyser Cell Modelling: A Review”, *Journal of Power Technologies 93 (4),* pp. 216-246, 2013.

[29] Allen J. Bard and Larry R. Faulkner, “Electrochemical methods, fundamentals and applications”.

[30] R. Bader, W. Lipinski, “Solar Thermal Processing”, *Advances in Concentrating Solar Thermal Research Technology,* pp. 403-459, 2017.